The Development of an Automated System for Electrical Characterization of Cells Using a Novel Force Balance Method

by

Hao-Wei Su

B.S., Electrical Engineering, National Taiwan University 2009

SUBMITTED TO THE DEPARTMENT OF ELECTRICAL ENGINEERING AND COMPUTER SCIENCE IN PARTIAL FULFILLMENT OF THE REQUIREMENTS FOR THE DEGREE OF

MASTER OF SCIENCE

AT THE

MASSACHUSETTS INSTITUTE OF TECHNOLOGY

SEPTEMBER 2012

Signature of Author_____

Hao-Wei Su
Department of Electrical Engineering and Computer Science
August 7, 2012

Certified by_____

Joel Voldman
Associate Professor of Electrical Engineering and Computer Science
Thesis Supervisor

Accepted by_____

Leslie A. Kolodziejski
Professor of Electrical Engineering and Computer Sciences
Chairman, Department Committee on Graduate Committee

The Development of an Automated System for Electrical Characterization of Cells Using a Novel Force Balance Method

by

Hao-Wei Su

Submitted to the Department of Electrical Engineering and Computer Science

on August 7, 2012

in Partial Fulfillment of the Requirements for the Degree of Master of Science

ABSTRACT

Dielectrophoresis (DEP), a cell separation technique based on the dielectric properties, has significantly advanced biomedical research in diverse applications ranging from blood stem cells purification to cancer cells isolation from heterogeneous populations. The ability to accurately measure the dielectric properties of individual cells is not only critical for effective sorting applications, but is also advantageous for enhancing the current knowledge of cell biology.

This thesis proposes a novel method: *the n-DEP spring*, which applies an electrical field gradient upon continuously flowing cells to distinguish them based on their individual DEP properties. Specifically, the method uses the equilibrium position originating from the force balance between hydrodynamic and DEP forces to infer the cellular dielectric properties.

For thorough DEP characterization, changing different conditions of cells is an essential but time-consuming process which usually takes hours to days. Especially for DEP characterization of time-sensitive events, such as neutrophil activation or cell apoptosis, short characterization time is required. This thesis describes the automation of the fluidic, optics, and electronics components of the DEP characterization system, which shortens the characterization time within an hour.

We first demonstrated the automated DEP characterization of a mammalian cell type in thirty-nine conditions within an hour. Subsequently, we characterized the neutrophils with different activation states and successfully found out the right conditions to discriminate the activated neutrophils and non-activated neutrophils. With this system and method, we now have the potential to rapidly screen through a variety of system parameters, and optimize conditions for effective cell sorting.

Thesis Supervisor: Joel Voldman

Title: Associate Professor of Electrical Engineering and Computer Science

ACKNOWLEDGEMENTS

First of all, I would like to express my deepest gratitude to Prof. Joel Voldman for guiding me, encouraging me, and helping me with his knowledge and patience during the entire duration of my Master of Science. Under his weekly advices, I have become more mature in critical thinking, scientific writing, and conducting independent research. I would also like to thank collaborators in MIT Lincoln Laboratory, especially Lalitha Parameswaran and Richard Mathews, for valuable discussions and lending me the high frequency equipment.

Secondly, I want to thank all my previous and current lab mates in Voldman's group, especially Michael Vahey, the man I admire for his great knowledge of dimensional analysis and differential equations where this work built on, as well as his professional attitude and work ethics. Also thanks to Marc, Javier, Thibault, and Tao for sharing their experience of the DEP characterization and sorting and providing guidance and useful suggestions for my thesis. Thanks to Sarvesh for sharing the little stories of the first two years of our MIT graduate life, Burak for thoughtful academic discussion and Aalap for enlightening the group meeting as well as organizing an awesome group outing event. Thanks to Laralynne and Catherine for answering my biology and many other questions, Lily for holding the FluidicMEMS where I felt connected to the microfluidic people. Thanks to Salil for his late night discussion, his plastic masters and his humorous words. Thanks to Minoru who introduced me to delicious Japanese food and played tennis with me. Thanks to Chad for taking care of our lab works and purchases. Also thanks to Katarina, Pat, Wei-Mong, Melanie, Anna, Moritz, and the UROPs Ram, Tiffany, and Yu-Chi who shared my enjoyable life in Voldman's lab.

Thirdly, this work would not been finish without many people who have helped me outside the lab. I want to thank Prof. Dennis Freeman and Prof. Rohit Karnik for thorough discussions. I want to thank Chia-Hua Lee for providing the HL-60 cells and Lara for providing the blood cell separation protocol. I also want to thank the staff and members of MIT MTL for training me the fabrication process.

Finally, I owe special thanks to all my friends for accompanying me through the ups and downs in this two years. At last, most importantly, thanks to my family for everything.

Table of Contents

List of Figures

Chapter 1: Introduction

In this chapter, we will introduce the background and motivation for measuring dielectrophoretic (DEP) forces, the existing methods for measuring DEP forces, and our approach. Finally, we will provide our specific aims and the overview of the thesis and in the last section.

1.1. Dielectrophoretic cell separation

Cell separation is an important technology for medical diagnostics, therapy and basic biological research. Label-free cell separation methods are a subgroup of cell separation methods that separate cells based on physical intrinsic properties such as size, shape, deformability, density and electrical properties [1]. Unlike commonly used cell sorting methods, such as fluorescent-activated cell sorting (FACS) and magnetic-activated cell sorting (MACS), label-free separation methods require no biochemical labels that would remain on the cells after the sorting. These methods include using mechanical filters [2], hydrodynamic force [3], deterministic lateral displacement [4], inertial forces [5], gravity [6], intrinsic magnetic properties [7], acoustophoresis [8], and dielectrophoresis [9]. Among these techniques, dielectrophoresis is the only method that separates cells based upon their intrinsic dielectric properties and therefore dielectrophoresis can perform separations that no other label-free methods can achieve.

Dielectrophoresis (DEP) has been actively applied to biosensors, cell therapeutics, drug discovery, medical diagnostics, microfluidic, and particle filtration during the past 10 years [10]. In the application of cell-based assays, it has been used to resolve different cellular identities in heterogeneous populations and to monitor cell state without bio-markers. Some common demonstrations include separation of different leukocytes subpopulations [11], viable/non-viable yeast cells [9] [12], and modified/unmodified bacteria [13]. Other interesting medical applications include enrichment of CD34+ cells from peripheral blood stem cell harvests [14], separation of cancer cells from blood [15], and isolation of malaria-infected blood cells [16]. Recently, dielectrophoresis has also been applied to stem cell research, investigating the relationship between the electrical phenotype and the differentiation state of neural stem cells [17]. The miscellaneous applications indicate the potential impact of the DEP separation.

The DEP applications are based on the DEP force difference between target populations. Some of them use the difference of the DEP force directions (attractive/repulsive) to separate cells. Some of them use the magnitude of the DEP forces to separate the cells. For example, the separation of viable/nonviable yeast cells [12] used attractive/repulsive DEP force. Namely, the DEP force pushes away the nonviable cells to the weak electric field (which we call negative DEP, or n-DEP) and attracts (which we call positive DEP, or p-DEP) the viable cells to the strong electric field. On the other hand, the separation of leukocytes subpopulations [11] uses n-DEP magnitude separation. Namely, the cells flow through a series of diagonal parallel electrodes which generate the n-DEP forces for lateral deflection. The larger the n-DEP force is,

the larger the lateral displacement is. Both magnitude and direction DEP separation are important in different applications.

The DEP forces acting on the cells depend on a few things: the cell morphology (size and shape), the electrical properties of the cell, the electrical properties of the media, and the electric field. In particular, the frequency of the electric field and the media conductivity are the two factors that are easy to manipulate to affect the DEP separation. Finding the right frequency and the right media conductivity to separate target cells is important. Estimating the DEP forces in different frequencies and media conductivities can help us improve the DEP separation and understand the electrical properties of the cells. In this thesis, we are developing a new method and a new system for measuring the n-DEP forces on cells in different frequencies and conductivities.

1.2. Approaches for measuring the DEP force

Even though there are over 100 publications of the DEP cell separation device for the past 5 years [18], few of them tried to quantify the exact DEP forces acting on the cells because most DEP separation devices only need to optimize its particular application, which can be done without quantification of DEP forces, but rather by trial and error. However, quantifying the DEP forces of the cells can help us determine the electrical properties of cells and why they can be separated. There are some approaches have been developed for obtaining the DEP forces on the cells. We briefly review these methods below.

Hydrodynamic drag force balance: When the cell has relative velocity to the surrounding fluid flow, the hydrodynamic drag force acting on the cell, known as Stokes' drag force, is well-understood in most microfluidic system. Therefore, several methods use the calculated hydrodynamic force as a known force to measure the DEP force.

Thomas Schnelle *et al.* has studied the n-DEP against the hydrodynamic drag force with the top-down parallel electrodes geometry [19]. They used a quarter circle-shaped electrodes to deflect the cells so that the hydrodynamic drag forces counteracted with the n-DEP force barriers were continuously changing (different angles between the flow and n-DEP force) in different parts of the electrodes. They estimated the n-DEP force by matching the corresponding hydrodynamic force where the particles passed through the quarter circle-shaped electrode. The advantage of the continuous flow system is measuring the n-DEP force for a lot of cells without stopping. However, the disadvantage is that the cells only pass through the electrodes once so that one cell can only be characterized under one condition. It is difficult to measure single cell in different frequencies or media conductivities.

Instead of having the flowing fluid, there are approaches of measuring the cell velocities in a static flow DEP system. Thibault Honegger *et al.* placed the particles on coplanar electrodes and applied a continuous frequency sequence to switch the DEP force between p-DEP and n-DEP

[20], and derived the DEP frequency spectrum for single particles. This method is highlighted for a wide frequency spectrum of the DEP force for single particles. However, the system does not work in highly conductive media because the cells only experience n-DEP in such high conductive media so the cells cannot concentrate on to the electrodes by p-DEP.

Gravitational force balance: There are approaches that use the gravitational/buoyant force as the known force to measure the DEP force. In 1977, H. A. Pohl and R. Pethig measured the balance height between the gravity and the DEP force [21]. They put the particles on a pair of electrodes that generated an isomotive electric field and pushed the cells upward against the gravity. Recently, a Japanese group modified this method by putting the experiment in an inclined floor [22] to control the magnitude of the gravitational force. This method can measure very minute DEP forces at small inclined angle (25 fN) and obtain the frequency spectrum of the DEP force of single particles (both p-DEP and n-DEP). However, the gravitational/buoyant force of the cell is usually below pN and therefore the maximum DEP force this method can achieve cannot exceed pN and therefore limits the dynamic range of this measurement. Furthermore, the density of the particle is needed for calculating the corresponding DEP force.

Optical tweezers: There are approaches that use optical tweezers to measure the DEP force. Optical tweezers are a technique that confines the cell in a small region using a focused laser beam to centralize the cell in the middle of the laser beam. The cell experiences a position-dependent optical force that moves the cell to the central of the laser beam due to the refractive index difference between the cell and the media. A German group has combined this technique with the dielectrophoretic cage [23]. They used the DEP force to calibrate the optical tweezers. Recently, a group at Lehigh University also used optical tweezers combined with amplitude-modulated DEP force to measure the DEP force [24]. However, the optical force depends on the laser power, the refractive index of the particle/media and thus requires calibration beforehand.

Automated high-throughput approaches: Instead of measuring single particles, there are also approaches for measuring DEP forces on a population of cells in an automated and high-throughput way. Michael Hughes' group has developed a method for measuring the DEP response at different frequencies for a large population of cells using the light absorption intensity in DEP-activated microwells [25]. Another common method is to quantify the amount of cells that trapped by the p-DEP and correlate it to the magnitude of the p-DEP force [26]. However, in these approaches, single cell information has lost because they do not measure the behavior of individual cells.

Non-DEP approaches: The DEP force can be calculated from the dielectric properties of the cells. Therefore, instead of DEP force, there are methods that measure the dielectric properties of the cells and then predict the DEP phenomena from the dielectric properties of cells. The common methods are electro-rotation [27] and dielectric spectroscopy [28]. These methods are

linked to the DEP force based on the dielectric model of the cell which we will describe in section 2.4.

Comparison among methods

Methods using the gravitational force or optical force require additional knowledge of the other cell properties such as density and refractive index of the cell, which are non-trivial to measure. Single-cell DEP measurement methods are usually time-consuming so that the number of cells measured is usually <100. The automated high-throughput approaches can measure many cells but usually lack single-cell DEP information. The impedance spectroscopy method and the electro-rotation are linked to the DEP force through dielectric models, which can be oversimplified for cells. They also require the single cell size information with the impedance/rotation rate to deduce the single cell DEP force. Therefore, a high-throughput method for measuring the DEP force on individual cells is needed. In this thesis we develop a continuous DEP force measurement method for high-throughput single-cell characterization using hydrodynamic and DEP force balance. The method is similar to Thomas Schnelle's approaches [19] but has several advantages which we will describe in the following section.

1.3. Introduction to the n-DEP spring

The n-DEP spring is a high-throughput method of measuring n-DEP force on individual cells using the force balance between the n-DEP force and the hydrodynamic force (**Figure 1-1**). This method is similar to Thomas Schnelle's approach [19], but instead of measuring the maximum holding force of the n-DEP barrier, we measure the n-DEP forces in different balance positions, δ, which counteracts with the hydrodynamic force. It has the advantage as a continuous characterization method while shrinking the needed field of view for detection within 50 μm square, and thus provides capability of high-resolution imaging. A similar method for measuring the DEP force through hydrodynamic force has described in the calibration of optical tweezers [23]. However, they did not implement their method in flow. The n-DEP spring method allows us to characterize the same cell many times as it flowing through. For the device geometry, instead of using a pair of top-down parallel electrodes, we use a simple fabricated parallel coplanar electrodes structure.

Essentially, the electrodes generate an n-DEP force gradient where the largest force occurs at the inner edges of the electrodes. In actuality, the DEP force is a 3D vector field but we can simplify the problem into 1-dimension through appropriate choice of electrode design [**Figure 1-1(a)**]. Even though 3D trajectory and motion analysis for extracting the DEP force is possible [29], simplification can reduce the number of parameters we need to measure.

We only analyze the force balance in a direction perpendicular with the central line of the coplanar electrodes but also in parallel with the substrate where the coplanar electrodes are on.

This makes the n-DEP barrier similar to a 1-D nonlinear spring: the more you push the cell with the hydrodynamic force, the more the spring is compressed. By putting a smaller angle between the flow direction and central line of the coplanar electrodes, we can continuously measure the balance positions from the images for a large amount of cells in a higher throughput manner [**Figure 1-1(b)**]. We can experimentally obtain the 1-D n-DEP force as a function of the balance position by giving different flow rates of the hydrodynamic force. The n-DEP force is proportional to the square of the applied voltage. Therefore, the stiffness of this n-DEP spring is also proportional to the square of the applied voltage. With the same hydrodynamic drag force, the larger the voltage is, the stiffer the n-DEP spring is, and the larger the balance position is. To give a qualitative idea of this method, we show the red blood cell images with different applied voltages [**Figure 1-1(c)**]. We can observe the balance positions increases when the voltage rises.

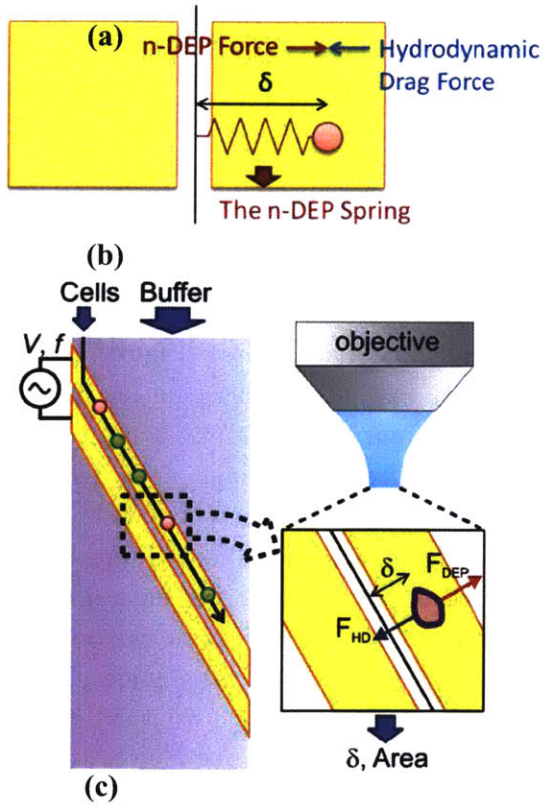

Figure 1-1 The general idea of the n-DEP spring. (a) The schematic of the 1-D n-DEP spring. The n-DEP force from the coplanar electrode (yellow) is like a nonlinear compressive spring because it has a position dependent reacting force. The more the applied hydrodynamic drag force is, the smaller balance position, δ, is. The stiffness of this n-DEP spring depends on several parameters: the voltage of the electric field, the cell size and the polarizability of the cell/media. **(b) Applying the n-DEP spring in a continuous manner.** The angled coplanar electrodes enable us to measure the balance position and the cell size in a continuous way. **(c) The n-DEP spring for different voltages on the red blood cells.** The balance positions of three different applied voltages are compared in the image. The balance position increases with the voltage.

The benefits of the n-DEP spring method are the continuous measurement for the cells and its capability to measure the force in highly conductive media. The other aspect worth highlighting is, compared to Thomas Schnelle's approach [19] , the measurement only requires a small field of view so that we can minimize the field of view and thus use higher magnification to obtain high-resolution images of the cells.

The general constraint about this method is that this method can only measure the cells that are deflecting by the electrodes but not able to measure the cells that experience p-DEP forces or very small n-DEP forces that are overwhelmed by the hydrodynamic drag force. Another constraint is that if one wants to get the exact value of the DEP force, the size of the cell needs to be measured accurately to calculate the hydrodynamic drag force (explained below in section Chapter 3: 3.3).

In this thesis, we will combine this n-DEP spring method with an automated system for quantifying the n-DEP force acting on the cells in different frequencies and different media conductivities. The measured result can assist the process of finding the right frequency and media conductivity for n-DEP magnitude separation of the cells. Furthermore, with the morphology information (size, shape), the electrical properties can be extracted out from the n-DEP forces. Therefore, the size, shape, and the electrical properties of the cells can be measured simultaneously for the same cell. The multi-modal electrical and optical parameters can be used for optimizing new label-free separation applications that use size, shape, and/or electrical properties.

1.4. Thesis overview

We have the following objectives in this thesis:

(1) The development of the n-DEP spring model for n-DEP force measurement: Derive the analytical expression for the n-DEP force and hydrodynamic force. Calculate the analytical expression of the balance position. Experimentally verify the expression with standard particles.

(2) The development of an automated system for generating various conditions for n-DEP force characterization: Develop a computer controlled dynamic conductivity generator to perform spatially and temporally changes media conductivity. Develop a computer controlled integrated system for automatic measurement of balance positions in different voltages, frequencies, flow rates and media conductivities.

(3) The n-DEP force measurement of the human promyelocytic leukemia cells (HL-60): Perform a full electrical characterization of HL-60 cells in different frequencies and media conductivities.

(4) The demonstration of a real medical application--characterization of activated and unactivated neutrophils: Measure the balance positions of activated neutrophils and

nonactivated neutrophils in different frequencies and media conductivities and find out the DEP separation condition.

Scope of the thesis

In order to understand the mathematic basis of this method, we will first introduce the underlying theory of DEP and the dielectric model of cells in chapter 2. Then we will introduce the analytical model for n-DEP spring in chapter 3. In chapter 4, we will describe the development of the automated system for providing dynamic control of media conductivity/conductivity gradient and different electric field frequencies.

Chapter 5 gathers the main experiment to demonstrate the data for objectives (1)-(4). To validate the n-DEP spring method, in section 5.1, we will show the 6 μm polystyrene beads as the standard particles to experimentally validate the balance position model. In section 5.2, we will demonstrate the first automated high-throughput n-DEP force measurement of HL-60 cells at various frequencies and media conductivities. To show the power of fast characterization of the cells, we will show the n-DEP spring applied in a real medical application: finding the DEP separation conditions in activated neutrophils and non-activated neutrophils in a short amount of time. The system we have developed is not limited to study the electrical properties of cells but also optical properties of the cells. In the chapter 6, we will conclude our contributions and provide some interesting preliminary result of the future direction using the electrical and optical properties simultaneously.

Chapter 2: DEP theory and the dielectric properties of the cells

We introduced DEP separation and its application in section 1.1 in a qualitative fashion. In this chapter, we will introduce the mathematical formulations of the DEP force and the dielectric properties of the cells. In section 2.4, we will introduce the existing method of measuring the dielectric properties of cells and compare the pros and cons of the DEP characterization with other methods. In the end, we will describe how our method fits into the niche of DEP characterization.

2.1. DEP force and the Clausius-Mossitti (CM) factor

Inside a static electric field (**E**), the particle and the surrounding media are both polarized to form a dipole moment. The effective induced dipole moment (**p**) is either parallel or anti-parallel to the applied field (**Figure 2-1** (Pohl and Crane 1971). If the electric field is uniform, there is no net force acting on the particle. However, in a spatially non-uniform electric field, the dielectrophoretic (DEP) force will either move the particle toward stronger electric field (positive DEP) or toward weaker electric field (negative DEP). The direction of the force depends upon the electrical properties of the particle and medium.

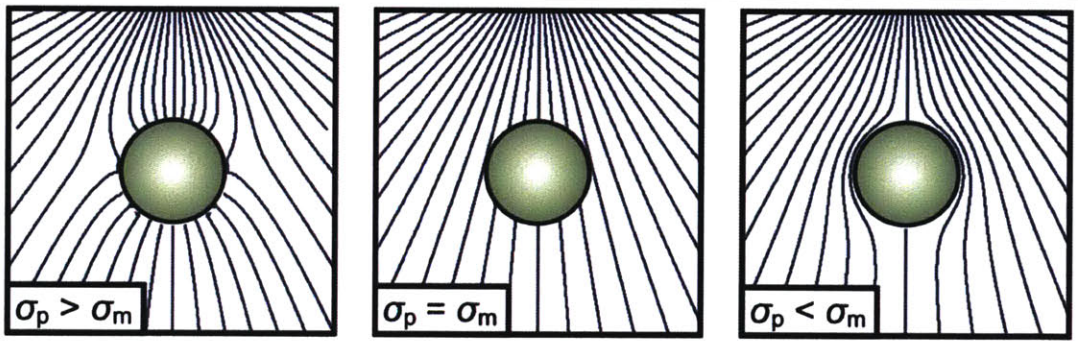

Figure 2-1 Polarization of a particle in an external non-uniform electric field. For relatively conductive particles (left), the dipole moment and electric field align parallel to each other, leading to lower potential energy at higher electric field strengths, known as p-DEP. For relatively insulating particles (right), the dipole moment and external field are anti-parallel, causing particles to be expelled from regions of higher field intensity, known as n-DEP. If the electrical properties of the particle match those of the medium (center), the polarization vanishes and there is no preferential motion towards higher or lower field strengths. Adapted from Mike Vahey [51].

In an AC electric field, the first order time-average DEP force is approximated as:

$$\overrightarrow{F_{DEP}} = (\vec{p} \cdot \nabla)\vec{E} = 2\pi R^3 \varepsilon_m \,\mathrm{Re}[\underline{CM}(w)]\nabla E^2 \qquad (2\text{-}1)$$

where R is the particle radius, ε_m is the permittivity of the media, E is the amplitude of the electric field, w is the frequency, and $CM(w)$ is the Clausius-Mossitti(CM) factor which is given by

$$\underline{CM}(w) = \frac{\underline{\varepsilon}_p - \underline{\varepsilon}_m}{\underline{\varepsilon}_p + 2\underline{\varepsilon}_m} \qquad (2\text{-}2)$$

where $\underline{\varepsilon}_p$ and $\underline{\varepsilon}_m$ are the complex permittivity of the particle and media, respectively. The sign of the $\mathrm{Re}[\underline{CM}(w)]$ determines the force direction. Due to the mathematical formulation of CM factor, the real part of the CM factor is always between -0.5 and 1.

The media can be considered as a loss-free capacitor in parallel with a resistor. Therefore, the complex permittivity of the media $\underline{\varepsilon}_m$ is a combination of permittivity and conductivity of the media solution.

$$\underline{\varepsilon}_m = \varepsilon_m + \frac{\sigma_m}{jw} \qquad (2\text{-}3)$$

For example, in phosphate buffered saline (PBS), the media permittivity ε_m is $78.5\,\varepsilon_0$ and the media conductivity σ_m is 1.6 S/m. For a typical DI (de-ionized) water, the media conductivity σ_m is around 0.01 mS/m. For an ideal pure water at room temperature, the media conductivity σ_m is 5.5 μS/m .

The complex permittivity of the particle is determined by the materials comprising the particle. If the particle is composed of a uniform material, the particle can be modeled similarly to the media.

$$\underline{\varepsilon}_p = \varepsilon_p + \frac{\sigma_p}{jw} \qquad (2\text{-}4)$$

For example, the polystyrene (PS) latex beads, the permittivity ε_p is $2\sim3\,\varepsilon_0$ and the conductivity σ_p is composed of two parts, the surface conductivity σ_s and the bulk conductivity σ_b. In theory, the bulk conductivity of the micro-submicron latex beads is negligible compared to the surface conductivity σ_s, which is inversely proportional to the particle radius R and proportional to the general surface conductance K_s (~1 nS for PS beads).

$$\sigma_p = \sigma_b + \sigma_s = \sigma_b + \frac{K_s}{R} \tag{2-5}$$

In low frequency range, the CM factor mainly depends on the conductivity of the particle and media.

$$\underline{CM}(w) = \frac{(\varepsilon_p + \frac{\sigma_p}{jw}) - (\varepsilon_m + \frac{\sigma_m}{jw})}{(\varepsilon_p + \frac{\sigma_p}{jw}) + 2(\varepsilon_m + \frac{\sigma_m}{jw})} = \frac{(jw\varepsilon_p + \sigma_p) - (jw\varepsilon_m + \sigma_m)}{(jw\varepsilon_p + \sigma_p) + 2(jw\varepsilon_m + \sigma_m)} \approx \frac{\sigma_p - \sigma_m}{\sigma_p + 2\sigma_m} \tag{2-6}$$

As a result, for micron size PS beads, the CM factor is positive in low-conductivity media (DI water) and negative in high-conductivity media (ionic solution).

2.2. Dielectric models of the cells

Unlike uniform latex beads, cells have more complex composition and different behavior than beads. Dielectrically, the cells are composed of several layers of materials. For example, a typical mammalian cell consists of cell membrane, the cell cytoplasm, the nuclear membrane, and the nuleoplasm from the outside to the inside of the cell. Each layer of the cell has distinct dielectric properties.

In order to match the true composition of the cell, the shell model has been developed to simulate the dielectric properties of the cell [30]. The single shell model [**Figure 2-2(a)**] and double shell model [**Figure 2-2(b)**] consider the cellto be composed of two and four concentric spherical shell layers of uniform conductivity and permittivity, respectively.

For the single shell model [**Figure 2-2(a)**], there are six parameters, including R, d, ε_{mem} , σ_{mem} ε_i, σ_i. The effective complex permittivity of the cell $\underline{\varepsilon_p}$ is given by

$$\underline{\varepsilon_p} = \underline{\varepsilon_{mem}} \frac{(\frac{R}{R-d})^3 + 2(\frac{\underline{\varepsilon_i} - \underline{\varepsilon_{mem}}}{\underline{\varepsilon_i} + 2\underline{\varepsilon_{mem}}})}{(\frac{R}{R-d})^3 - (\frac{\underline{\varepsilon_i} - \underline{\varepsilon_{mem}}}{\underline{\varepsilon_i} + 2\underline{\varepsilon_{mem}}})} \tag{2-7}$$

Similarly, the mathematical formulation of equation (2-7) can be recursively done with multiple layers of different material.

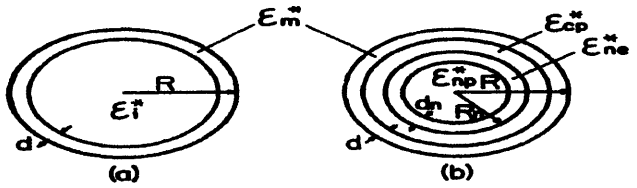

Fig. 1. Two electrical models of a cell. (a) Single-shell model. (b) Double-shell model. The phase parameters are represented by complex permittivity defined by $\varepsilon^* = \varepsilon - j\kappa/\omega\varepsilon_v$: ε, relative permittivity; κ, conductivity. $\omega = 2\pi f$: f, frequency; ε_v, permittivity of vacuum; j, imaginary unity. The subscripts refer to the following phases: m, plasma membrane; i, inner phase of cell; cp, cytoplasm; ne, nuclear envelope; np, nucleoplasm. The morphological parameters are: R, outer radius of cell; R_n, outer radius of nucleus; d, thickness of plasma membrane; d_n, thickness of nuclear envelope.

Figure 2-2 Two electrical models of a cell. (a) Single –Shell model. (b) Double-shell model. The cell is composed of concentric uniform layers of different complex permittivity($\underline{\varepsilon} = \varepsilon + \sigma/jw$). The subscripts refer to the following phases: m, plasma membrane; i, inner phase of cell; cp, cytoplasm; ne, nuclear envelope; np, nucleoplasm. The morphological parameters are: R, outer radius of cell; R_n outer radius of nucleus; d, thickness of plasma membrane; d_n thickness of nuclear envelope. Figure adopted from [32].

For a cell with a thin membrane, there is another representation of $\underline{\varepsilon_p}$, which is given by [31]

$$\underline{\varepsilon_p} = \frac{\underline{C_{mem}} R \underline{\varepsilon_i}}{\underline{C_{mem}} R + \underline{\varepsilon_i}} \tag{2-8}$$

where the membrane complex capacitance $\underline{C_{mem}} = C_{mem} + G_{mem}/jw$. C_{mem} and G_{mem} are the membrane capacitance and conductance which is derived from ε_{mem}/d and σ_{mem}/d.

Asami *et al.* measured the dielectric properties of mouse lymphocytes and erythrocytes in suspension using dielectric spectroscopy [32]. They fitted the measured complex permittivity $\underline{\varepsilon_p}$ of erythrocytes and lymphocytes with the simulation of single-shell and double-shell model. They extracted out the parameters of the shell model which have been referenced from various publications since then.

2.3. Re[CM] map and the Iso-dielectric point

From the single shell and double shell model, one can deduce the frequency dependency of the DEP behavior by their mathematical formulations. At lower frequencies, the DEP force mainly depends on the membrane properties. In higher frequencies, the force mainly depends on the cytoplasm conductivity (and/or the nuclear and cytoplasm ratio for double layer model). The DEP force is not only a function of frequency but also a function of electrical properties of the media. The common approach to disturb the DEP response of the cell is to change the media conductivity and the frequency. Therefore, we often use the 2-D (media conductivity and frequency) Re[*CM*] maps to explain the dielectric response or DEP separation of cells. The 2-D Re[CM] map as a function of frequency and media conductivity in **Figure 2-3** can help us

estimate the magnitude and the sign of the DEP force. In general, for cells, the Re[CM] is usually negative at high conductivity media because the media is more polarizable than the cell.

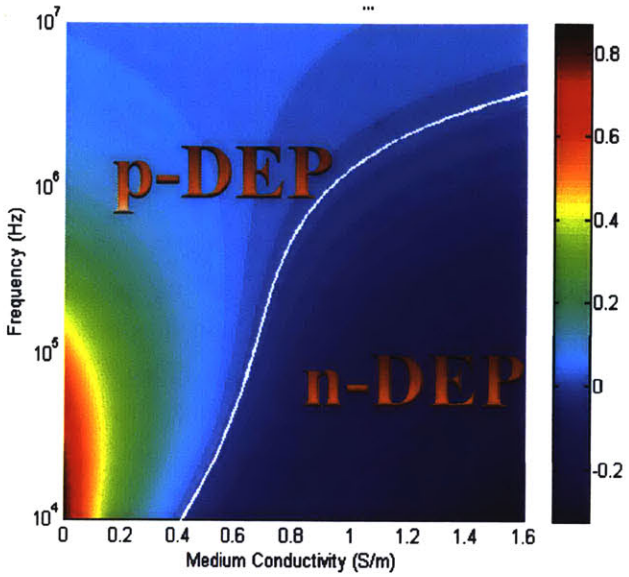

Figure 2-3 The real part of the Clausius-Mossitti factor as a function of the frequency of the external electric field and the media conductivity. The white-line shows the IDP (iso-dielectric point) curve where the particle experiences zero DEP force. The blue area on the right side is the condition where the cell experiences p-DEP force ($\mathrm{Re}[\underline{CM}]<0$) and the left side is the condition where the cell experiences p-DEP ($\mathrm{Re}[\underline{CM}]>0$). The white-line shows the condition where the cell experiences no DEP force ($\mathrm{Re}[\underline{CM}]=0$). We term any point this line as an iso-dielectric point, and the related frequency as the cross-over frequency. The electrical parameters for this figure come from dielectric spectroscopy for human white blood cells [11].

2.4. Methods of measuring the dielectric properties of cells

Over the past century, people have developed different methods to measure the dielectric properties of cells. The earliest work was comparing the conductivity of erythrocytes in high and low frequency in 1910s and they proved that cellular membranes exist electrically by the different response at low/high frequencies [33]. Following that, many techniques have been developed for dielectric measurement of cells, including dielectric spectroscopy [34], electro-rotation [35], and dielectrophoresis. We briefly introduce the three listed methods below.

Dielectric spectroscopy (bulk impedance measurement):

Dielectric spectroscopy is one of the earliest tools used in dielectric characterization of cells. Typically, the impedance of a cell population is measured using an impedance analyzer. The suspension is held in a reservoir containing two, three or four electrodes. An AC excitation signal is given to the suspension and the current passing through the system is measured as a

function of frequency. The relation between the complex permittivity $\underline{\varepsilon_{mix}}(w)$ of the whole mixture and the CM factor is given by

$$\underline{\varepsilon_{mix}}(w) = \underline{\varepsilon_m} \frac{1+2\varphi \underline{CM}(w)}{1-\varphi \underline{CM}(w)} \tag{2-9}$$

where the φ is the volume fraction of the cells and the media.

Electro-rotation (ROT):

Typically, electro-rotation is performed by putting a cell inside quadruple electrodes with four AC sinusoidal signals, successively 90° out of phase and thus creates a rotational electric field surrounding the cell. In the rotational electric field, if the induced dipole moment is not in phase with the electric field, a torque will act on the cell and make it rotate. The time-averaged torque is given by

$$\Gamma_{ROT} = -4\pi\varepsilon_m R^3 \,\mathrm{Im}[\underline{CM}]E^2 \tag{2-10}$$

and depends on the sign of the imaginary part of the CM factor ($\mathrm{Im}[\underline{CM}]$), the cell will rotate with or against the electric field. The electro-rotation is measured by analysis of the rotation rate, which is given by

$$R_{ROT} = -\varepsilon_m \frac{\mathrm{Im}[\underline{CM}]E^2}{2\eta} K \tag{2-11}$$

where η is the viscosity of the media and K is a scaling factor.

Dielectrophoresis (DEP):

The DEP force for a spherical particle inside non-uniform electric field was described in equation (2-1). Methods for measuring DEP force, including hydrodynamic drag force method, optical tweezers method, and gravitational method, were described in chapter 1.2. For the methods using velocity measurement, the step response of the velocity of the particle after initiation of a uniform DEP forceis given by

$$u = \frac{F_{DEP}}{6\pi R\eta} + (u_0 - \frac{F_{DEP}}{6\pi R\eta})e^{-t/(m/6\pi R\eta)} \tag{2-12}$$

where η is the viscosity of the media and u_0 is the initial velocity.

From equation (2-1), it is worth noticing that if one wants to calculate the $\mathrm{Re}[\underline{CM}]$, the size of the electrodes and the electric field gradient needs to be measured or calibrated. Alternatively, most DEP characterization methods chose to measure the DEP crossover frequency

($\mathrm{Re}[\underline{CM(w,\sigma_m)}]=0$) as a function of conductivity. The information, however, is not sufficient to determine the dielectric properties of cells in highly conductive media where the cell has no cross-over frequency. Also, the crossover frequency method is mathematically insufficient to obtain the entire $\underline{\varepsilon_p(w)}$ without electrical models of the cell. However, with the measurement of Re[CM] values in different conductivity, we can obtain the entire $\underline{\varepsilon_p(w)}$ without any electrical models. We will discuss the details in Appendix -B: Determining the electrical properties of the cell from Re[CM].

Discussion:

Dielectric spectroscopy (impedance method) can acquire the real part and imaginary part of the CM factor but it requires information of the volume fraction, which is not easy to get. The other caveat of dielectric spectroscopy is that the measurement of a mixture of cells is an average over a population rather than the electrical properties of a single cell. Recently, single impedance cytometry [36] has been developed to overcome this problem. This technique can measure single cell impedance in a flowing microfluidic device, but the measurement did not measure and decouple the morphological effect from the electrical properties. ROT can measure the rotation rates of a cell at different frequencies while obtaining optical information, and thus provide rich information for the imaginary part of the CM. It is famous for its sensitivity of dielectric characterization but also notorious for its low throughput and cumbersome cell loading process. On the other hand, DEP characterization is usually limited to cross-over frequency characterization because the DEP force is proportional to volume and it is hard to decouple the size and the $\mathrm{Re}[CM]$. There are approaches of size-insensitive characterization methods like DEP-FFF. However, there is no successful high-throughput method like single cell impedance spectroscopy for DEP characterization. The n-DEP spring method fits into the niche of high-throughput single cell measurement for DEP characterization where $\mathrm{Re}[CM]$ is negative.

Even though the experiments in this thesis only measure the DEP response of cells at a single frequency, the method can easily be extended to measure a frequency spectrum of $\mathrm{Re}[CM]$ of a single cell by applying a frequency sweep and tracking the cell position.

Thus, the n-DEP spring is a new way of extracting the dielectric properties of single cells that can potentially improve the DEP characterization and make them comparable to ROT and single cell impedance spectroscopy.

Chapter 3: n-DEP spring model

Now that we have introduced electrical forces and described different ways to extract out electrical properties of cells, in this chapter we will derive the analytical model for the n-DEP spring extraction method. The n-DEP spring method uses the force balance between the position-dependent DEP force and the constant hydrodynamic drag force to measure the DEP force from a particle's equilibrium position. We first discuss the hydrodynamic force drag force in the microfluidic channel and then evaluate the DEP force created by coplanar electrodes. By balancing the two forces, we determine the theoretical balance position as a function of flow rate, applied voltage, cell size, and the electrical properties of the cell. In section 3.6, we will describe relation between the balance position and binary n-DEP separation on the angle coplanar electrodes. At last, we describe the conditions where other forces become significant and their effect on balance positions.

3.1 Method overview

The n-DEP spring is a force balance method for measuring the negative DEP forces acting on individual cells in a continuous manner. The cell first enters the microfluidic channel from the inlet and flows with laminar flow until it runs into the electric field from the coplanar electrodes (**Figure 3-1**). The negative DEP force forms an invisible barrier to deflect the cell. The deflected cell reaches a force balance and moves along the electrodes with constant velocity. We use δ, the *balance position* between the hydrodynamic force and the DEP force in the direction perpendicular to the electrodes, to extract the electrical properties of the particles.

To use the n-DEP spring to extract electrical properties, we need to theoretically analyze the

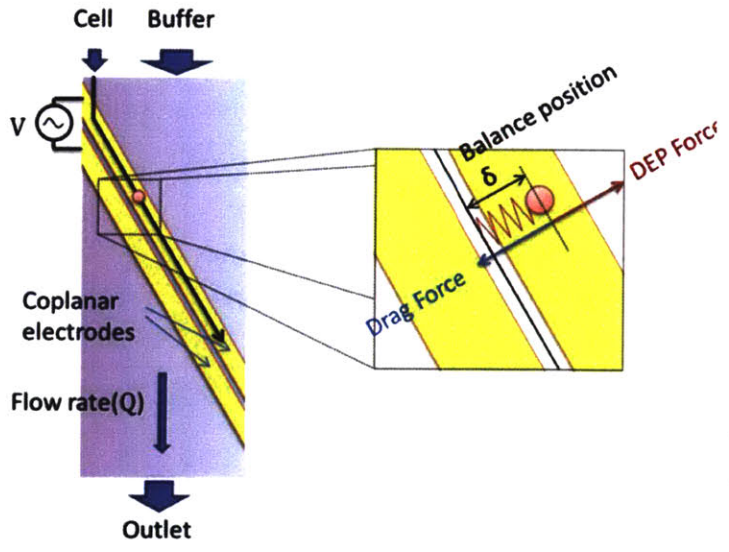

Figure 3-1 The n-DEP spring method overview. Cells (or other particles) are introduced into the channel along with buffer flow. As the cells flow down the channel they encounter the electrodes where they experience a DEP force (red, inset) that balances the drag force. The equilibrium balance position between the two forces is denoted by δ.

force balance for the deflected cell. We are going to find how the *balance position* relates to the electrical properties of the cell, the cell radius, the flow and the electric field.

3.2 The force balance of a particle moving along a pair of diagonal coplanar electrodes

The predominant forces acting on the deflected cell are the DEP force, hydrodynamic drag force, the contact force from the wall, the buoyant force and the lift force (**Figure 3-2**). In the *z*-direction, the DEP force is larger than the lift force and the buoyant force so that the cell is pushed by the DEP force to the ceiling of the channel. The reacting force from the ceiling offsets the excessive DEP force in the *z*-direction. Therefore, the buoyant force and the lift force do not affect the balance position unless they become comparative to the DEP force in z-direction. In the *y*-direction, the cell moves along the electrodes with constant velocity. The hydrodynamic drag force counteracts the friction force between the particle and the ceiling. In the *x*-direction, defined as perpendicular to the electrodes, we consider two predominant forces, the DEP force and the hydrodynamic force, in our first-order model. In the next two sections, we solve for the hydrodynamic drag force and the position-dependent DEP force to determine the *balance position*. There are some second-order forces, such as the friction force and the electro-hydrodynamic force that could affect the force balance and hence the *balance position.*

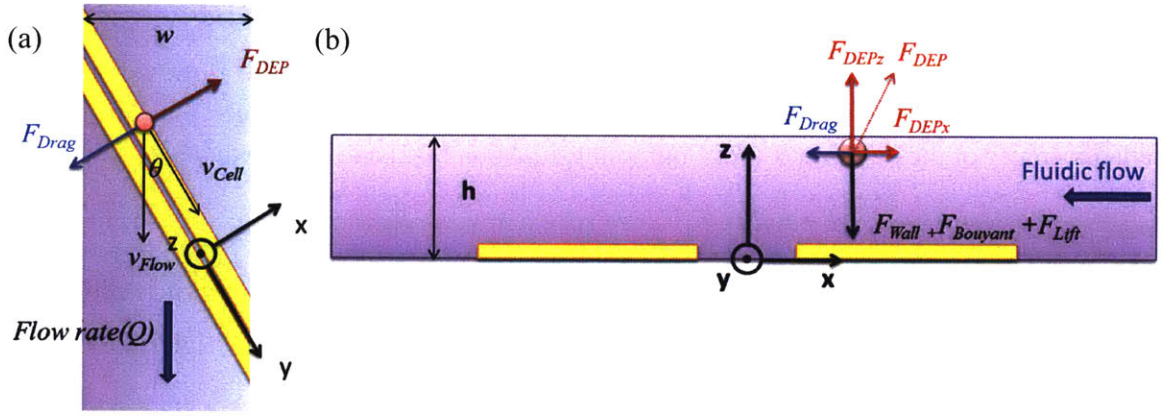

Figure 3-2 The force balance of the particle flow along the coplanar electrodes. (a) The top-down view of the microfluidic channel. (b) The cross-sectional view of the coplanar electrodes.

3.3 The hydrodynamic drag force in a microfluidic channel

The Reynolds number is a dimensionless number that represents the ratio between inertial forces and viscous forces in hydrodynamics. For Reynolds number much smaller than 1, the viscous force dominates and the Stokes' flow occurs. For water or physiological media flowing in a 20 μm by 2 mm rectangular channel with flow rate of 10 μL/min, the dimensionless Reynolds number is 0.167. Therefore, because our operating flow rates are at or below 10 μL/min, the flow

in our microfluidic channel can be treated as Stokes' flow. Mathematically, for a spherical cell moving in a uniform Stokes' flow, the hydrodynamic drag force (F_{Drag}) is given by

$$\overrightarrow{F_{Drag}} = 6\pi\eta R(\overrightarrow{v_{Flow}} - \overrightarrow{v_{Cell}}) \tag{3-1}$$

where η is the viscosity of the fluid. $\overrightarrow{v_{Flow}}$ is the average velocity of the flow which points to the outlet and $\overrightarrow{v_{Cell}}$ is the velocity of the cell which points along the electrodes. We can decompose the drag force into two components: F_{Dragx} (perpendicular to the electrodes) and F_{Dragy} (parallel to the electrodes). The two individual components are given by

$$F_{Dragx} = -6\pi\eta R \sin\theta \, |\overrightarrow{v_{Flow}}| \tag{3-2}$$

$$F_{Dragy} = 6\pi\eta R(|\overrightarrow{v_{Flow}}| \cos\theta - |\overrightarrow{v_{Cell}}|) \tag{3-3}$$

However, in a thin microfluidic channel, the pressure-driven flow is not a uniform plug flow but a Poiseuille flow. The aspect ratio of channel width to channel height is 100 and therefore the flow can be considered as a plane Poiseuille flow. Since the entrance length for the flow is a small fraction of the channel length, we assume that the flow is fully developed. Fully developed plane Poiseuille flow has a parabolic profile along the z-axis. The flow rate profile is given by

$$v_{Flow}(z) = \frac{6Q}{wh^3} z(h-z) \tag{3-4}$$

where Q refers to the volumetric flow rate, w is the channel width, and h is the channel height. The average velocity experienced by the cell can be approximated as the flow velocity at the mass center of the cell. The cell is pushed to the ceiling by the upward-directed n-DEP force, so the mass center of the cell is at $h-R$. Combining equation (3-2) and (3-4), we have

$$F_{Dragx} = -6\pi\eta R \sin\theta \left[\frac{6Q}{wh^3} (h-R)R \right] \tag{3-5}$$

In the case of $h>>R$, the hydrodynamic drag force is proportional to R^2. If not, it is proportional to slightly less than R^2. Since in our case of $R \sim h$, we use equation (3-5) as our approximation of the hydrodynamic drag force.

3.4 The electrical field and the DEP force on a pair of coplanar electrodes

The other predominant force is the DEP force. We are specifically concerned with the DEP force produced by coplanar electrodes. This could be modeled as a number of different ways. We chose to simulate the electric field of coplanar electrodes using conformal mapping. Schwarz-Christoffel mapping [37] maps the potential from the parallel plate capacitor to the coplanar electrodes and provides an analytical solution for the electric field. In the model, we assume the coplanar electrodes are in an insulating microfluidic channel with channel height 20 μm and infinite channel width. The electrode width is 46 μm and the gap between two electrodes is 16.3 μm which is measured from an actual device. The simulation result of the electrical potential is shown in **Figure 3-3**. The blue lines show the equipotential lines of the electric field and the two red lines are the coplanar electrodes. As expected, the strongest field appears at the inner edges

of the electrodes. As we move further away from the electrode edges, the potential lines get farther apart, indicating that the electric field is smaller. Therefore, the n-DEP force is forcing the cell away from the central line of electrodes.

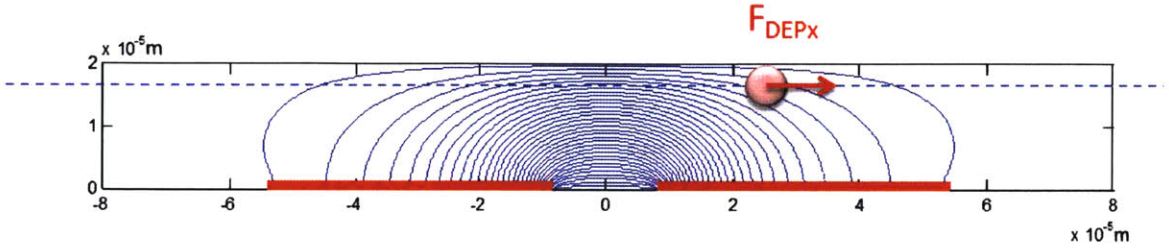

Figure 3-3 The simulated electrical potential above a pair of coplanar electrodes. The blue lines denote equipotential lines created by electrodes (red). The solution is obtained via conformal mapping as developed by [38]. The dashed blue line represents the line along which the DEP force is plotted in **Figure 3-4**.

We want to get an analytical representation of the DEP force along x (F_{DEPx}). Similar to the methods used in deriving the DEP force in different levitation height in DEP-FFF [39], the mathematical formulation of the F_{DEPx} can be given by

$$F_{DEPx} = 2\pi R^3 \varepsilon_m \,\mathrm{Re}[\underline{CM}] \frac{\partial E^2(x, h-R)}{\partial x} = 2\pi R^3 \varepsilon_m \,\mathrm{Re}[\underline{CM}] q_R(x) V_{RMS}{}^2 p(f) \qquad (3\text{-}6)$$

where $E^2(x, h-R)$ is the RMS value of the electric field strength for an applied RMS voltage V_{RMS} at location x and height h-R. The $p(f)$ is the normalized function that corrects the frequency-dependent voltage drop at the electrode/solution interface. $q_R(x)$ is a function that reflects the positional dependency of the DEP force, the shape of this function is determined by the electrode geometry: the electrode gap (g), the electrode width (w) and the channel height (h). The magnitude of $q_R(x)$ scales inversely with the cube of the electrode gap ($q_R(x) \sim g^{-3}$). Different from the DEP-FFF formulation, $q_R(x)$ in our case is size dependent. This is because different particle sizes are levitated to different heights (h-R) when they are pushed to the ceiling, so they experience slightly different electric-field gradients.

We plot F_{DEPx} as a function of x for a 5 μm radius particle in **Figure 3-4**. For x>0, the force is always positive (pointing to the right) and for x<0, the force is always negative (pointing to the left). The maximum of F_{DEPx} is at x= -10.4 μm where it is the maximum n-DEP barrier created by the pair of coplanar electrodes. We use the region where x>10.4 μm to form the force balance with the hydrodynamic force.

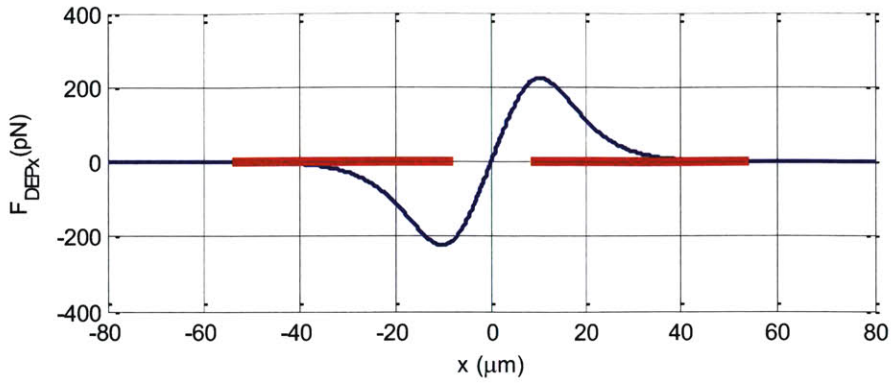

Figure 3-4 The DEP force along x direction for R=5 μm at the height 15 μm. Other simulation parameters for this plot are: $p(f)$ = 1, Re[CM] = -0.5, V_{RMS} = 7.07V, channel height = 20 μm, electrode width = 46 μm, and electrode gap = 16.3 μm.

3.5 The balance position of the two forces

After solving the hydrodynamic drag force and DEP force, we plot the two forces in **Figure 3-5** according to equation (3-5) and (3-6) to find the balance position δ at the intersections of the two.

$$\overrightarrow{F_{DEPx}} + \overrightarrow{F_{Dragx}} = 2\pi R^3 \varepsilon_m \,\mathrm{Re}[\underline{CM}] q_R(\delta) {V_{RMS}}^2 p(f) - 6\pi\eta R \sin\theta \left[\frac{6Q}{wh^3}(h-R)R \right] = 0 \qquad (3\text{-}7)$$

There are two intersections but the inner side intersection is not a stable solution because the force gradient is pushing the particle away from its equilibrium. Only the intersection greater than L, the position of maximum DEP force ($F_{DEPxMAX}$), can form a stable force balance. We define this *balance position* as δ.

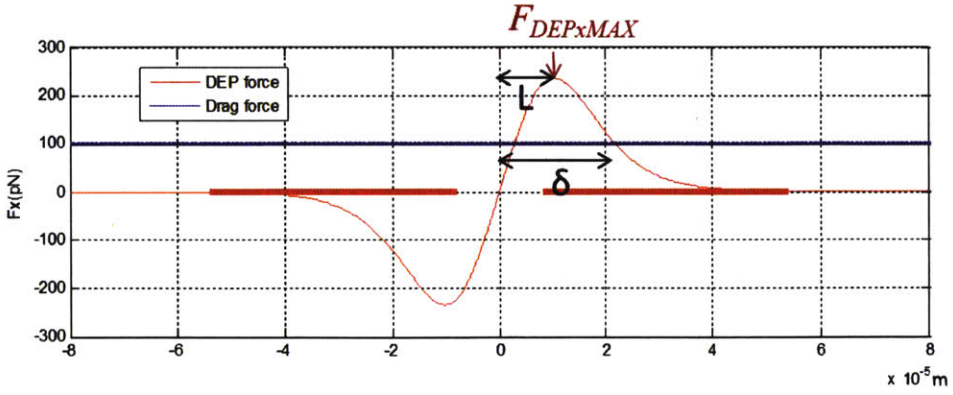

Figure 3-5 The two forces in the *x*-direction. The balance position δ is the right intersection of the blue line (hydrodynamic drag force) and the red line (DEP force) because the left intersection is not a stable equilibrium.

After reorganizing equation (3-7), we have the explicit expression of the balance position as

$$\delta = q_R^{-1}\left(\frac{3\eta \sin\theta\left[\frac{6Q}{wh^3}(h-R)\right]}{R\varepsilon_m \mathrm{Re}[\underline{CM}]V_{RMS}{}^2 p(f)} \right) \tag{3-8}$$

From this formula, we can analytically deduce the balance position from the theoretical model which we will compare the experimental result with in section 5.1. The balance position depends on the $V_{RMS}{}^2/Q$. Therefore, for the same particles if we increase the flow rate by 4 and increase the voltage by 2, the balance position should remain the same.

If we change the frequency or the media conductivity, not only the Re[$\underline{CM}$] will change but also the $p(f)$, the normalized frequency response of the system, can be accommodated from an impedance measurement [39]. We chose to experimentally compensate this effect by using known Re[$\underline{CM}$] (modeled) standard particles (polystyrene beads) as a reference to characterize $p(f)$ while estimating the Re[$\underline{CM}$] of the cells.

Unfortunately the balance position has size dependency in many places. The hydrodynamic drag force, the original DEP force formula (R^3) and the position dependent function $q_R(x)$ are all size dependent. Therefore, we need to measure R while measuring the balance position in order to obtain the Re[$\underline{CM}$].

3.6 The force ratio and the binary separation on the angle coplanar electrodes

The binary separation (pass/deflected) on the angle coplanar electrodes depends on the hydrodynamic drag force F_{Dragx} and the maximum DEP barrier $F_{DEPxMAX}$. Theoretically, if $F_{DEPxMAX} < F_{Dragx}$ the drag force will overcome the DEP barrier and make the cell pass through the electrodes. If $F_{DEPxMAX} > F_{Dragx}$, the cell could be deflected by the electrodes and hold a balance position. Therefore, we define the force ratio $F_{DEPxMAX} / F_{Dragx}$ as the criteria of the binary separation on the angle coplanar electrodes. The larger the force ratio, the larger the barrier margin it is for the cell to pass through the electrodes. The force ratio formula is given by

$$\frac{F_{DEPxMAX}}{F_{Dragx}} = \frac{2\pi R^3 \varepsilon_m \mathrm{Re}[\underline{CM}] q_R(L) V_{RMS}{}^2 p(f)}{6\pi\eta R \sin\theta\left[\frac{6Q}{wh^3}(h-R)R\right]} = \left[\frac{wh^3\varepsilon_m p(f)}{18\eta\sin\theta}\right]\left[\frac{V_{RMS}{}^2}{Q}\right]\left[\frac{q_R(L)R\,\mathrm{Re}[\underline{CM}]}{(h-R)}\right] \tag{3-9}$$

where the first term on the right hand side is the geometry and system factor, the second term is the dynamic tuning factor that can be changed during the experiment to perform different binary separations, and the last term is the intrinsic separation factor on the angle coplanar electrodes. If

two cells have distinct intrinsic separation factors (and therefore the force ratio), then theoretically, we can separate them by tuning the voltage and flow rate.

The interesting thing is the balance position can actually predict the force. That is, if from the balance position we can actually predict how much fold of flow rate we need to increase (or how much flow rate we need to decrease) to pass through the electrodes. To show this, we first decompose the position dependent $q_R(x)$ into two components

$$q_R(x) = q_R(L(R))\xi_R(x) \tag{3-10}$$

where $L(R)$ is the position where the n-DEP force has its maximum and $\xi_R(x)$ is the normalized force ratio function of the $q_R(x)$.

Therefore, the normalized function is

$$\begin{aligned} \xi_R(x) &= \frac{q_R(x)}{q_R(L(R))} = \frac{F_{DEPx}}{F_{DEPxMAX}} \\ \xi_R(\delta) &= \frac{F_{Dragx}}{F_{DEPxMAX}}, \delta = \xi_R^{-1}\left(\frac{F_{Dragx}}{F_{DEPxMAX}}\right) \\ \frac{F_{DEPxMAX}}{F_{Dragx}} &= \frac{1}{\xi_R(\delta)} \end{aligned} \tag{3-11}$$

⇨ We can deduce the force ratio from the balance position with the modeled normalized force ratio mapping $\xi_R(x)$. We plot the balance position as a function of force ratio in **Figure 3-6**.

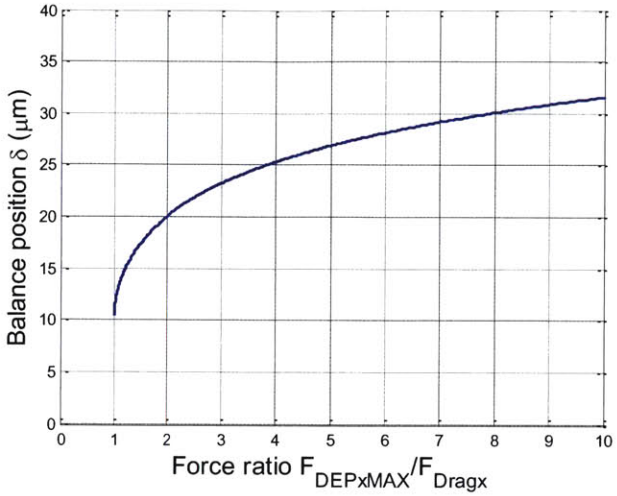

Figure 3-6 The balance position δ as a function of force ratio $F_{DEPxMAX} / F_{Dragx}$. The balance position to the force ratio mapping depends on the $\xi_R(x)$. The figure is plotted with R = 5 μm.

$\xi_R(x)$ is size dependent, which means we cannot deduce the absolute force ratio without the information of size. However, the size dependency of $\xi_R(x)$ is small. We explicitly plot $\xi_R(x)$ for different sizes in **Figure 3-7**. We find out that the maximum of $\xi_R(x)$ is in similar positions L, which is 10.4 μm (with less than 0.5% error for R=1~7 μm). The maximum deviation of $\xi_R(x)$ is <3% in magnitude. However, if we plot the deviation in percentage compared to $\xi_{5\mu m}(x)$ (**Figure 3-8**), the deviation is less than 14%. This means if the cells are in the same balance position, their force ratio is approximately the same (<14%) regardless of the sizes. Therefore, we can approximately deduce the force ratio of two cells (and therefore the separability) given by the balance position difference even without the cell size information.

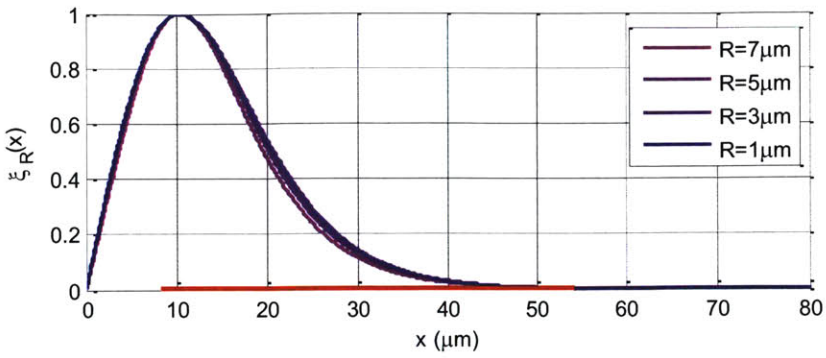

Figure 3-7 The normalized force ratio function $\xi_R(x)$ for different sizes. The size dependency of $\xi_R(x)$ is small. The maximum deviation between different lines is at ~20 μm, where they are ~3% difference in magnitude.

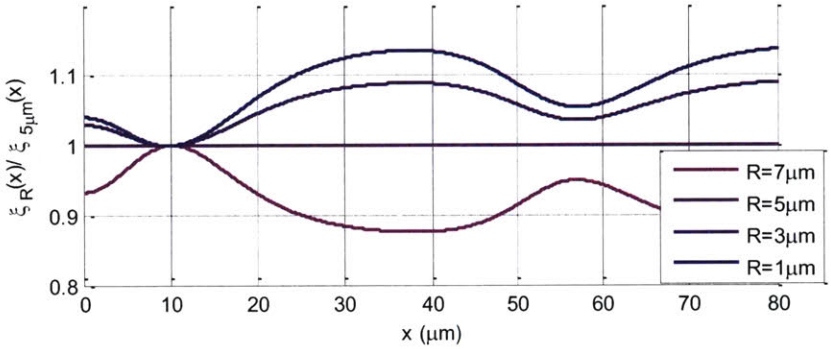

Figure 3-8 The deviation percentage of $\xi_R(x)$ compared to particle of R=5 μm We compare the ratio between the $\xi_R(x)$ and $\xi_{5\mu m}(x)$. The deviation is less than 14% in percentage.

It is worth noticing that the size dependent effect of $\xi_R(x)$ can be eliminated using a top-down parallel electrodes geometry because cells with different sizes would be in the same plane ideally.

3.7 Other forces

There are other forces that have been neglected in our analysis, including the friction force and the electro-thermal hydrodynamic flow. For sticky cells like activated neutrophils, the friction force on the ceiling might not be negligible. The friction force should be the same along the x-direction. Therefore it might form an offset to the proposed hydrodynamic drag force. In high-conductivity media or at high voltage, the electro-thermal hydrodynamic flow can be severe. Or if there is a conductivity gradient in x-direction, the imposed gradient electro-osmosis will also introduce electric hydrodynamic flow. The overall effect will change the flow rate profile and therefore distort the hydrodynamic force in **Figure 3-5** and result in a different balance position to electrical properties mapping. If the cell still remains on the ceiling, then we can introduce the

third force into our model where keeping the DEP force and hydrodynamic model the same like equation (3-12).

$$F_{DEPx} + F_{Dragx} + F_{Other\_x} = 0 \tag{3-12}$$

If our model is accurate, we can quantify the third force experimentally using the n-DEP spring method and standard particles of known size and Re[$\underline{CM}$] using equation (3-13).

$$\delta = q_R^{-1}\left(\frac{6\pi\eta R^2 \sin\theta\left[\frac{6Q}{wh^3}(h-R)\right] - F_{Other\_x}}{2\pi R^3 \varepsilon_m \mathrm{Re}[\underline{CM}] V_{RMS}^{\ 2} p(f)}\right) \tag{3-13}$$

For effect of the electro-thermal hydrodynamic flow, Mike Vahey did the analysis of the force near the L in his PhD thesis [40]. The approximate force ratio between the two is given by

$$\frac{F_{DEPxMAX}}{F_{tEHD}} \approx \frac{R(10^3 W/m)}{hV_0^2\sigma_m}|\mathrm{Re}[CM]| \tag{3-14}$$

where the F_{tEHD} is the drag force from electro-thermal hydrodynamic flow and σ_m is the conductivity of the media. Therefore, in lower voltage and conductivity, the effect of the electro-thermal effect will be insignificant.

3.8 Conclusion

In this chapter we derived the analytical model of the hydrodynamic force, the n-DEP force and the balance position. After characterizing the system with a standard (known) particle, we can deduce the Re[$\underline{CM}$] of the cell with the size information. We found that we can also deduce the binary separation criteria on the coplanar electrodes, which is the force ratio between the maximum n-DEP barrier and the hydrodynamic flow, using the balance position. In the next chapter, we are going to integrate the n-DEP spring into an automated system for DEP characterization in different frequencies and media conductivities. The various characterization results can eventually assist in finding the optimal separation conditions between different cell types.

Chapter 4: Development of an automated system for force measurement

In the previous chapter, we introduced the model of the balance position method for measuring the electrical properties of the cells. The DEP force on the cell depends on the frequency and the conductivity. **Figure 4-1** shows a n-DEP force map as a function of frequency and conductivity. We want a DEP characterization system that can find out the optimal separation condition for different cell types. Therefore, for a complete characterization, we need to measure the DEP forces in different conditions. However, changing the condition for the cells, especially the media conductivity, is a time-consuming work, which could take hours to days. Furthermore, changing the cell media requires centrifuging steps that can result in sample loss or potentially influence the electrical properties of cells. Most importantly, since the electrical properties of some cell types are time-sensitive, such as the activation level of neutrophil, and apoptosis, we want the characterization time of these cells to be as short as possible. Therefore, in this chapter, we will describe the automated system we developed for high-throughput DEP characterization for cells, which can measure the DEP force across different frequencies and conductivities on thousands of cells within an hour. We will demonstrate the use of this system in sections 5.2 and 5.3.

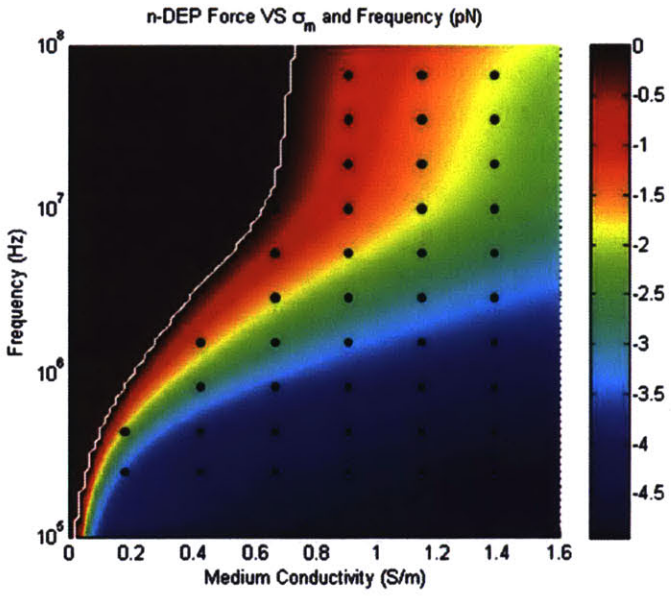

Figure 4-1 n-DEP force map as a function of frequency and conductivity.

The white line is the cross-over frequency line and the left side of this line is the region of p-DEP where we cannot measure using n-DEP spring. The right side of the line shows the colors which represent the value of the n-DEP force (pN). The black dots are the tentative operation condition from which n-DEP spring method measures. The simulated particle is the normal human white blood cell with the double shell model [55].

4.1. Overview of the automated system

The automated system includes four main parts: the fluidic control, the electrical control, and the optical control, and the imaging software (**Figure 4-2**). The automated system is meant to provide flexible configuration and wide capability. We are able to control the flow rate, conductivity and even conductivity gradient with a computer-controlled fluidic system. We can

also apply a frequency sequence to the electrodes using low frequency (DC-20MHz) or high frequency (10MHz-1GHz) electrical signals. We can control the camera, taking pictures or videos whenever we want. Finally, we can record images or videos as well as the time and other parameters for each frame. There are several instrumentation software packages on the market, such as LabView which offers strong instrumentation control and GUI. However, we decide to use Matlab to control all the automated system because of its strong image processing module and convenience of its programming language. We will describe how we implement each sub-system in the following sections.

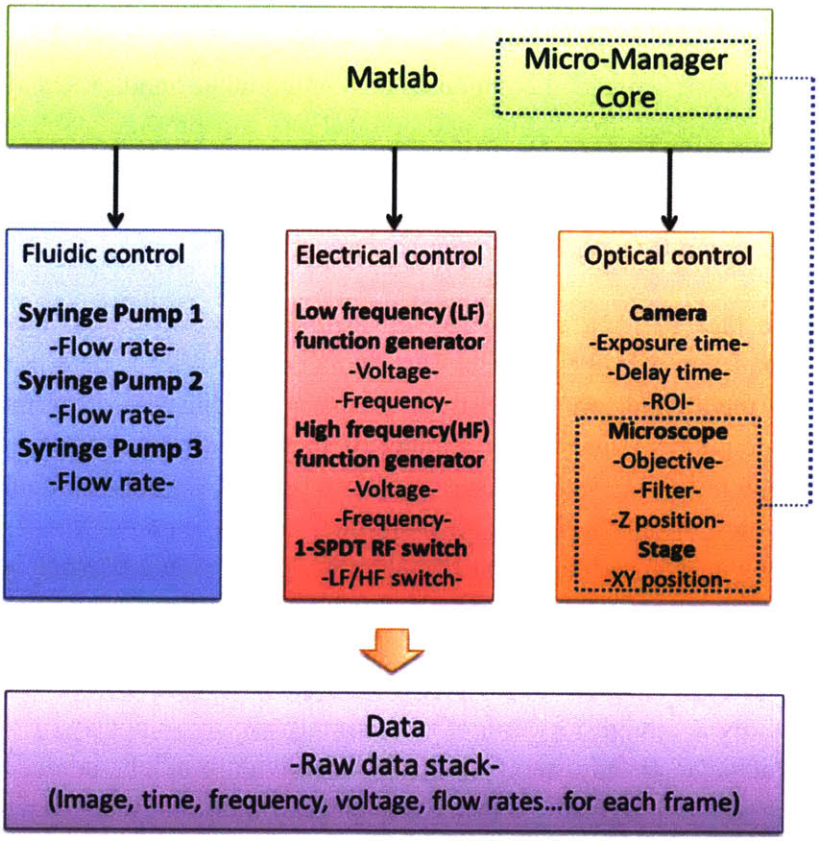

Figure 4-2 The overview of the automated system

The Matlab controls all the equipment with parameters. The image and other parameters for each frame are recorded for processing. The microscope is control with Matlab script but requires importing the Micro-Manager Core.

4.2. Fluidic system

The goal of the fluidic system is to control the media conductivity dynamically to measure the n-DEP force in different conditions. While the n-DEP spring method does not require a spatial media conductivity gradient, since the initial motivation of this fluidic system was generating a dynamic conductivity gradient for iso-dielectric separation, this section will mainly focus on the development of generating the conductivity gradient.

Design choice: People have demonstrated dynamic control of solute concentrations using a variety of methods. For example, Toner's group used an on-chip valve to switch between two constructed conductivity gradient [41]. They can achieve short transient times (a few seconds)

because the gradient is already generated. The other approach is by playing with the flow rates of syringe pumps to dynamically mix four high concentration and low concentration liquids to generate the conductivity [42][43]. This approach has a longer transient time (~1 min) but provides more flexibility for the concentration gradient (the ratio of two of the flow rates is adjustable). We choose to use the idea of the later because its flexibility of providing ideally arbitrary linear conductivity gradient for experiments.

The next question is the fluidic source. Pressure control or flow control flow in fluidic domain is an analog of voltage control or current control in electrical domain. The pressure control method requires a stable pressure source, a computer-controlled pressure regulator, and if the resistance of the system is not constant an additional flow rate sensor with feedback loop can assist to achieve more stable flow rate, but this is an added complications. On the other hand, direct flow rate control by syringe pumps and leakage-free tubing and connections can provide stable and high-precision flow rate control. Since the n-DEP spring method and IDS both require stable and accurate flow rates for computing the electrical properties or determining the separation distribution, we chose the syringe pump flow control system for our system.

Implementation: Similar to the idea of [42], we change the flow rates of several pumps to control the media conductivity and the overall flow rate. The media conductivity is determined via mixing of high conductivity media and low conductivity media with adjustable flow rates. Essentially, the number of syringe pumps equals to the number of variables we want to control. If we just want to control the flow rates, we need one syringe pump only. If we want to control the flow rate as well as the conductivity of the media, then we need two syringe pumps. If we want to control the flow rate plus an adjustable spatial conductivity gradient, we need at least three syringe pumps.

Creating a liquid with a single, intermediate, uniform conductivity from two input liquids of low (σ_{MIN}) and high (σ_{MAX}) conductivity is straightforward. We can simply mix σ_{MIN} and σ_{MAX} with different flow rate ratios. To achieve an adjustable spatial conductivity gradient across the channel, we can create two controllable intermediate media streams and then mix them together to form the gradient. Using four syringe pumps to control two intermediate media streams is trivial. We have developed a new way to control the two conductivities (σ_H, σ_L) and the total flow rate (Q) with only three syringe pumps. A schematic of the fluidic system is shown in **Figure 4-3**. The relation between σ_H, σ_L, Q and Q_1, Q_2, Q_3 is given by

$$\begin{pmatrix} 2Q \\ Q\times\sigma_H \\ Q\times\sigma_L \end{pmatrix} = \begin{pmatrix} 1 & 1 & 1 \\ \sigma_{MAX} & \sigma_{MAX} & \sigma_{MIN} \\ \sigma_{MAX} & \sigma_{MIN} & \sigma_{MIN} \end{pmatrix} \begin{pmatrix} Q_1 \\ Q_2 \\ Q_3 \end{pmatrix} \tag{4-1}$$

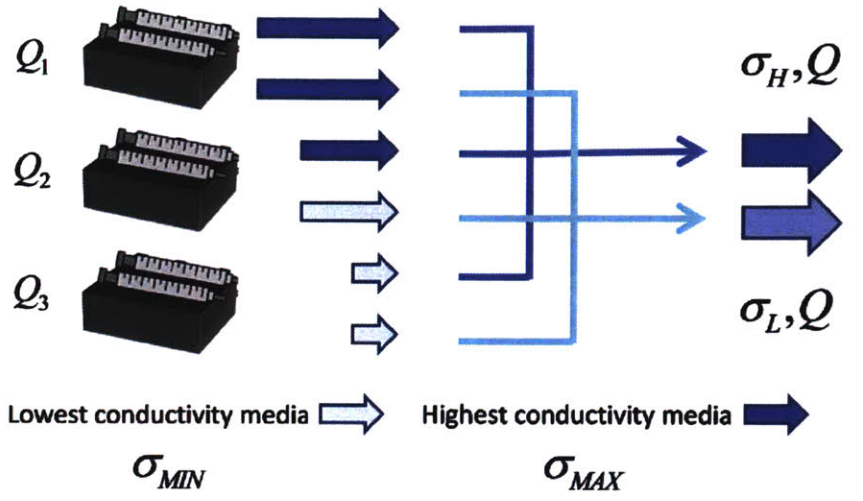

Figure 4-3 The scheme for the tri-pump system.

We can dynamically control the two intermediate conductivity σ_H and σ_L and the total flow rate Q using three syringe pumps. Each syringe pumps contain two syringes with the conductivities (σ_{MAX}, σ_{MAX}), (σ_{MAX}, σ_{MIN}) and (σ_{MIN}, σ_{MIN}) and with flow rate respectively.

We programed all the syringe pumps using we use serial commination command in Matlab. The syringe pump models we have are KD scientific 200, Harvard Apparatus PicoPlus HA11, and Chemyx Fusion Touch 200. The experiments shown in this chapter were done with three KD scientific syringe pumps. The experiments in chapter 5 were done with Chemyx Fusion Touch 200.

Since the computer we use only has one RS232 serial port but several USB ports, we use a USB to RS232 adapter to control the pumps. The KD scientific 200 and Harvard Apparatus PicoPlus HA11 pumps are connected to the computer through the RS232 serial port. They can be linked together with a daisy chain so that we only need one RS232 port to communicate with all of them. The Chemyx Fusion Touch 200 connects to the computer directly through a USB port.

Characterization:

To demonstrate the ability to control the conductivity gradient, σ_H and σ_L, we use a fluorescein solution in DI water to mimic high-conductivity media to verify the concentration profile through images. The device we use to verify the concentration gradient is in **Figure 4-4** (20 μm x 2 mm x 5 cm). We observe the concentration at the red rectangle region using computer control microscope (Zeiss AxioImager) and camera (LaVision SensiCam). We first show that we can

generate different gradients and then we discuss the long term and short term response of the system.

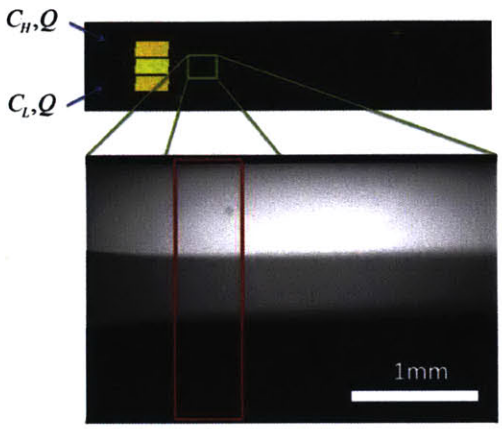

Figure 4-4 The micro-mixer microfluidic device for demonstrating the dynamic concentration gradient control. Two liquid streams with different fluorescein concentrations go into the microfluidic channel through a mixer that generates three streams. The image shows the three streams after entering the channel. The upper part shows the AutoCAD layout of the micro-mixer which we used to generate the conductivity gradient. Intensities in the red rectangular region are used for quantitative analysis in .

In the first experiment, we used 1 mM fluorescein as our C_{MAX} (analogous to σ_{MAX}) and DI water as C_{MIN} (analogous to σ_{MIN}). We used our fluidic system to create two input concentrations, a high-concentration media C_H (analogous to σ_H) and a low-concentration media C_L (analogous to σ_L). Firstly, we changed the C_L while kept C_H the same to the concentration gradient with different slopes [**Figure 4-5**(a)]. Secondly, we changed the C_H while kept C_L the same to the concentration gradient with different slopes [**Figure 4-5**(b)]. The image intensities were compensated by the optical gain of the imaging system, which we obtain from the image of a fluorescein stream with concentration 1 mM. In addition, the system was allowed to reach steady state by waiting 2 min before taking the images with the flow rate of 4 μL/min. The results show that the low [(**Figure 4-5**(a)] and high [(**Figure 4-5**(b)] concentrations can be changed while inducing minimal change (<5%) in the other (constant) concentration. The middle stream's concentration adopts the expected intermediate intensity.

In a second experiment, we show that the gradient we generated can last for 3 hours with very little deviation (CV<1.5%) (**Figure 4-6**). Here we set up a concentration gradient and let the system run for 3 hrs, recording images every 1 min. The images were compensated for light intensity instability of the microscope (CV~4%) by dividing the overall light intensity factor (sum of the intensity divided by mean of the sum of the intensity) of each image. We extracted time traces of the intensity at five locations transverse to the fluid flow. The time slopes of these lines are -0.0025, 0.0026, 0.0025, -0.00031, and 0.00014 (intensity/min) from position 0.33 mm to 1.67mm, respectively, and show that the gradient has little-to-no time drift.

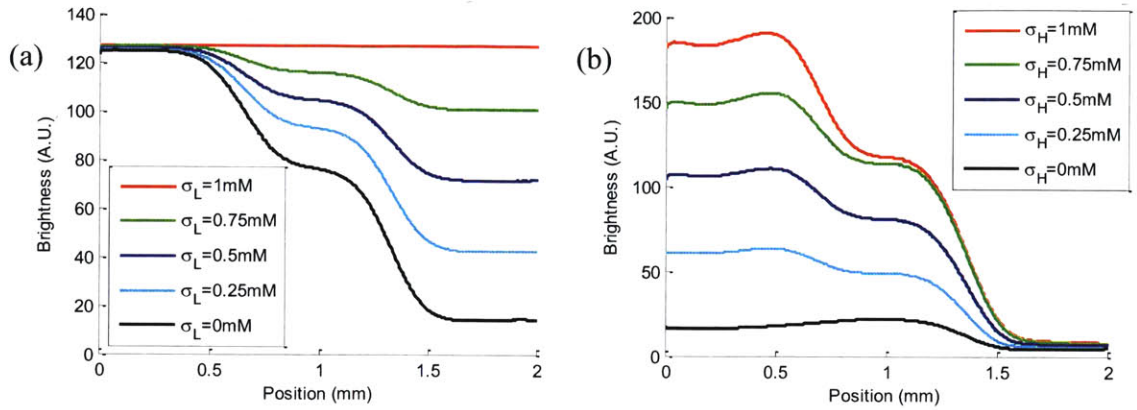

Figure 4-5 The dynamic control of concentration gradient system. (a) Control the high intermediate conductivity stream $\sigma_H(C_H)$ (b) Control the low intermediate conductivity stream $\sigma_L(C_L)$. The plots show intensity on the cross-section in the middle part of the microfluidic channel in device in **Figure 4-4**.

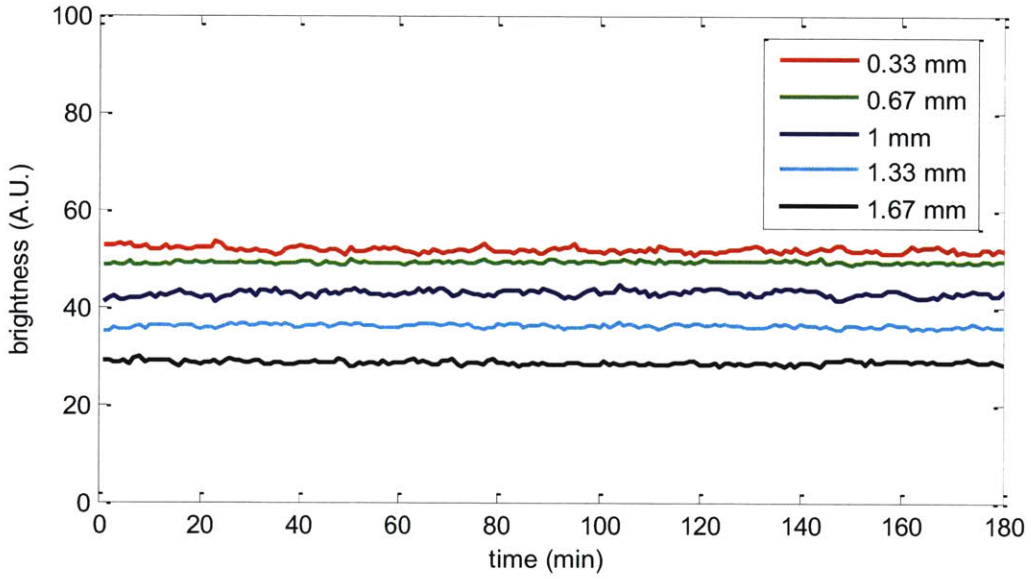

Figure 4-6 The long term response of the conductivity gradient. The image shows the intensities at 5 different lateral positions of the concentration gradient for 3 hour duration. The long-term response shows this system is very stable over times. We observe little variation (CV<1.5%) along the time axis.

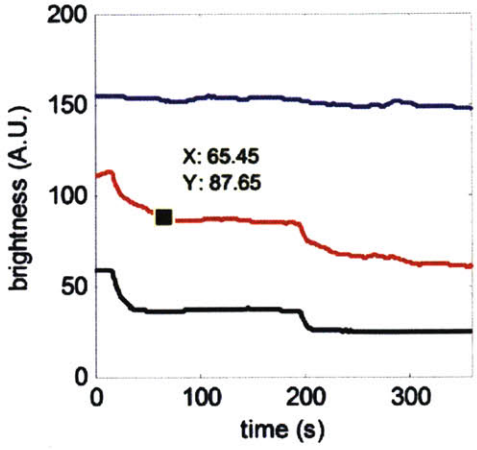

Figure 4-7 The short term response of the conductivity gradient. The image shows the intensities at 3 different lateral positions of the concentration gradient for 360 seconds. The conductivity gradient was programmed to change at t=0 s and t=180 s. The first twenty seconds was the transient time for dead volume and the later 40 second is the time for waiting the concentrations to reach their steady states. The flow rate used for each stream was 3 μL/min.

In the third experiment, we used 10 μM fluorescein as our C_{MAX} and DI water as C_{MIN}. We imaged the fluorescence intensity near the beginning of the channel (**Figure 4-7Error! Reference source not found.**) to quantify the transient time for the new concentration gradient reach the beginning of the channel. The flow rate (Q) each is set to 3 μL/min. There is some void volume in the mixer and tubing (~ 2 μL) that result in a delay time ~20 seconds and it also takes time ~40 seconds to reach steady state. The overall transit time between initiation of the command and observation of the profile change in beginning of the channel is ~ 60 seconds.

With the dynamic control of the conductivity, we are able to measure the electrical properties of the cell in different conductivities. However, in the n-DEP spring method, we do not really need to generate a dynamic conductivity gradient. We can either set up a fixed spatial conductivity gradient and image the balance position at different part of the electrodes or use a uniform conductivity at a time and change it temporally.

4.3. Electrical system

The goal of the electrical system is to control the DEP force with different frequencies and voltages. We use commercial computer-controlled function generators as our electrical source. We have a low-frequency function generator and a high-frequency function generator that are linked to a computer-controlled single-pole double-throw RF switch as the output signal. We control the low-frequency function generator and the RF switch via a USB connection and the high-frequency function generator through the USB-RS232-adpater. The electrical signal is conducted in a 50 ohm co-axial cable with BNC or SMA type connectors to minimize interference and transmission line loss.

The low-frequency function generator (Agilent 33250 A) can supply from DC to 20 MHz output. The maximum output signal is 20 Volt peak-to-peak with output resistance 50 ohm. The high frequency function generator (TTi TGR1014) can supply 10 MHz to 1000 MHz but the output voltage is ~500 mV, which is not enough for DEP separation, so we use a high-power amplifier (Mini-Circuits ZHL-20W-13+) to boost the output voltage by 50 dB. Since the amplifier output has a DC offset component that occasionally appears when changing frequencies transition, we use a DC block (block under 300kHz) to avoid passing DC that could cause the electrodes to corrode. The RF switch (Mini-Circuits USB-1SPDT-A18) enables us to switch between the high-frequency and low-frequency function generators as the signal source.

With the electrical system, we are able measure the electrical properties of the cells at different frequencies. However, across different frequencies, the actual voltage loaded into the device is not the same due to parasitics in the system. Therefore, we characterized the frequency response of the electrodes using an impedance analyzer (Agilent 4294A). We flowed media of different conductivities (1.6S/m, 0.8S/m, and 0.3S/m) through the device (which we will describe in section 5.1) and measured the frequency response of the electrodes (**Figure 4-8**). As expected, the magnitudes [**Figure 4-8**(a)] at lower frequencies are inverse proportional to the conductivity of the media (L, M, H = 357, 124 70 Ohm at 1 MHz). In terms of the phase [**Figure 4-8**(b)], at 10 MHz the phase of the low conductivity media is more negative than the higher conductivity media because the frequency is reaching its cutoff frequency and reducing the phase. For lower conductivity media, the cutoff frequency is lower so the magnitude drops faster than higher conductivity media. We also varied the flow rate from 1 μL/min to 8 μL/min and found that variation in the impedance due to the different flow rates is negligible (not shown).

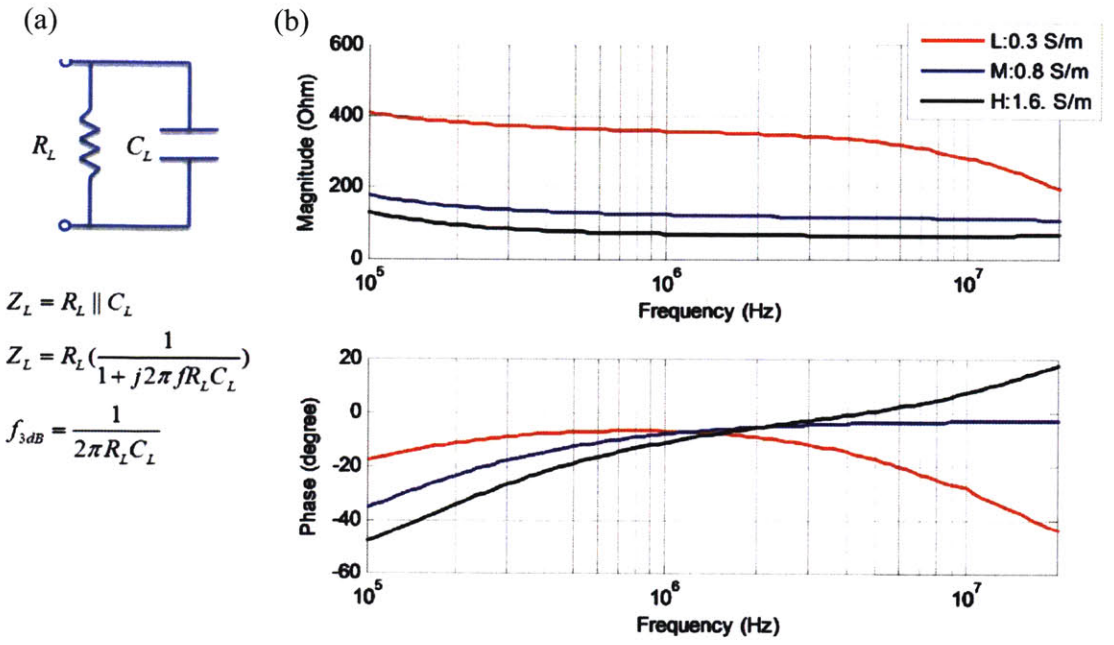

Figure 4-8 The frequency response of the parallel electrodes in different media conductivity.

(a) A simple parallel RC model for the parallel electrode with media. In this model, the impedance in lower frequencies is resistance, which is inversely proportional to the media conductivity. The cut off frequency f_{3dB} is inversely proportional to the resistance value and the capacitance value. **(b) The magnitude of the impedance**, plotted in the range of interest (100kHz to 20MHz)**. (c) The phase of the impedance** across the same frequencies as in (b)**.**

The data we have can explain the conductivity and frequency dependency effect of the balance position in the n-DEP spring measurement. However, we did not use the spectra in **Figure 4-8** to compensate the balance position measurements. Instead we used relative measurements of beads to dynamically characterize the frequency response of the system, since the actual voltage drop in the bulk media changes with frequency and media conductivity.

Although our electrical system can control frequency up to 1GHz, operation above 100 MHz would require use of microfabricated electrodes and connections suitable for high-frequency operation. We have developed such electrodes in collaboration with colleagues at Lincoln Laboratory, but they are not the focus of this thesis.

4.4. Optical system

The software and driver compatibility for the microscope and cameras is the main issue that we found in trying to build an integrated optical system. In particular, we encountered several challenges in finding compatible drivers and software to control the camera.

Our camera is a LaVision QE which also known as the PCO Sensicam QE camera. The software development kits (SDK) for the camera PCO camera (sensicam / dicam pro / hsfc pro SDK for WindowsXP/7 (32/64bit) does not support Matlab API (Matlab4sensicam) using the new driver (WindowsXP/7(32/64bit)). Therefore, if we want to control the camera through Matlab, we could only install the old driver and the old SDK (sensicam software development kit (SDK) for Windows9x/ME/NT/2000). The caveat is that with the old driver Matlab works but the imaging software provided by the company (PCO Camware) cannot execute. The company is working on writing the new Matlab API for the WindowsXP/7(32/64bit) driver but it has not been released at the time of this thesis writing. Another option we considered is to use the open source microscopy software Micro-Manager with Matlab to control the camera with the new driver. However, Micro-Manager (v. 1.3 or 1.4) has a bug in the live imaging function and offers no option for changing the camera mode (fast mode/ continuous mode/ normal mode). Therefore, we decided to use the old driver (Windows9x/ME/NT/2000) with Matlab API to control the camera because it is the only option that we can use the camera with Matlab without writing our own API. The downside of it is whenever we want to use the Camware software, we need to change the driver to the new one.

We wrote a Matlab graphical user interface (GUI) program for controlling the camera, which provides options for changing the region of interest (ROI), binning level, exposure time, and bit depth. The recorded video stack is in stored in a Matlab matrix so it can directly be processed with temporal or spatial filters.

For the microscope (Zeiss Axio Imager.m1m) and the stage control (MAC 5000), we first installed the MTB2012 server for Zeiss. They offer the API for controlling all the parameters of the microscope and the stage. In order to use Matlab to control the microscope and stage, we choose to incorporate Micro-Manager 1.4 since it offers some useful functions like pixel calibration, scan-and-stich, autofocus, and other existing plug-in or Macros, which could save us time for developing new functions.

With our optical system, we are able to switch between different imaging modes. The system can image the device in bright-field and then switch filters for DIC imaging or other fluorescent channels (TRITC, FITC, DAPI...). This allows us to obtain multi-dimensional optical information as well as the balance position information. Having this multimodal information in turn allows us to study the correlation between optical and electrical properties of the cell. We can also change the x-y position and tune the z position to autofocus the microscope, which allows us to measure the balance positions at different locations of the electrodes. Finally, though

not implemented in our current software, it is straightforward to add the ability to switch objectives to the system.

4.5. The graphical user interface of the automated system

After linking all the components to the computer, we wrote a Matlab GUI that not only controls each of the components but also provides some protection of the device (avoid illegal inputs and conditions that could cause electrode electrolysis). The GUI (**Figure 4-9)** consist of two menus (File and Setting) and three blocks (Video display, Control panel and Macro panel).

The File menu has the "Save as" and "Save" items. "Save as" provides the path, file name, and the videos options. "Save" is simply put the video stack and parameters into the assigned path. "Setting" has the camera setting that can change the region of interest, binning, gain, expose time, delay time and bit depth (8 bits or 12 bits).

The Video display shows the real time image acquired from the camera. The frame rate, frame number and the elapsed time is shown below the video box. The control panel (**Figure 4-10**) includes the individual fluidic, electrical, and optical units. The frequency of the low frequency function generator is set above 100kHz to prevent electrolysis. The Macro panel (**Figure 4-11**) provides the following function:

(1) Voltage Sweep: Change the voltage of the function generator and record the video for each voltage. The length of the video is assigned in the "File-> Save as" menu. The raw data will be automatically saved with incremental names.
(2) Frequency Sweep: Change the frequency of the function generator and record the video of each frequency. If the frequency is between 100kHz to 15MHz, we choose to use the low frequency function generator. If the frequency if between 15MHz to 1GHz. We choose to use the high frequency function generator.
(3) Single Cell Frequency Sweep: Apply a continuous frequency sweep to the electrodes (chirp signal). A single cell will experience different frequency while traveling in the region of interest.
(4) Frequency and conductivity sweep: Provide a two dimensional scan for frequency and conductivity. The conductivity is controlled by the flow rates of the pumps.
(5) Auto Scan: A user-defined scan.
(6) Customized Frequency Sequence: To apply frequency sequence with assigned duration and record a video stack with parameters. The "Current Status" will display the current voltage and frequency of the signal.
(7) Execute Customized Frequency Sequence Stack: To apply a few frequency sequences with assigned duration and record a few video stacks.

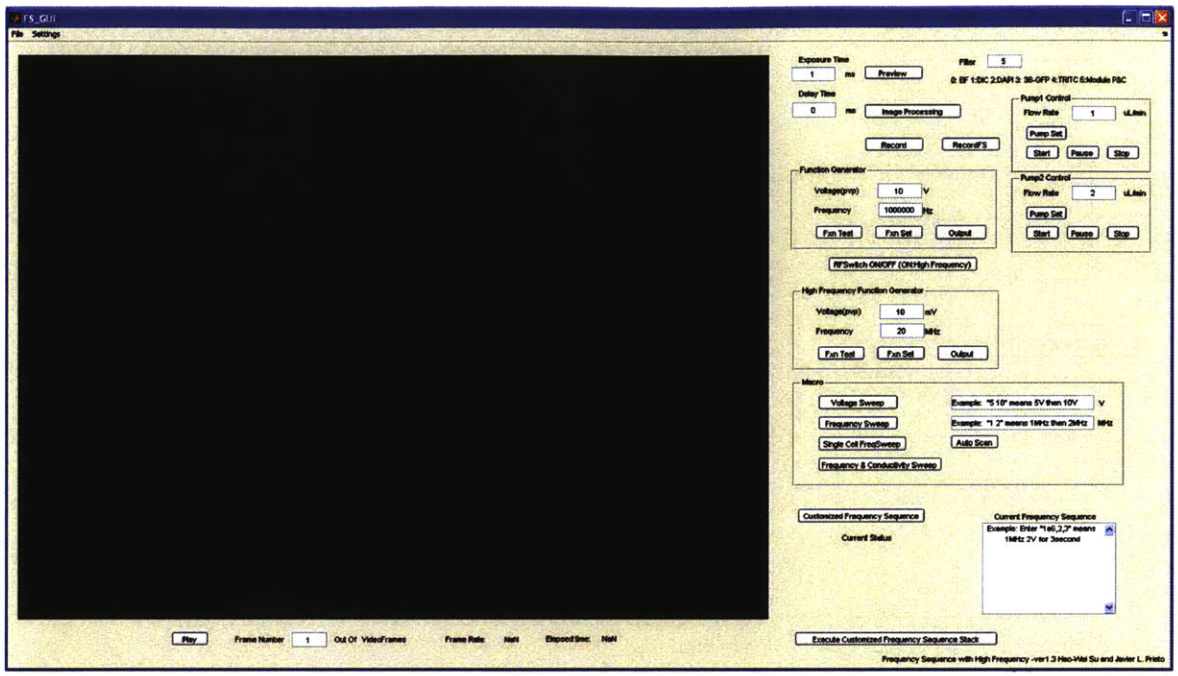

Figure 4-9 Matlab GUI for automated system.

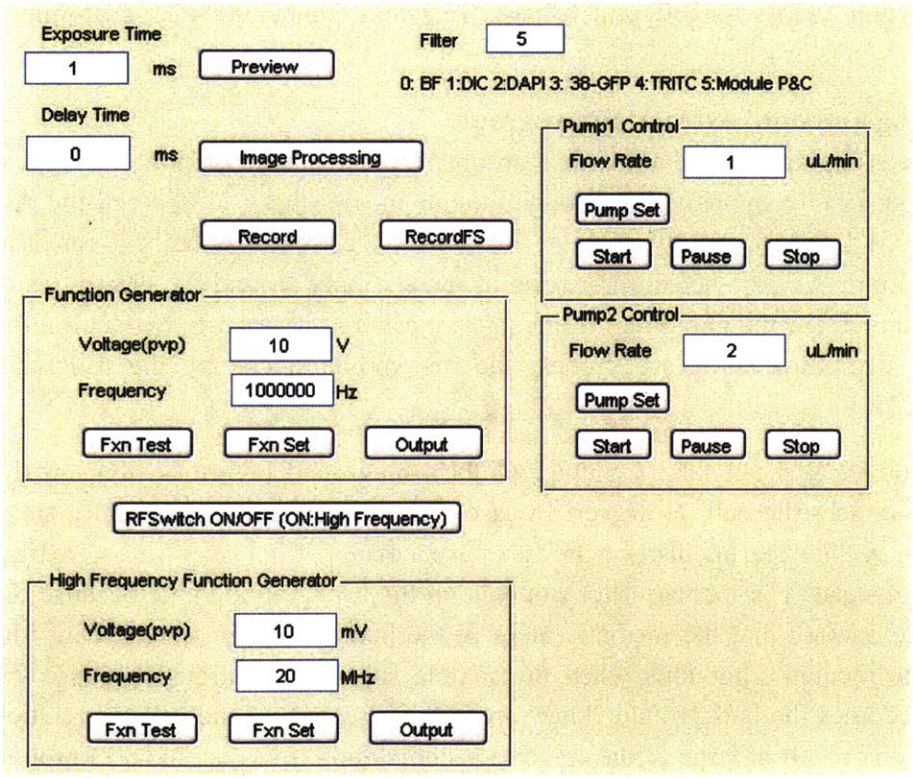

Figure 4-10 The control panel of the Matlab GUI.

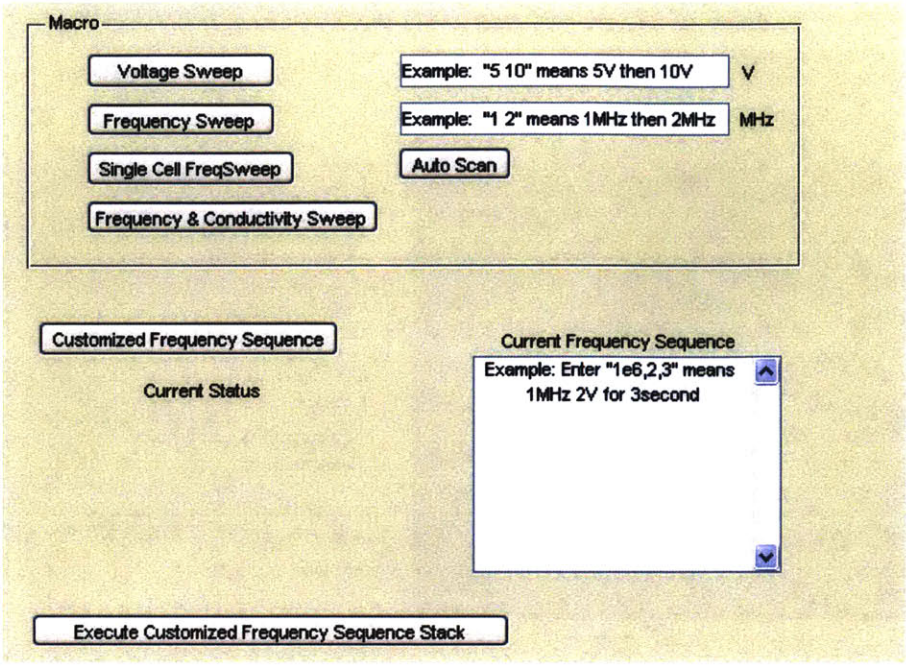

Figure 4-11 The Macro panel of the Matlab GUI

Useful Macros for recording videos for different voltage, frequency, conductivity, or customized frequency sequence.

4.6. Image processing and data extraction program

Our goal in image processing and data extraction is to obtain the balance position and optical information (e.g., size, shape) of the particles through the raw movie stacks. We record the raw movie from the Matlab GUI. We physically align the camera and electrodes so that it is easier to extract the balance position. We also select the region of interest only around the electrodes to reduce the file sizes and increase the maximum frame rate we can get. In order to extract out the balance positions and size information we process the raw movie stacks by the following procedures as **Figure 4-12**.

(1) Finding background: We can take a picture of the background before turning on the electric field to deflect the cell. However, in case of lighting stability or slightly stage movement between the experiments, we choose to use a median filter over time to extract the background instead. The median filter can pick up the background value because the particle is sparse enough that the median values of the pixels over time are usually the background. The median filter fails when the sample is too concentrated because the median value becomes the background. There are some cases where the cells were stick to the electrode and result in large erroneous data accumulation if we use the background beforehand. The median filter will consider the cells as the background and do not count the data in. However, if the cells happened to stick to the electrodes during the recording and then median filter cannot help as well. We need to use further signal processing to

remove the artifact. Fortunately, the phenomena do not happen often if we soak the device with BSA to minimize surface adsorption.

(2) Finding the central line of the electrodes: We tried the Hough transform to extract out the line and angle of the electrodes and then average the position of the two electrode edges to get the central line. However, for convenience and consistency, we align the electrodes at the center of the field of view so that the central line is mid-line so we can skip the Hough transform to fasten the computation and reduce the uncertainty of the edge detections. The error that could happen in finding the central line is ~0.5 pixel (1 pixel = 1.07 μm in our experiments).

(3) We subtract the background from the raw image and take the absolute value to get the image of the moving objects. We normalize the result with the intensity of the electrode intensity value (obtained from the background). Then we threshold the image to get binary image. For determining the threshold value, we tried the *GRAYTHRESH* function in Matlab which use the Ostu's method[44] to choose the threshold by minimizing the intraclass variance of the black and white pixels. The threshold value, however, depends on the number of cells and beads in each image. Therefore, we choose a threshold value (0.05) for all the images because it is the value return from *GRAYTHRESH* function applied on an all cell image.

(4) We identify the connected components in the binary image using the *BWCONNCOMP* function in Matlab which connects the nearby pixels have the same value and form the objects. We use the connectivity of 4 which connects the pixel in 4 (up/down/right/left) directions. The identified objects are mostly the cells. Sometimes, the threshold will capture small regions from the thermal noise (very little) so we add an additional filter to collect objects that have an area larger than 4 pixels.

(5) After identifying the objects, we use the Matlab command *REGIONPROPS* to extract the properties of each object, including centroid (for calculating the balance position), filled area (if the cell has some hollow region inside, it will be filled and counted), mean intensity and eccentricity. We also record the time, the frequency, and the voltage we used for each image. Then we crop the images for the objects with 21 x 50 pixels (1 pixel = 1.07 μm) and save them individually for future examination. We identify connected regions to get the particle area. We obtain the centroid of the particle area to determine balance position of the particle. The maximum error of measuring the balance position is ~0.5 pixel.

After the image processing, we acquire the multi-dimensional data matrix from the video. Each particle has its image index, its particle parameters (centroid, area, mean intensity, eccentricity) and its system parameters (time, frequency, voltage).

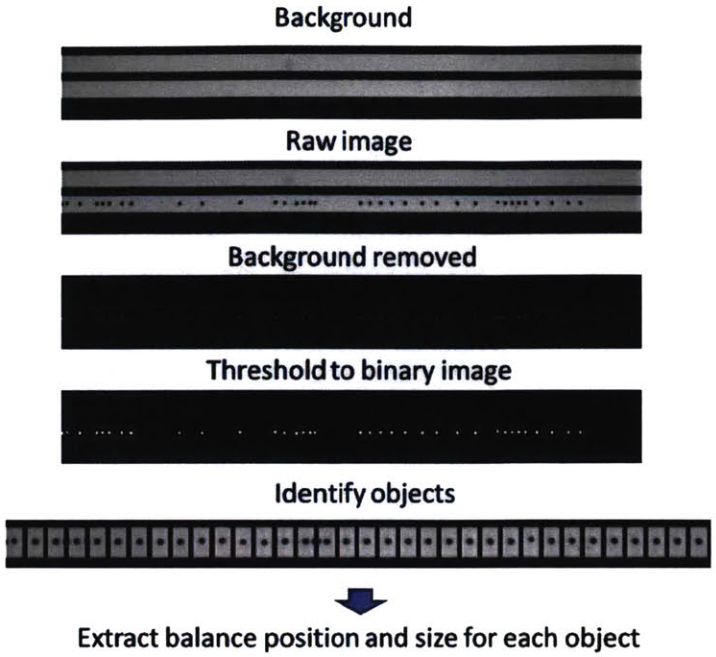

Figure 4-12 The image processing for extracting the objects on the electrodes. The background of the video is found via temporal median filter and removed from the raw images. The resulting images are normalized with their original light intensities on the electrodes and converted to binary images with a threshold determined by Ostu's method [44]. The cell objects were identify from the binary images and cropped into 21 x 50 pixels images (1 pixel = 1.07 μm).

One metric that we extract is the particle area. The particle area we obtained is not exactly the true size of the particle. The particle area depends on the threshold value, the light, imaging channel, focusing, and particle material. Here we discuss the uncertainty and accuracy of the size measurement below.

The uncertainty of size measurement:

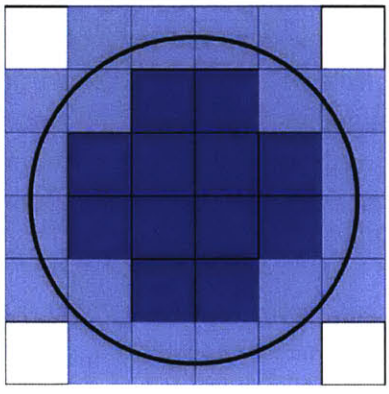

Figure 4-13 The uncertainty of measuring the size of a cell.

The black circle is the real cell object. The dark blue area is the certain area (A_C) and the light blue area is the uncertain area (A_U), which can be counted or not based on the algorithm (threshold). The real object size is in between A_C and A_C+A_U.

The accuracy of the measurement of cell size and balance position depends on the pixel size. From **Figure 4-13**, we can calculate the uncertainty of the area as (A_U/ A_C+A_U). The smaller the pixel is, the smaller the uncertainty of the area. Similarly, the balance position also has the uncertainty ~ 0.5 pixel as evidence as moving the real object upward ~ 0.5 pixel can still get the same discretized area. The pixel size to cell radius diameter ratio for our case is about 1:10 and therefore our uncertainty of radius measurement is around 10% and area measurement is around 20%. We can reduce the error by having higher resolution images.

Accuracy:

However, even with higher resolution, the error between the real object and measured object will not reduce to infinitesimal. The resulting image is a convolution between the real object and point spread function of the optical system. Therefore, the edge of the particle is blurry and creates uncertainty in area in this case. The error comes in for these indecisive edges. The accuracy thus depends on the threshold value we use.

We show the cell image we obtained and measure its size by different normalized threshold **Figure 4-14**. Different threshold will affect the size by 50%. Therefore determining the right threshold in important. In this thesis, we use the normalized threshold of 0.05 where Ostu's method gives a similar value around 0.067 for the cell.

Figure 4-14 The effect of different threshold to the area measurement from cell image. (a) The raw image (b) The background removed image (c) The binary image with normalized threshold 0.05 (d) The binary image with normalized threshold 0.1. The area of (c) and (d) are 122 and 81 pixels. The threshold value obtain by Ostu's method is 0.067 which is near the value we used for all the cells (0.05).

We used a Coulter Counter to get the cell sizes in an orthogonal way. We compared the size measured from the Coulter Counter with that obtained from image segmentation in **Figure 4-15**. The mean of the calculated radius is off by ~ 1 micron. It means the accuracy of our image segmentation requires further examination. One caveat here is that the cells measured in the image and Coulter Counter are from different batches of cells, and so to be conclusive this experiment should be repeated with identical sets of cells. The cell size variation could come from the phase or the cells. Thus, the accuracy of our optical size measurement is in question.

Because the sizing error will affect the measurement of Re[CM] and n-DEP force, , this is a critical direction to improve in the future.

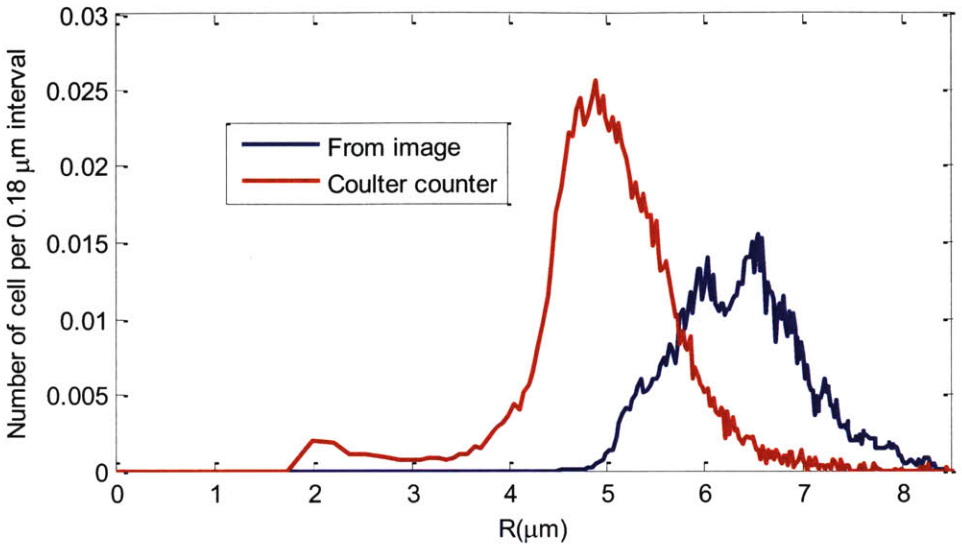

Figure 4-15 Comparison of the size measurement between the imaging segmentation and Coulter counter. The size measurement from the image is greater than the Coulter counter. (Mean 6.07 μm v.s. 5.18 μm).

4.7. Conclusion

We have created an integrated system that links the fluidic, electrical, optical subsystems to a computer, and accomplished the GUI for controlling each component. We also wrote macros for automatically sweeping different conditions. With the automated system, we can record many videos of cells in different conditions thus produce large image datasets for characterizing the both electrical and optical properties of cells. We also record each frame with elapsed time and other the parameters of the systems, which enables the study of the dynamics of the cells. Future application of velocity-based DEP force measurements or even cell rolling phenomena on the microfluidic channel can be studied in this system.

However, one shortcoming of the current system is that the resolution of the optical image is not fine enough. The resolution of the cell can affect the balance position measurement (accuracy ~ 0.5 pixel) and area measurement (accuracy ~ edge area pixel number/overall area pixel number). The accuracy can be improved with higher resolution and higher contrast of images in the future.

Chapter 5: Experimental validation

In this chapter, we will demonstrate the theory validation, the automated high-throughput measurement and the medical application of the n-DEP spring method. We first use 6 μm polystyrene beads to verify the balance position model to show that the trend of balance positions in different flow rates and voltages agree with the theory. Secondly, we measure balance positions of HL-60 cells in different frequencies and media conductivities to show that we can perform high throughput single cell DEP characterization of cells automatically. Finally, we applied this high throughput system and n-DEP spring method to a real medical application, neutrophil activation. We use balance position to distinguish between activated neutrophils and unactivated neutrophils in the right condition after screening through the different conditions in a short amount of time.

5.1. Theory validation with 6 μm polystyrene bead in low conductivity media

In our model, the balance position depends on the n-DEP field and the hydrodynamic force when other forces, such as electro-hydrodynamic force and friction force on the wall are negligible. Explicitly, as describe in chapter 3, the balance position is a function of V^2/Q [equation (3-8)]. To validate this, we measured the balance position of 6 μm polystyrene beads in different flow rates (1, 2, 4 μL/min) and with different applied voltages (3, 4, 5, 6, 7, 8, 9, 10 Volt in amplitude). We put them in the sufficiently low conductivity media (10 mS/m) to minimize the electro-thermal effect (~ 0.13 % of the DEP force, as estimated from [equation (3-14)]). The two forces acting on the cells are in the range of several pN. We first compare the consistency of the balance positions in different flow rates as a function of V^2/Q, and then we compare the measured balance position with our theoretical simulation.

5.1.1. Materials and methods

The microfluidic device

The device we used throughout the entire thesis is described in Figure 5-1, which was designed by Michael Vahey [40]. The device consists of four layers: (A) The PDMS layer (B) The glass layer with electrodes (C) The PCB board (D) The secure layer.

(A) The micro-channel layer: This layer is made of PDMS (1:10 with secure agent) and the thickness is about 5-7 mm. There is a microfluidic channel (20 μm by 2 mm by 5 cm) in this layer which made of the SU-8-silicon mold. We punched the holes on the PDMS layer and cleaned the surface with Scotch tape before plasma bounding.

(B) The glass layer with electrodes: This layer is made of the 762-μm thick pyrex wafer with a thin film of gold electrodes. We patterned this thin metal layer (200nm/10nm Au/Ti) using a conventional lift-off process (negative resist NR-7).

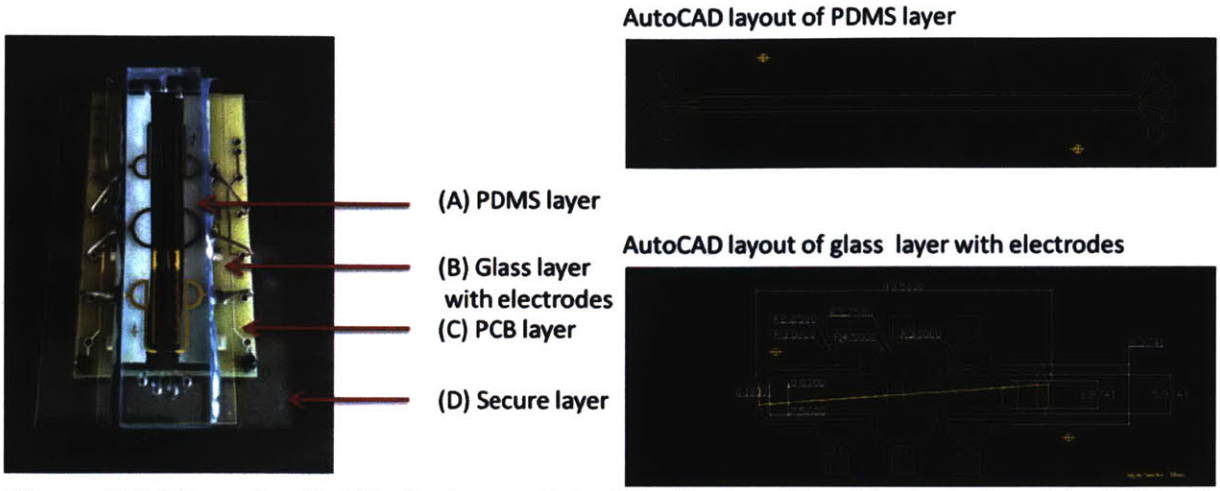

Figure 5-1 The microfluidic device used in this thesis. The chip is designed by Michael Vahey. The device consists of four layers: the PDMS layer, the glass electrodes, the PCB layers and the secure layers on the bottom. The AutoCAD layout of (A) and (B) are shown on the right.

We exposed the layer (A) and layer (B) in the oxygen plasma for 1 min to make them temporarily hydrophilic and bound the two layers together. We baked the chip on the hotplate (80°) for 30 minutes to secure the binding. After that, we sealed the side of the layer (A) and (B) with non-conductive epoxy to prevent fluid leakage.

(C) The PCB board: The PCB board is the interface between the electrodes and the alligator clips. We used conductive epoxy to connect the electrode and the printed circuit board.
(D) The secure layer: This layer is to stabilize the entire chip on the stage while the tubing and alligator clips connected to the chip.

The layer (C) and layer (D) is optional because the device has two pairs of electrodes and we are only using one pair so the PCB layer for connecting the two pairs of signal is not needed. We can directly tape the glass layer on the microscope stage for simplicity.

The fluidic system

We used two glass syringes (Hamilton Model 1001, 1 mL) to load the beads solution and buffer. Both bead solution and buffer have the same conductivity (10 mS/m). We use 6 μm (6.081 ± 0.195 μm) carboxyl-modified polystyrene beads (Polyscience) in this experiment. The benefit of using carboxyl-modified beads is that the charge group on the surface will make them repel each other to prevent particle aggregation. We set the bead concentration to ~1 million/mL so that they have enough spacing with each other (which minimizes particle-particle interaction) while deflecting by the electrodes. The conductivity of the liquid is measured using a commercialized conductivity meter (Thermo Orion pHuture™ Meter, Model 555A) at room temperature. The low conductivity media is formed by diluting 1x PBS (1.6 S/m) with DI water. The reason we

use a low conductivity media for model validation is to prevent the electro-thermal effect which will introduce extra forces. After loading the solution, it is important to remove the bubbles in the syringes to minimize the time for the flow rate to reach steady state. The glass syringes were connected to the device with 1/16 inches tubing (IDEX 1474: inner diameter 0.004 inches). The tubing is flexible enough to bend and matches with the inlets. We use a syringe pump to push the two syringes at flow rate: 0.5, 1, 2 μL/min so that the total flow rate (Q) flow through the device is 1, 2, 4 μL/min. The syringe pump and syringes were placed vertically and syringes were pointing down. There are two benefits of putting the syringes vertically. For one, the particle is usually slightly denser than the solution so as the particles sediment, the number of cells coming out of the syringe will not decrease too fast. For the other, even if bubbles are generated in the syringes, they will rise to the top of the syringe and will not go into the tubing and hence the device. There are three inlets on the PDMS layer (as shown in **Figure 5-1**) but we only need two inlets in this experiment, one for beads solution and the other for buffer. Therefore, we use dead-end tubing to seal up unused inlet.

Experiment procedure

Before the experiment, we filled the device with 7.5% BSA (Bovine Albumin Fraction V Solution, Life Technologies) in DI water for 30 minutes to prevent non-specific binding to render the surface of the microfluidic channel. Then we flushed the device with DI water. We filled the device with DI-water until droplets formed at the inlets and outlets of the device. We turned on the syringe pumps flow to 10 μL/min until small droplets came out from the tubing. We connected the tubing and the device carefully to prevent bubble generation. We stubbed the tubing into the device to about ¾ of the depth of the inlets so that there is no leakage but also no dead end high pressure. We turned down the flow rates to around 1-5 μL/min so that we could see the cells in the objectives. We adjusted to the desire flow rates and wait for 5 minutes to allow the system to stabilize. We turned on the function generator (Agilent 33250 A) with 1 MHz signal and tested different voltages. We started from 10 V in amplitude and gradually reduced the voltage by 1 V until 3 V. Note that the output resistance of the function generator is 50 Ohm, so that the display of the voltage amplitude differs if you enter different load resistance value in the function generator program. In the case of this experiment, the impedance of the device is more than 6000 Ohm (approximate from **Figure 4-8**). Therefore, the output resistance of the function generator can be neglected and we can enter infinity for the load resistance with error < 1%.

5.1.2. Results

Experimental result

We measure the balance position in for an average of 200 beads for different flow rates and voltages and we show the representative images in **Figure 5-2(a)**. **Figure 5-2(b)** shows the representative balance position distribution which is similar to a Gaussian distribution because of the mapping between the size and balance position is approximately linear in small variation and

the distribution of the size is approximately Gaussian. We summarized the measured balance position with mean and its standard deviation of the population in **Figure 5-2(c)**. As expected, the higher the flow rates, the smaller the balance position we have because we are compressing the n-DEP spring with higher applied HD drag force. For a given flow rate, if we increase the voltage, the balance position also increases because the higher n-DEP force makes the n-DEP spring stiffer. If we plot the data as a function of V^2/Q, the three lines overlap with each other [**Figure 5-2(d)**]. Thus, the balance position is a function of V^2/Q, supporting the model that the balance position is the ratio of the DEP force and the HD drag force.

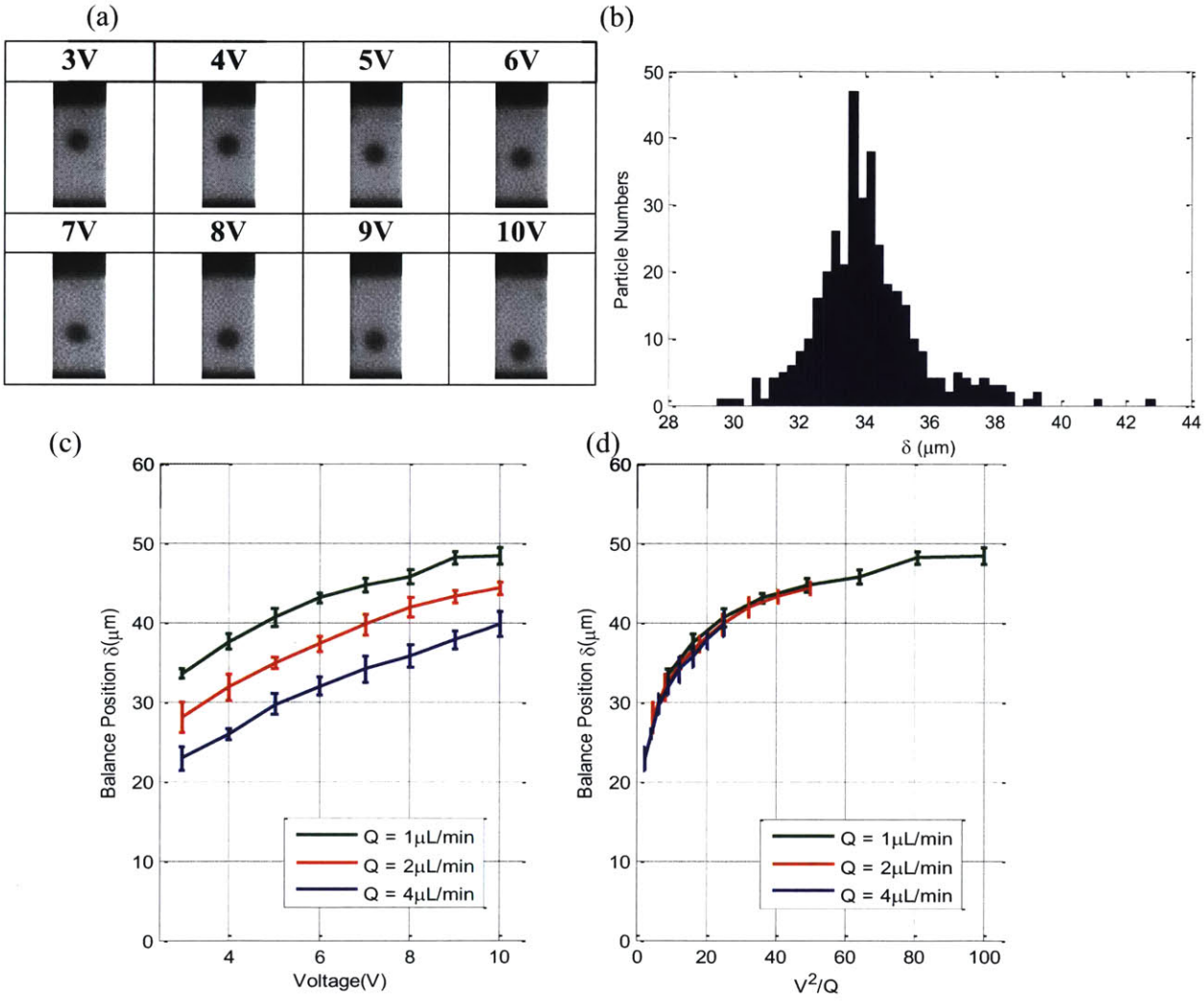

Figure 5-2 Experiment result for balance positions of 6 μm beads. (a) Representative images (median balance position) for Q=1 μL/min. The images are 20x50 μm big. (b) Representative histogram of the balance position (Q=4 μL/min and V=7 V). (c) The balance position measured from different Q and V. (d) The balance position as a function of V^2/Q.

Simulations

Using the coplanar strip electrical model [equation (3-6)], we calculated F_{DEPx} and the maximum n-DEP force in x-direction ($F_{DEPxMAX}$). For applied voltage amplitudes in the range of 3-10 V, the forces are in the range of 20.1-223 pN. On the other hand, we use the first order parabolic fluid profile model [equation (3-5)] to calculate F_{Dragx} of different flow rates (1, 2, 4 μL/min) as 1.22 pN, 2.43 pN, 4.87 pN. Therefore, the model force ratio $F_{DEPxMAX} / F_{Dragx}$ is in the range of 4 to 183. We plot the simulated result with log scale of force ratio in **Figure 5-3**. In the model, the relation between the balance position to the log force ratio is approximately linear (slope~16 μm/decade) when the balance position is greater than one channel height (17 μm in this case). The exponential decay of the field is similar to the levitation height model in DEP-FFF [39] when the balance position is away from the electrodes.

The model parameters and the modeled uncertainty are listed in **Table 5-1**. We analyze the uncertainty (possible errors) from each parameter in the model and calculate the potential errors in force ratio and in balance positions using equation (3-9). Our estimate of the balance position error is obtained from the condition of 10 V and 1 μL/min (δ=46.9 μm).

From the equation (3-9), we find out that some significant parameters that could result in the systematic error in the balance position are (1) the channel height, (2) the viscosity of the fluid, (3) the cell radius, (4) the angle between the flow and the electrodes, and (5) the normalized frequency response. The effect of (2), (4), and (5) is obvious because it directly affect the force ratio and therefore couple to the balance position by the modeled line. The effect of (3) is also foreseeable because size dependency of the force ratio is approximately R^1~R^2 from the equation (3-9). The surprising effect is that of channel height (1), where it changes the force ratio and balance position in different ways. By slightly increase the channel height, the force ratio slightly decrease because the $F_{DEPxMAX} \sim h^{-3}$ while $F_{Dragx} \sim h^{-2}$. However, for the large balance position, $F_{DEPx}(\delta)$ is not so sensitive to h so the effect of the hydrodynamic force take place.

Table 5-1 The parameter table for simulation

Symbol	*Description*	*Value*	*Obtained from*	*Error*	*Error in force ratio* $\frac{F_{DEPxMAX}}{F_{Dragx}}$	*Error in* δ *(um)*
Q	*Flow rate*	*(1,2,4)e-9/60*	*Syringe pump*	*± 0.35%*	*± 0.35%*	*~0*
w	*Channel width*	*2e-3*	*Measured from image*	*± 1%*	*± 1%*	*±0.05*
h	*Channel height*	*20-e6*	*Measured from Dektak (EML)*	*± 5%*	*∓3.4%*	*±1.6*
g	*Electrodes gap*	*16.3e-6*	*Measured from image*	*± 5%*	*∓2.85%*	*∓0.15*
d	*Electrodes width*	*46e-6*	*Measured from image*	*± 2%*	*∓0.001%*	*±0.05*
R	*Particle radius*	*3e-6*	*Polyscience beads*	*± 10%*	*± 13%*	*± 0.7*
v	*Voltage amplitude*	*(10,9,8,7,6,5,4,3)V*	*Function generator*	*±1%*	*±2%*	*±0.1*
θ	*Angle between the flow and electrodes*	*4°*	*Measured from image*	*± 10%*	*∓9%*	*∓0.6*
η	*Viscosity of the fluid*	*9.68e-4*	*Obtain from table*	*<± 10%*	*<∓9%*	*<∓0.6*
ε_m	*Media dielectric constant*	*80* ε_0 *=7.08e-10*	*Reference*[45][46]	*<± 3%*	*<±3%*	*<±0.15*
ε_p	*Particle dielectric constant*	*3.5* ε_0 *=3.10e-10*	*Reference*[45][46]	*<± 10%*	*<∓0.1%*	*~0*
σ_m	*Media conductivity*	*~10mS*	*Measured from conductivity meter*	*<± 10%*	*<±0.43%*	*~0*
σ_p	*Particle conductivity*	*0.33-0.66mS*	*Reference*[45][46]	*±50%*	*∓0.2%*	*∓0.15*
$p(f)$	*Normalized frequency response*	*1*	*Electrical model*	*<-10%*	*<-10%*	*< -0.65*

(Unit: SI unit)

Comparison between the model and experimental result

We plot the simulated result with the experimental result in **Figure 5-3**. The simulated balance positions have a similar trend but larger absolute value than the measured ones. We use least square fitting to fit the balance position by tuning the force ratio and we find out the best fitting curve has a force ratio 47 % to smaller than expected. We compare the modeled balance position and the measured balance position in two different perspectives: (1) the balance position (δ). (2) the force ratio ($F_{DEPxMAX}$ / F_{Dragx}).

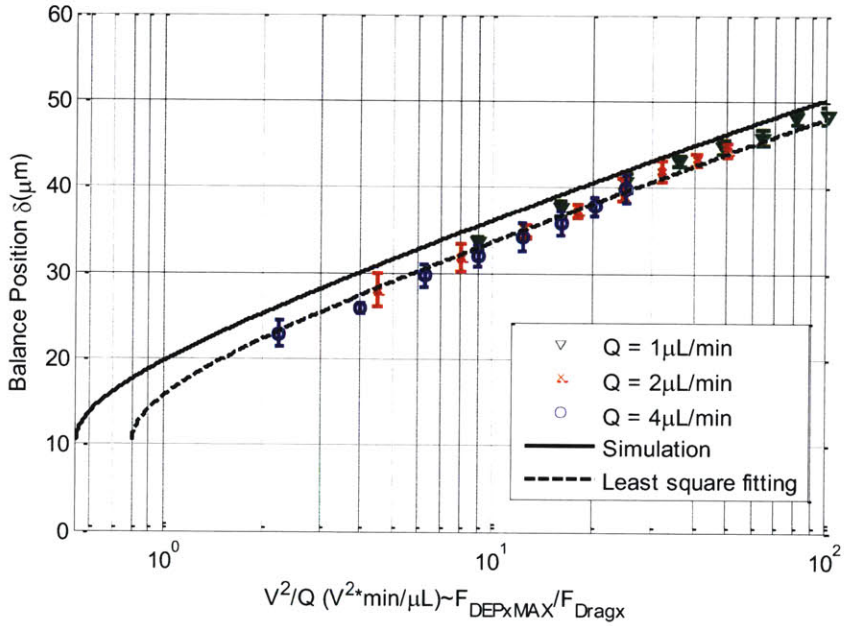

Figure 5-3 The comparison between simulation and experimental balance position with different flow rates and voltages. The least square error fitting is done with changing the value p(f) in equation (3-8) to minimize the square error of δ.

(1) Compare the balance position (δ) error

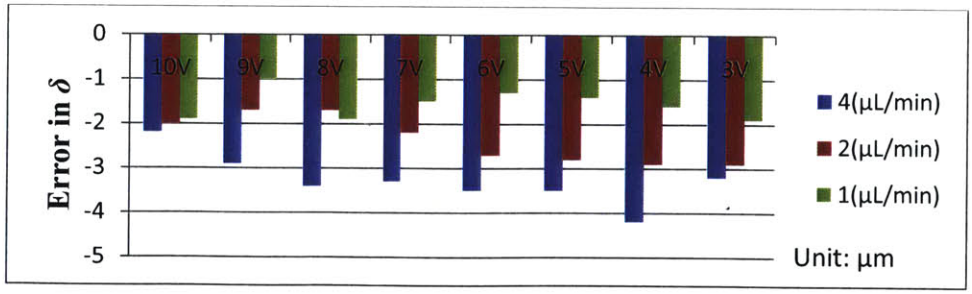

Figure 5-4 Balance position error between measurement and model. It is calculated as the [(measured δ – modeled δ] for data in **Figure 5-3**.

If we analyze the data from the balance position perspective (**Figure 5-4**), the measured balance position is smaller than the model balance position by 1 μm to 4 μm. The average error is around -2.4 μm.

(2) Compare the force ratio ($F_{DEPxMAX} / F_{Dragx}$)error

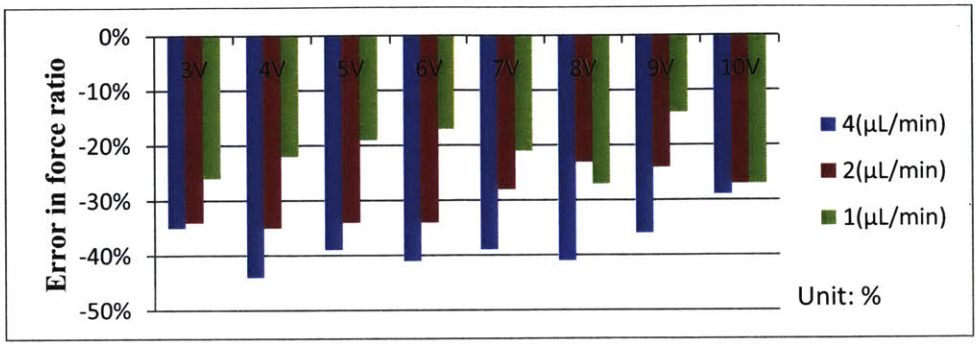

Figure 5-5 Force ratio error between measured force ratio and model force ratio. It is calculated as the [(measured – model)/model] for data in **Figure 5-3**.

If we compare the measured force ratio to the model force ratio (**Figure 5-5**), we find out that the measured force ratio is ~30 % in average smaller than the modeled one.

(3) Standard deviation of the balance position (δ)

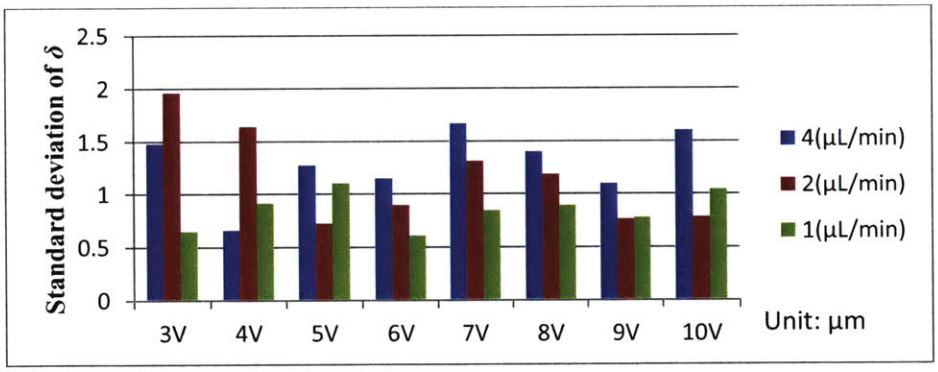

Figure 5-6 Standard deviation of the balance positions (δ) measured in different frequencies and flow rates. They are calculated for each balance position distribution.

The standard deviation of the balance position for different conditions is shown in **Figure 5-6**. The mean of the standard deviation is 1.1 μm. There is no specific trend found in the experiment. The source of the variance mainly comes from the size difference of the particles (stated as 10% CV from the manufacturer), which would result in 0.7 μm standard deviation. The rest of the variation could come from the segmentation process because our pixel size is 1.07 μm, the worst case error for the measurement of the centroid could be ~ 0.5 μm.

Discussion

We overestimate the n-DEP force or underestimate the hydrodynamic drag force in the model. The error could mainly arise from the following reasons.

(1) *p(f) is not 1:* Since we measure the voltage across the electrode and make sure it is the one we applied, the potential voltage drop could come from the electrode polarization effect [47]. This effect is related to the discontinuity in current carriers at the electrode/liquid surface, which will result in voltage drop at the electrode\electrolyte interface. Since this effect is frequency dependent, we could do more experiment in different frequencies in the future to find out the *p(f)* in the system.

(2) *The η is larger than expected:* The viscosity of the liquid we use is for the pure water but the solution is a diluted PBS which contains some ions that that could potentially makes the solution more viscous.

When we reduce the force ratio by 47 %, the maximum deviation between the average measured data and the simulation reduces to 16 % (at 9 V and 1 μL/min). The least square error fitting has a regression coefficient of 0.9996.

5.1.3. Conclusion

The balance positions of the 6 μm polystyrene beads overlap when they have the same V^2/Q. This supports our balance position model. The data are internally consistent but the absolute balance positions are smaller than predicted by ~2.4 μm. This means we overestimate the n-DEP force or we underestimate the drag force in the model. The balance position as a function of force ratio agrees with the corrected first order model with regression coefficient 0.9996 after 47 % correction. Since some of the experimental parameters of that device, such as channel height, angle between the electrodes and flow were not certain, the absolute value between the model and the experiment require more experiments to validate. Even though we have systematic error between the model and the experiment, we can use particles of known electrical properties to characterize the systematic error into a systematic parameters to calibrate the system when we are characterizing cells.

5.2. Balance position measurement for HL-60 cells in different frequencies and conductivities

We use the human leukemia HL-60 cell line as our first target for cell electrical characterization because it is a well-studied non-adherent cell line. Back in 1994, Becker *et al.* studied the DEP force for HL-60 cells and separated them from blood (Becker, Wang, Huang, Pethig, & Vykoukal, 1994). They used interdigitated electrodes in low conductivity media (10 mS/m) to attract the HL-60 cells with p-DEP force. Following by that, Huang *et al.* used DEP-FFF method to separate HL-60 cells and peripheral blood mononuclear cells [39]. Their media conductivity also was low (<56 mS/m). However, there is no well-established study of the properties of HL-60 cells in high-conductivity media. Recently, an English group [49] studied the dielectric

response in high-conductivity media (1.35 S/m). They modeled the Re[*CM*] in high-conductivity media and at high frequency and used a velocity-based method to distinguish live and dead HL-60 cells at 40 MHz. However, no quantitative data of Re[*CM*] was derived. With the n-DEP spring method, we are able to estimate the Re[*CM*] of individual cell in a quantitative and higher-throughput way. We are measuring the balance position of 5 different conductivities (0.3, 0.35, 0.53, 0.89, 1.47 S/m) and each with 8 different frequencies (0.1, 0.2, 0.4, 0.8, 1.6, 3.2, 6.4, 12.8 MHz) in an hour. We acquire ~100,000 single particle images for analysis. We first compare the experimental result and the single shell model (**Figure 5-7**) based on the electrical parameters extract from the low conductivity media [39].

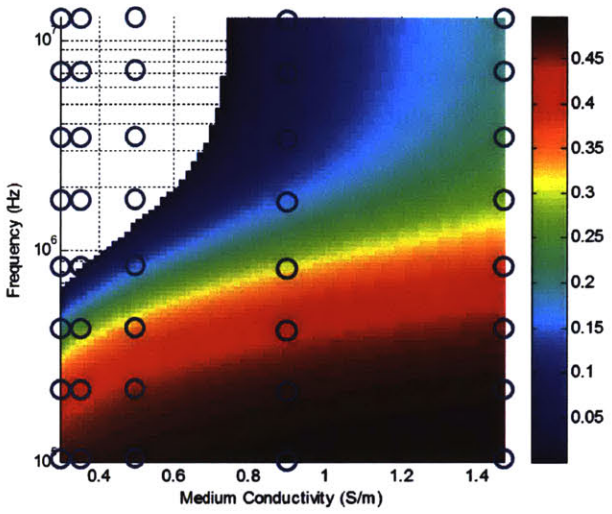

Figure 5-7 The |Re[CM]| (only negative part) for HL-60 Cells. The dots are conditions of the measurement.

5.2.1. Materials and methods

Determine the scanning scheme

We proposed two schemes to measure the n-DEP force in different frequencies and conductivity. Scheme 1: We set up a fixed spatial conductivity gradient like in Iso-Dielectric Separation. By imaging different parts of the electrodes, we can obtain the balance positions in different conductivities. Scheme 2: We measure the balance positions in flat conductivity but temporally change the conductivity after scanning in a set of frequencies for one media conductivity.

For scheme 1, the challenge is in refocusing after changing the viewing position and the errors from channel condition differences between different parts of the channel. Furthermore, the spatial conductivity gradient could result in an imposed-gradient electro-hydrodynamic flow which would distort the balance position to force ratio mapping.

For scheme 2, we need some intervals between the measurements of different conductivity for stabilizing the conductivity. Also, the impedance of the electrodes changes with the media

conductivity in the channel. Therefore, we need to use complementary methods to compensate for the error of the voltage drop.

We decided to use scheme 2 for HL-60 characterization because we have better control of the conductivity we are using.

Electro-thermal effect

From the equation (3-14), we estimate the DEP force to electro-thermal effect ratio which is about 22 % at the smallest balance position.

Relative measurement with beads

The absolute force ratio depends on voltage drops, device variation, flow rate errors, and model inaccuracy. Therefore, we use 6 μm (6.081 ± 0.195 μm) and 10 μm (10.269 ± 0.502 μm) polystyrene beads for error calibration. In the model, the Re[*CM*] of the 6 μm and 10 μm polystyrene beads is always approximately -0.5 in the media conductivity and frequency range we are interested for measuring the electrical properties of HL-60 (**Figure 5-8**). Therefore, we can compare the relative force ratio between the HL-60 cells and 6 μm and 10 μm polystyrene beads.

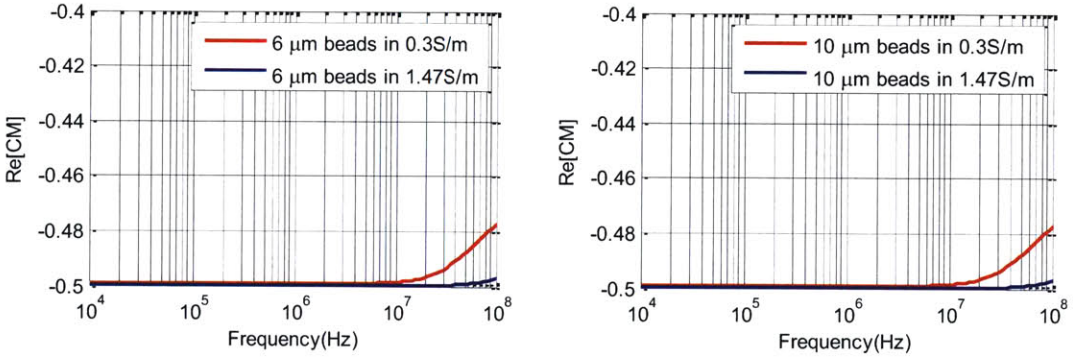

Figure 5-8 The Re[CM] for 6 μm and 10 μm polystyrene beads. In the region of our experiments, the Re[CM] are mostly -0.5. In 12.8MHz, the Re[CM] for both beads raise a little to -0.498, which we still assume to be -0.5.

Experimental setup

The microfluidic device is fabricated as the same as in section 5.10 but with the channel dimension of 17 μm by 2 mm (*h* x *w*). We control the media conductivity by adjusting the flow rates of two syringe pumps. The syringe pump A has two syringes of high conductivity media (1.6 S/m) while the syringe pump B has two syringes of lower conductivity media (0.17 S/m). There is one cell syringe and one buffer syringe in each syringe pump. We mix the low conductivity and high conductivity streams with flow rate ratio of 1:10, 1:3, 1:1, 3:1, 10:1 while the overall flow rate is 4.4 μL/min in total. In the end, we get two streams (cell/buffer) of equal

flow rates (2.2 μL/min) and equal conductivity (0.3, 0.35 0.53 0.89 1.47 S/m) connecting to the inlets of the device. The mixing was done in the tubing using two Y-shape connectors. The length of the tubing after the mixing is 35 cm for premixing before they go in to the chip. The camera took pictures at 8 frame/s, while we set the camera delay as 50 ms and exposure time as 1 ms. The velocity of the cells is around 2 mm per second so their images can be taken ~5 time each as the cells pass through the field of view.

Sample preparation

The HL-60 cell lines for this experiment were cultured in the media (DMEM / 20 % FBS / 1 x Penstrip) in T75 flask. We measured the HL-60 cells 24 hours after seeding (passage #10). We centrifuged the cells down and resuspended them into isotonic high-conductivity media (1 x PBS / 0.75 % BSA / 1 mM EDTA) and low conductivity media (8.5 % Sucrose / 0.3 % Dextrose / 0.75 % BSA). The conductivity of the liquid is measured from commercial conductivity meter (Thermo Orion pHuture™ Meter, Model 555A) at room temperature.

Experimental procedure

Before the experiment we filled the device with 7.5 % BSA for 30 minutes to prevent non - specific binding. We loaded syringes with cells and buffers carefully without making any bubbles in the syringes. We connected the high conductively buffer and low conductivity buffer carefully through the Y connectors and squeeze out the air inside all tubing with high flow rates (30 μL/min). We connected the cell stream and buffer stream of the same flow rates to the device. We observe the electrodes at the buffer side (~1/3 of the channel) so that we only record the stable deflected cell but not the cells coming into the electrodes.

We connected the electrodes function generator with the electrodes then start the automated system for different frequency scan. We scan the frequencies from low to high (0.1 – 12.8 MHz). In high conductivity media and low frequency, it is easy to burn the electrodes by electrolysis. This would ruin the electrodes irreversibly. Therefore, we avoid measuring the low frequencies in high conductivity media. We recorded the video of each condition for 300 frames. The cell and bead concentration are both around 1 million/mL.

Image processing

We extract out the particle images from 39 movies of different conditions. In each condition, we have about 3000 particle images. Since the particle images are a mixture of the 6 μm beads, 10 μm beads, and the HL-60 cells, we need to classify them. For each particle image, we extract out the balance position, the area, and the mean intensity of the particle. We use the intensity information and area information to classify the three categories. The beads are darker than the cells, and 10 μm beads are larger than 6 μm beads. We tuned the threshold of intensity and area by visually classifying the images. There is a slightly brightness difference between different location in the field of interest. Therefore, we did a compensation of optical gain (normalizing

the intensity of the particle image) before extracting the parameters. The images therefore coming from the mixture and classified as individual clusters (**Figure 5-9**). We manually count 1000 images for each classified category and find that the accuracy of each is 99.9 % (6 μm beads), 96.9 % (10 μm beads), and 92.6 % (cells). In detail, there are 1 cell image in 6 μm bead category, 22 cell images and 9 (cell+6 μm bead) images in 10 μm bead category, and 34 small bead images and 40 big bead images in cell category.

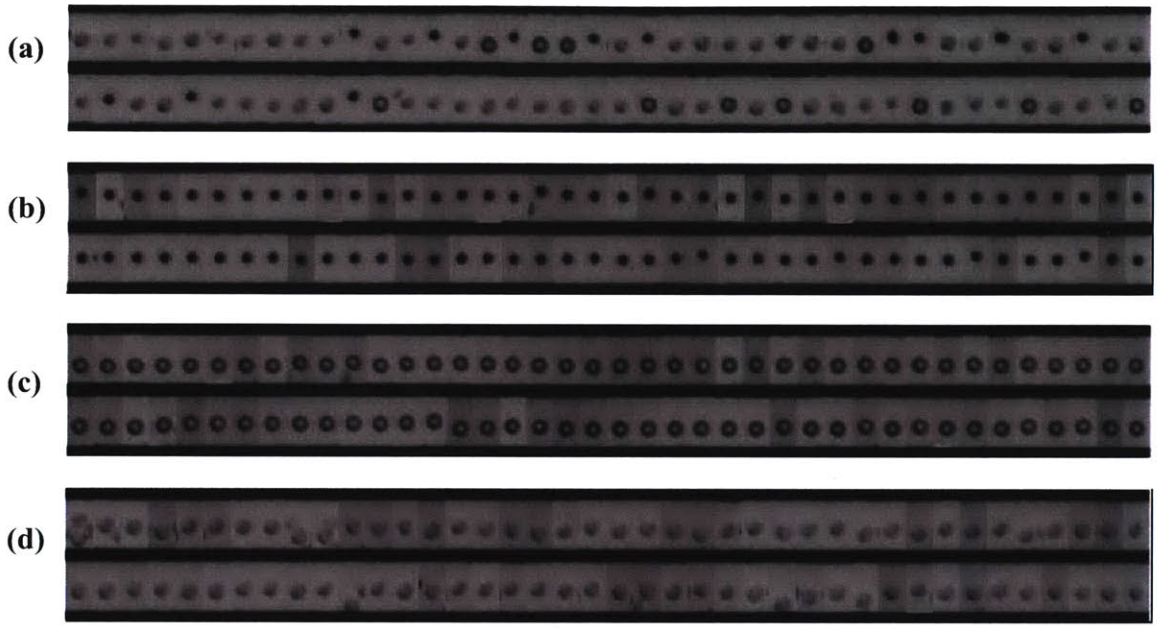

Figure 5-9 Particle images of (a) a mixture (b) 6 μm beads, (c) 10 μm beads, and (c) the HL-60 cells. Each image is 21x50 pixels (1 pixel = 1.07 μm). Images are acquired at 0.3 S/m and 0.4 MHz.

5.2.2. Results

We select two datasets to present the balance position histograms at different frequencies (**Figure 5-11**) and different conductivities (**Figure 5-12**). The mean of the HL-60 cells diameter is 10.34 μm (measured from Coulter Counter Z2). The 6 μm beads and 10 μm beads are references to calibrate out systematic errors.

From equation (3-7) we can explicit express Re[*CM*] as

$$\mathrm{Re}[CM] = [\frac{18Q\eta \sin\theta}{V_{RMS}{}^2 wh^3 \varepsilon_m p(f)}][\frac{h-R}{Rq_R(\delta)}] = C_1[\frac{h-R}{Rq_R(\delta)}] \qquad (5\text{-}1)$$

where the first term is the systematic parameter

$$C_1 = \frac{18Q\eta \sin\theta}{V_{RMS}{}^2 wh^3 \varepsilon_m p(f)} \tag{5-2}$$

shared commonly with the beads and cells, and the second term is different for different particles. We first use Re[CM] = -0.5 and the balance position of beads to quantify C_1 in each condition. Then we use the C_1 to calculate the Re[CM] for the cells.

(1) The systematic parameter C_1 of the in different frequencies and conductivities

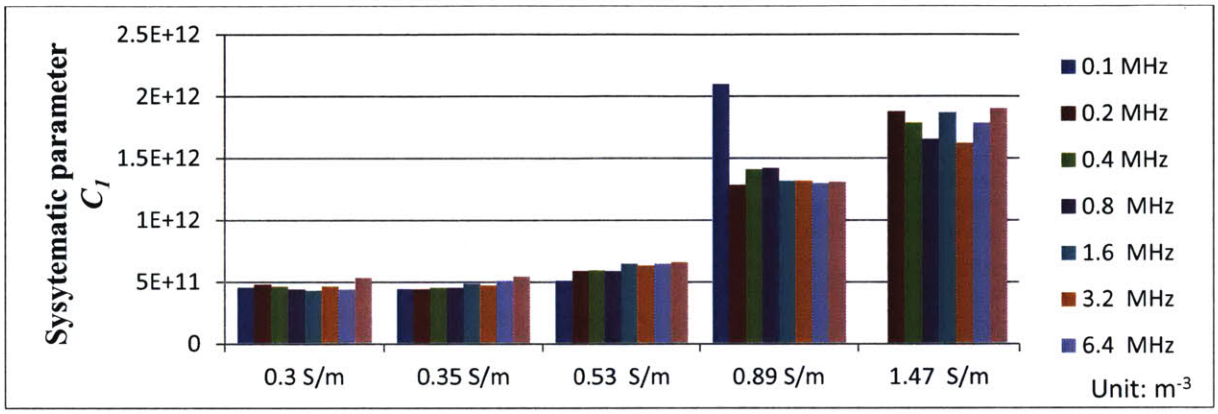

Figure 5-10 The systematic parameter C_1 for different frequencies and media conductivities using 6 μm bead as reference.

We calculated the C_1 from the 6 μm beads from equation (5-2) and the balance position measurement of 6 μm beads in **Figure 5-10** . It is a function of conductivity but not very clearly dependent on frequency. The C_1 increases with conductivity because the output resistance of the function generator is 50 Ohm and the resistance of the device is (70, 127, 357 Ohm) at (0.3 0.8 1.6 S/m) at 1MHz from the impedance measurement (**Figure 4-8**). Therefore, the gain of the frequency response $p(f)$ reduce to about half of the original in high conductivity.

(2) Re[CM] Measurement in different frequencies

We compare the balance position histogram in different frequencies in **Figure 5-11** (0.3 S/m). The mean balance positions of the two kinds of beads varied from 27.4-28.6 μm and 33.3-34.6 μm (~2 % error) across frequencies from 0.1 MHz to 12.8 MHz. At 0.1 MHz, the cell has the balance position similar to the 10 μm beads. Since the cell has similar size (R=5.2 μm in average from the coulter counter) with the 10 μm beads, this implies that the Re[CM] for the cells should be close to -0.5 at this frequency and conductivity, which make sense with the modeled Re[CM] = -0.47. The balance positions for the cells decrease when the frequency increases. In our experiments, the cell numbers reduced dramatically from 0.4MHz to 0.8 MHz which can be explained by the model. In this conductivity, the cross over frequency is 0.7 MHz (**Figure 5-7**). Therefore, many cells no longer experience n-DEP at 0.8 MHz. At 12.8 MHz, most cells do not experience n-DEP so there are few cells deflected by the electrodes.

Frequency: 0.1 MHz **Model Re[CM]: -0.47** **Exp Re[CM]: -0.50**	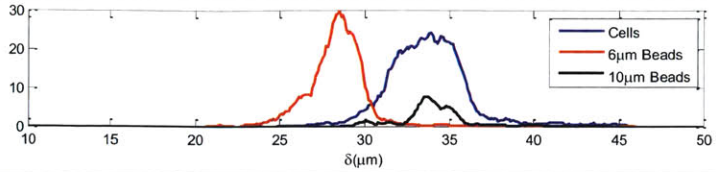
Frequency: 0.2 MHz **Model Re[CM]: -0.41** **Exp Re[CM]: -0.42**	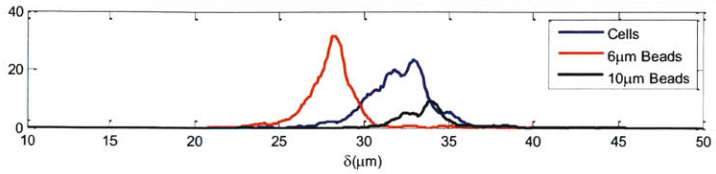
Frequency: 0.4 MHz **Model Re[CM]: -0.23** **Exp Re[CM]: -0.30**	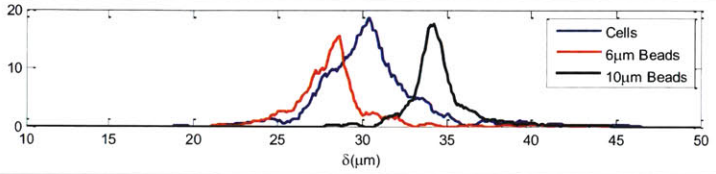
Frequency: 0.8 MHz **Model Re[CM]: p-DEP** **Exp Re[CM]: -0.24**	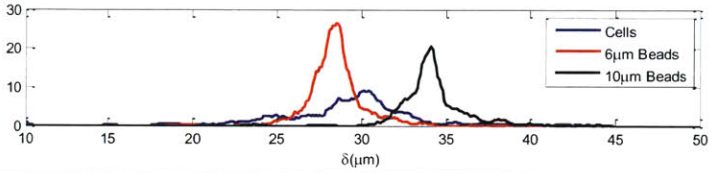
Frequency: 1.6 MHz **Model Re[CM]: p-DEP** **Exp Re[CM]: -0.20**	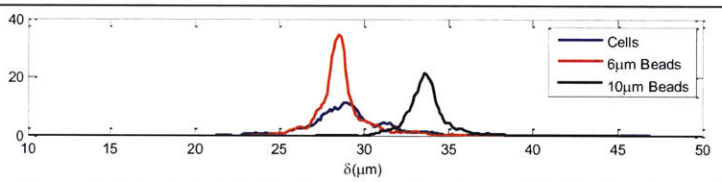
Frequency: 3.2 MHz **Model Re[CM]: p-DEP** **Exp Re[CM]: -0.18**	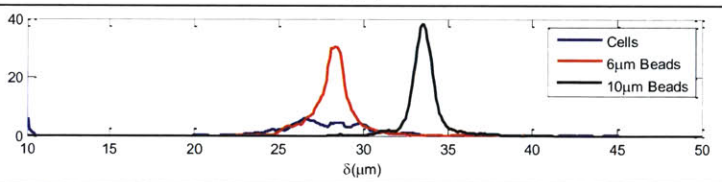
Frequency: 6.4 MHz **Model Re[CM]: p-DEP** **Exp Re[CM]: -0.16**	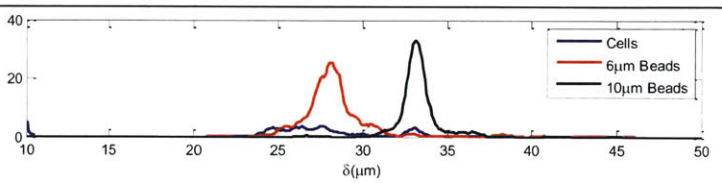
Frequency: 12.8 MHz **Model Re[CM]: p-DEP** **Exp Re[CM]: -0.18**	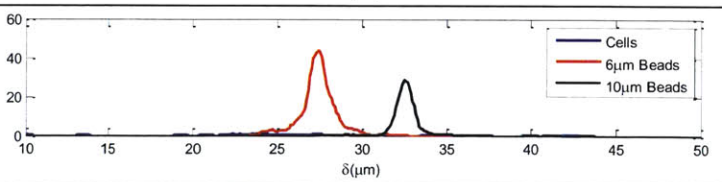

Figure 5-11 The balance position histograms of the HL-60 cells, 6 μm beads, 10 μm beads in 0.3 S/m and different frequencies. The model (from the literature [39]) and experimental Re[*CM*] (calculated from equation (5-1) with 6 μm beads as reference) of the HL -60 cells is compared on the left. The y-axis unit is (cells/μm interval).

(3) Measurement in different media conductivities

We compare the balance position histogram in different conductivities in **Figure 5-12** (0.4 MHz). The balance positions of the beads decrease when the conductivity increases because the actual voltage drop in the liquid is reduced when the impedance of the liquid decreases. The balance position of the cells at 0.30 S/m is between the 6 μm beads and 10 μm beads. At high conductivities (0.89 S/m 1.47S/m), the balance positions of the cells are similar to 10 μm beads.

Conductivity: 0.30 S/m **Model Re[CM]: -0.23** **Exp Re[CM]: -0.30**	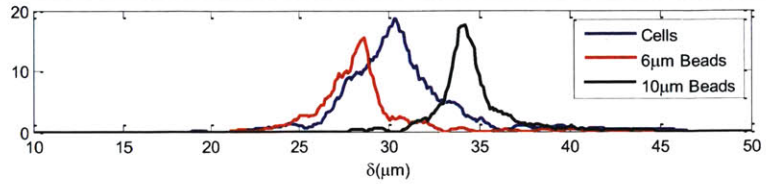
Conductivity: 0.35 S/m **Model Re[CM]: -0.28** **Exp Re[CM]: -0.28**	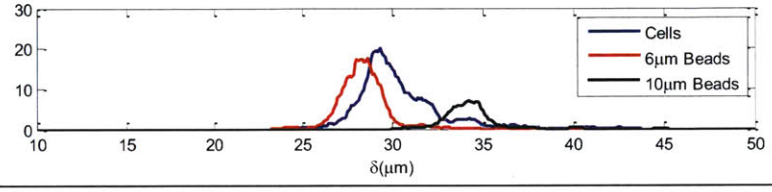
Conductivity: 0.53 S/m **Model Re[CM]: -0.36** **Exp Re[CM]: -0.31**	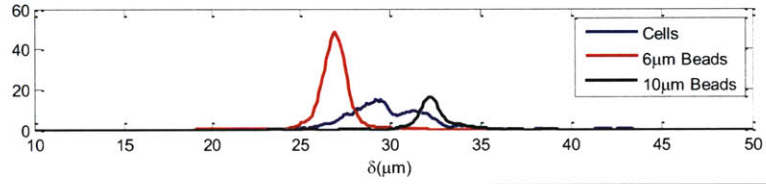
Conductivity: 0.89 S/m **Model Re[CM]: -0.43** **Exp Re[CM]: -0.44**	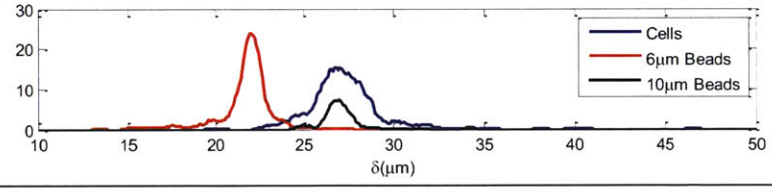
Conductivity: 1.47 S/m **Model Re[CM]: -0.46** **Exp Re[CM]: -0.40**	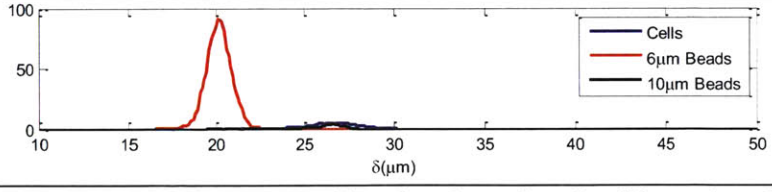

Figure 5-12 The balance position histograms of the HL-60 cells, 6 μm beads, 10 μm beads in 0.4MHz and different media conductivities. The model (from the literature [39]) and experimental Re[*CM*] (calculated from equation (5-1) with 6 μm beads as reference) of the HL - 60 cells is compared on the left. The y-axis unit is (cells/μm interval).

We also find that the standard deviation of the beads' balance positions are larger in the existence of the mixture (6.4 % versus 3.9% for unmixed beads), likely because the velocities of the cells and beads vary so that there can be collisions in the channel. These collisions would disturb the balance position. We can reduce this effect by diluting the particles.

(4) Calculated Re[*CM*] distribution in different frequencies and conductivities

We calculated the Re[*CM*] for each cell using equation (5-1) where the C_1 is measured from the 6 μm beads and plotted the Re[*CM*] histograms in **Figure 5-13**. The histograms shift to the right as the frequencies increase, which agrees with the trend of the theoretical model (the red dots). In low frequencies and low conductivity, the measured distributions agree with the simulated model. In high conductivity, the measured distributions also agree with the simulated model. However, in the region of p-DEP or small n-DEP (Re[*CM*] > -0.2), the distributions do not match with the model which could be because we can only record the balance positions of the cells that deflected by the electrodes. Therefore, the result is biased to the cells that have stronger n-DEP forces.

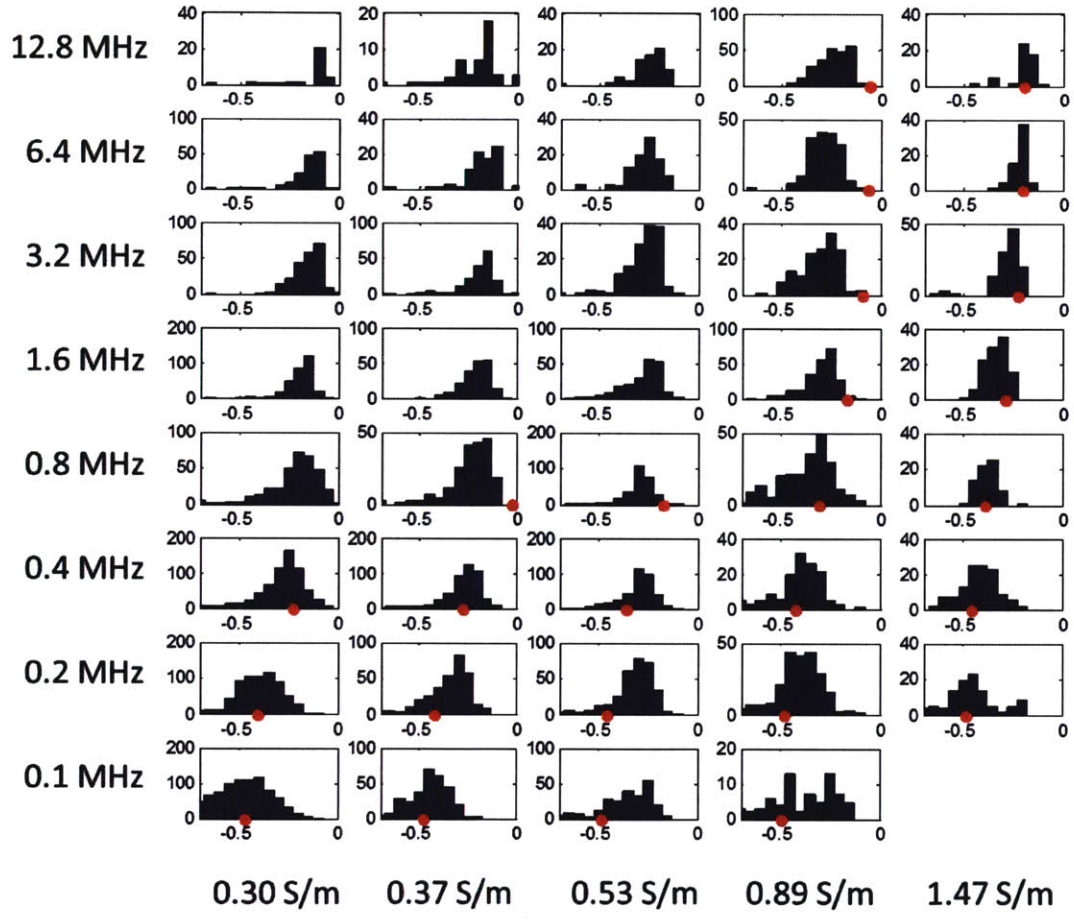

Figure 5-13 The calculated Re[*CM*] histograms in different frequencies and conductivities. The x-axis is the Re[CM] and the y-axis is the number of cell images per 0.05 interval. The red dot is the model Re[*CM*] from [39].

We plot the mean and standard deviation of the distributions in **Figure 5-14**. Again, the trend is following the model prediction. In the region where Re[*CM*] <-0.2, the experimental result matches with the model. However, with Re[*CM*] <-0.2 the calculated Re[*CM*] value deviates from the model.

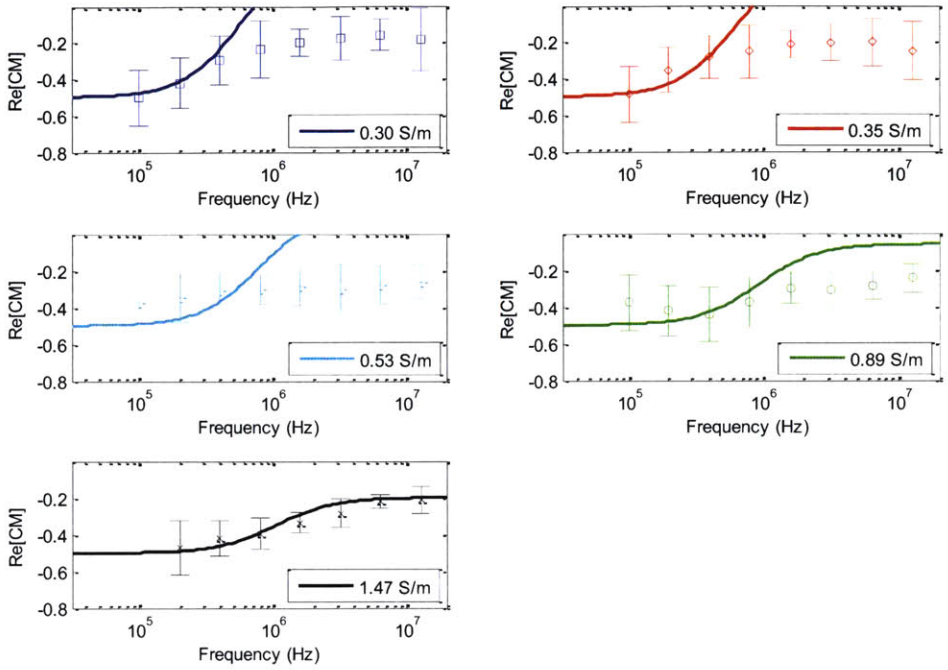

Figure 5-14 The comparison between model Re[*CM*] and the experimental Re[CM] in different conductivity. The solid lie is the model and the discrete data are the mean and standard deviation of the calculated Re[*CM*] distribution in **Figure 5-13**.

The variance of the Re[*CM*] distribution could come from (1) the cell intrinsic Re[*CM*] variation (2) the error from the size measurement inaccuracy (3) the error from the balance position inaccuracy.

Since the distribution shows some value which is not in the range of -0.5 to 0, we suspect the variation might come not only from the cell intrinsic variation but also from the error of the size and balance position measurement. Ideally, at lower frequencies or higher conductivity where the Re[*CM*] is almost -0.5 for each cell, the balance positions should reflect the intrinsic size variation. When we extract out the Re[*CM*] from size, the value should be roughly -0.5. When the conditions vary away from the Re[*CM*] ~ -0.5 region, the variation of the cell electrical properties will come in. In the region where model Re[*CM*]~ 0.5, we did not observe a narrow distribution of the Re[*CM*] in this dataset. We suspect that the measurements (size or balance position) were not accurate enough so that the variation we saw is due to these inaccuracies.

The sensitivity of the Re[CM] to the size is the same as force ratio because the size dependent factors in equation (3-9) and equation (5-1) are the same. From **Table 5-1**, the sensitivity of the force ratio (and therefore to the Re[CM]) to the size is quite high. 10% of sizing error can propagate into 13% of Re[CM] error. In our measurement, the variation of the size measurement depends on the threshold process which can result in 20 % discrepancy in area. Therefore, future experiment of higher resolution size measurement should be done in order to reduce the error coming from the size measurement.

One thing we did not consider in the model is the electro-thermal effect which is ~23% around a balance position of 10 μm. Ideally, we should perform more experiments to calibrate this additional force in high conductivity as a function of frequencies and position using equation (3-13) However, with the relative measurement of beads, the effect from the electro-thermal effect seems not significant in the relative measurement of balance positions.

5.2.3. Conclusion

We successfully detect the electrical differences of the HL-60 cells at different conductivities and frequencies via their balance positions. From this experiment, we can estimate the Re[CM] in higher conductivities where cross-over frequency characterization cannot. We consider the n-DEP spring as a complementary method of cross-over frequency measurement. We can also combine the n-DEP spring method with the cross-over frequency methods (e.g., IDS) to complete the cell characterize of the 2-D Re[CM] map.

In the balance position experiments, the information we measured is biased toward larger |Re[CM]| because the cells near the cross-over frequency regions or p-DEP passed through the electrodes and we did not quantify them. For future improvement, we can lower the flow rate to measure these low n-DEP force conditions. Also we can quantify the cells that pass through the electrodes to adjust statistics for the biased result. For example, we can image both the deflected cells and pass-through cell in the same field of view if we use hydrodynamic focusing to concentrate the cells into a smaller stream line before they enter the electrodes.

In sum, even though with limited accuracy, we demonstrate the first high-throughput n-DEP characterization for HL-60 cells in different frequencies and conductivities (including high conductivity media). The system can further accumulate more datasets for different cell types to achieve a DEP library of cells (with images). They can be further used for DEP separation or electrical studies of cells.

5.3. Discrimination of activated and unactivated neutrophils

Neutrophils play an important role in the immunopathogenesis of sepsis [50]. Dielectrophoretic separation of activated neutrophils from blood provides a possibility for treatment of sepsis. Finding the separation condition of activated neutrophils and unactivated neutrophils is difficult because neutrophils can easily get activated through centrifugation or exposure to non-physiological media. Thus, sample preparation and experiment time need to be minimized.

Therefore, we use the n-DEP spring method with the automated system to test different separation conditions. We successfully find out the separation condition of unactivated neutrophils from activated neutrophils at 6.4 MHz and 0.34 S/m. The total time spent for the experiment is within 2 hours.

5.3.1. Materials and methods

Experimental setup

Similar to HL-60 characterization, we add in the 6 μm and 10 μm polystyrene beads as reference. We set up a fixed spatial conductivity gradient like in Iso-Dielectric Separation (**Figure 5-15**). By imaging different part of the electrodes, we obtained the balance positions of neutrophils in different conductivities (0.34 S/m, 0.89 S/m, 1.36 S/m).

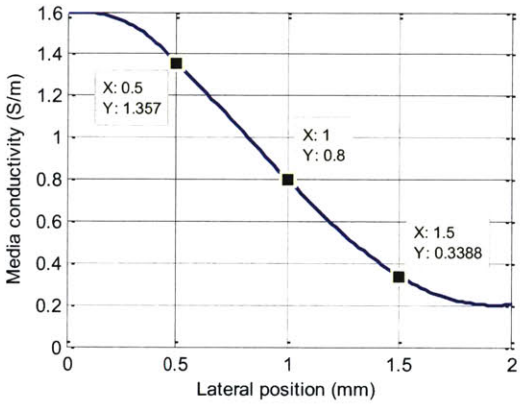

Figure 5-15 Simulated conductivity profile along the electrodes of Q = 1.5 μL/min . The simulated method is done by analytically solving the diffusion convection model in a 2D-microfluidic channel [51]. The diffusion coefficient for the ions is assumed to be 1.5e-9 m^2/s.

Sample preparation

The blood cells were obtained from healthy human donors (Blood Research Components) and arrived in the morning of each experiment day. The neutrophils were collected from the second layers (Fraction 2) of the centrifuged blood separated by gradient density methods. Then, half of them were activated by 1 μM PMA for 20mins incubation time. The activated cells and unactivated cells were centrifuged down at low speed (2500 rpm for 5 mins) and resuspended in the high-conductivity media (1xPBS/0.75 %BSA/1 mM EDTA). The low-conductivity media (8.5 % Sucrose/0.3 % Dextrose/0.75 % BSA) and middle-conductivity media buffer (1:1 ratio of high and low conductivity media buffer) were used to create the spatial conductivity gradient. The conductivity of the liquid is measured with a commercial conductivity meter (Thermo Orion pHuture™ Meter, Model 555A) at room temperature.

Experimental procedure

We measured the balance positions of the unactivated neutrophils first and then the activated neutrophils to minimize any artifacts due to activation during the experiments. The two categories of cells were loaded with different syringes. The activated neutrophils were sticky so we raised the flow rates for flushing between the measurement in different positions (different conductivities). The flow rate we use for this experiment is 0.5 μL/min for each syringe so the total flow rate in the channel is 1.5 μL/min.

Image processing

We extract out the particle images from 21 movies of different conditions. For each particle image, we extract out the balance position, the area, and the mean intensity (**Figure 5-16**). With the gradient density separation method, the neutrophils were not 100% isolated but mixed with some erythrocytes. The cells were also mixed with 6 μm and 10 μm polystyrene beads as well, and using a single dimension of information is not enough to distinguish them. We use intensity to distinguish beads and cells. We use area to distinguish 6 μm and 10 μm polystyrene beads. We manually count 1000 images for each classified category and find that the accuracy of each is 99.8 % (6 μm beads), 93.8 % (10 μm beads), and 97.3 % (cells). In details, there are 2 cell images in 6 μm bead category, 48 cell images and 2 (cell+6 μm bead) images in 10 μm bead category, and 14 small bead images and 13 big bead images in cell category.

By looking at the cluster of cells, the erythrocytes and neutrophils show differences in balance position and area scatter plot but overlap in the intensity and area scatter plot. Therefore, we set up non-binary threshold (polygon gating) in the balance position and area scatter plot to classify the cells. Since this classification of erythrocytes and neutrophils we defined is based on the electrical properties (the balance position), we did not verify the classification result by images.

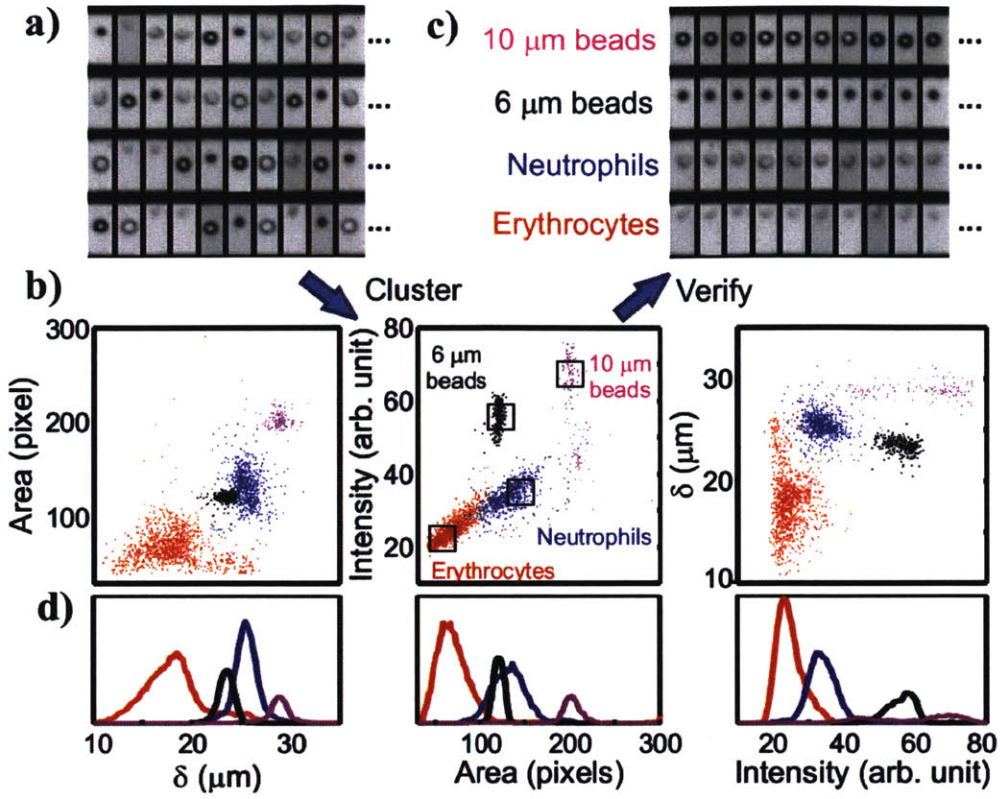

Figure 5-16 Classify the mixture through 3-dimensional clustering. (a) Images of a mixture of of 10 μm beads, 6 μm beads, neutrophils and erythrocytes. (b) Scatter plots of balance position, particle area, and intensity extracted from the images. (c) The classified populations can be verified by gating and examining the images of particles in each gated region. (d) Single-parameter histograms show overlap of the four populations.

5.3.2. Results

After gathering the balance positions of unactivated neutrophils and activated neutrophils at 7 different frequencies (0.2, 0.4, 0.8, 1.6, 3.2, 6.4, 12.8 MHz) and three conductivities (0.34 S/m, 0.89 S/m, 1.36 S/m), we plot the balance positions of the cells in **Figure 5-17**. In high conductivity (1.36 S/m), both cells have similar balance positions in all frequencies. In middle conductivity (0.89 S/m), when the frequency goes up, the balance positions of the activated neutrophils decrease faster than the unactivated ones. In low conductivity region, the cell number decreases when the frequency goes up because they pass through the electrodes in higher conductivity region. From this scanning of 7 frequencies and three conductivities, we conclude that it is better to separate the activated and unactivated neutrophils at higher frequencies and middle conductivity because the magnitude of the Re[*CM*] appears to be smaller in (12.8 Mhz, 0.89 S/m) and (6.4 Mhz, 0.89 S/m).

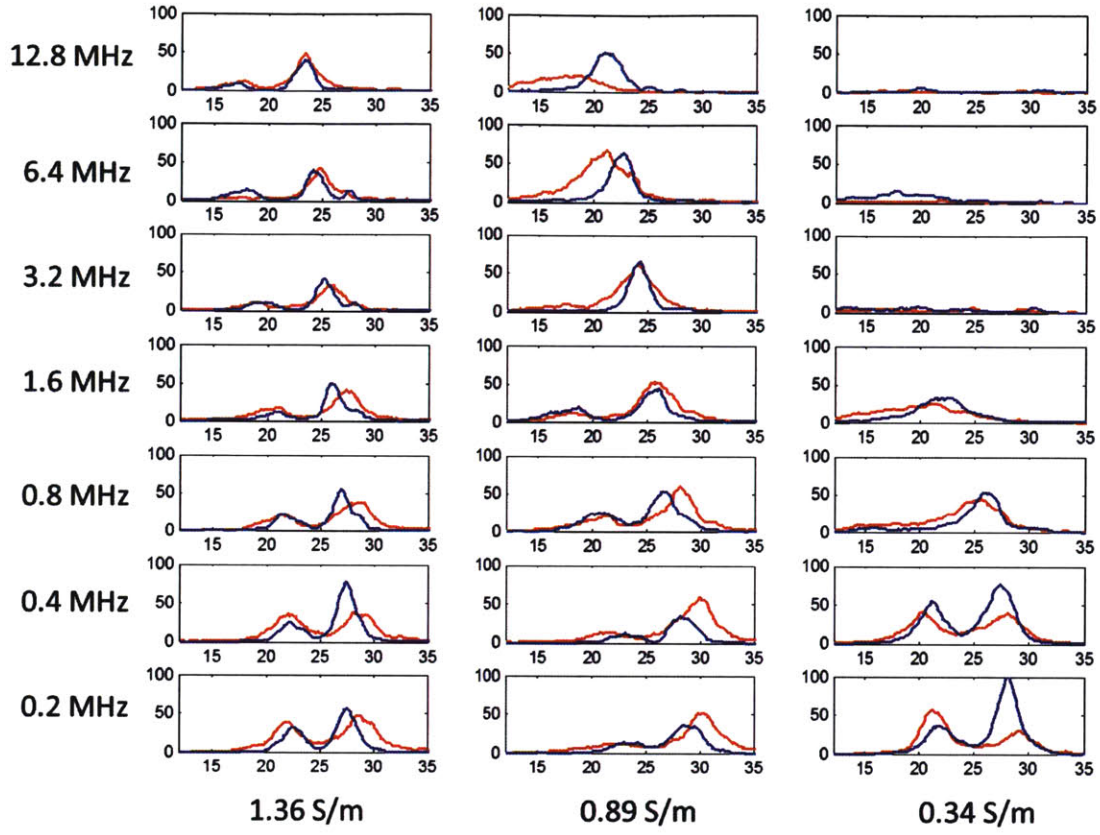

Figure 5-17 The balance position histograms of activated an unactivated neutrophils in different frequencies and conductivities. The x-axis is the balance position (μm). The y-axis is the number of particle images recorded per 0.1 μm. The red population is the activated neutrophils and the blue population is the unactivated neutrophils. Both of them have two peaks in low frequencies because the existence of the erythrocytes. In high conductivity, the two populations are similar. In middle conductivity, the two populations become different when the frequency goes higher. In low conductivity, the number of cells decreases when the frequency goes higher.

The cells pass through the electrodes in low conductivity (12.8 Mhz, 0.34 S/m), but this does not mean they do not experience a n-DEP force. Rather, it may be because the flow rate is large so that the maximum n-DEP force is not enough to deflect the cells. We repeat the experiment in another day using a new sample and examine the separability in at 6.4 MHz and low conductivity with half the flow rate (0.75 μL/min in total) (**Figure 5-18**). The low conductivity increases to 0.42 S/m in the simulation because the conductivity gradient smooth out more in slower flow rate. It shows that the two cell types have the balance position in this situation.

The activated neutrophils have smaller balance positions (17.3 μm vs. 22.4 μm) than the unactivated neutrophils [**Figure 5-18(a)**]. In this dataset, there are 2084 unactivated neutrophils and 896 activated neutrophils in each experiment. We use the receiver operating characteristic curve (ROC) to quantify how separable they are [**Figure 5-18(b)**]. The ROC curve is a standard approach for compainge classification result by defining different thresholds of the binary classification. In our case, we assume the positive hypothesis is the unactivated neutrophils because we want to recover them. We define the cells into four categories: true positive (collected unactivated cells), false negative (not collected unactiavted cells), false positive (collected activated cells), and true negative (not collected activated cells). To understand the ROC curve, we need to read the true positive rate (true positive/[true positive+false negative], also known sensitivity) and false positive rate (false positive/[false positive+true negative], as 1-specificity). For example, if we want to our collected (higher balance positions) unactivated neutrophils have purity of 90% (true positive rate = 90%), then we can only rule out 74% of the activated neutrophils (false positive rate = 26%). We compare the area-under-curve (AUC) for two ROCs and find out the balance position δ can better distinguish neutrophil activation than size.

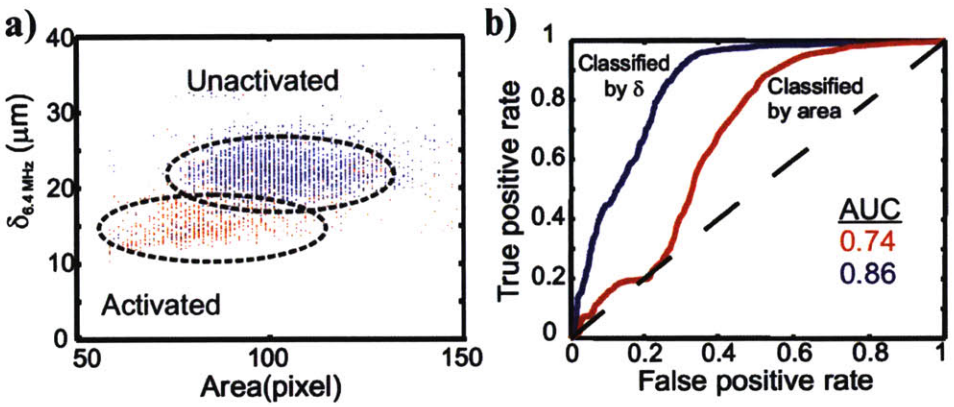

Figure 5-18 Discrimination of neutrophil activation. (a) Unactivated and activated (via PMA) human neutrophils were analyzed with balance position method. Shown are scatter plots of two intrinsic properties of the two populations. **(b)** The higher area-under-curve(AUC) obtained with electrical properties (via δ) indicates that they are better than size for distinguishing neutrophil activation.

The difference is not due to the contact force between the neutrophils and the wall because the activated neutrophils are stickier than unactivated and activated neutrophils would have larger balance positions if friction force at the wall dominated. We also observe a small size difference between activated neutrophils and unactivated neutrophils. However, after comparing the AUC of using the size as criteria and balance position as criteria, we suspect that size difference between activated neutrophils and unactivated neutrophils is not as significant as the balance position.

5.3.3. Conclusion

We use the automated system to screen out the electrical difference for neutrophil activation in different frequencies and conductivities. The fact that the balance positions are similar in low frequency but different in high frequency indicates that there are intrinsic electrical changes under PMA neutrophil activation might due to the cytoplasmic differences rather than the membrane capacitance changes. This result can assist in understanding neutrophil activation and designing devices for DEP separation of activated and unactivated neutrophils.

Chapter 6: Conclusions and future direction

In this chapter, we will summarize the work of this thesis and propose potential application and future direction for this technology.

6.1. Conclusions and contributions

6.1.1. n-DEP Spring

This thesis has described a novel method to measure the n-DEP force acting on the cells, which we call the n-DEP spring. We turned the binary result (passing or deflected) of the angle coplanar electrodes into an analog quantifiable measurement, the balance position. We have modeled and verified this method with beads and cells.

There are, however, some uncertainties within this method. Firstly, to derive the Re[CM] from balance position requires measurements of the size of the particles. Inaccuracy of the size will lead to uncertainties in the Re[CM]. There is no easy existing method for accurately measuring the size information of the cells. Especially if we want to automate this process, finding the threshold value for measuring the edge of the cell is not easy. Fortunately, in the approximation model (considering the balance position to force ratio mapping is independent of size), the balance position is a monotonic function of the force ratio, the larger the balance position it is, the larger the force ratio (n-DEP to HD drag) it has. The larger the force ratio it has, the larger the flow rate needs to be multiplied to overcome the n-DEP barrier. Therefore, even if the size measurement is not accurate, we can still predict the separation result if we increase the flow rates. However, without the size information, we can only predict the separation result on the angle coplanar electrodes but not on other structures (because for other structures the size factor is involved in a different way).

Secondly, the electro-thermal effect can be significant in high-conductivity media. The AC electro-kinetic of fluidic flow has been studied in the field for a long time [52]. Under high-conductivity media or at high voltage, the Joule heating of the electrolyte due to the large power dissipation in the liquid will locally change the conductivity and permittivity of the fluid. The resulting thermally induced conductivity gradient will result in an electro-thermal hydrodynamic flow with two circulating vortexes above the electrode directed inward or outward depending on the frequency.

Fortunately, Michael Vahey has modeled the effect at the same structure in his thesis [40]. With sufficient large particles, this effect would only affect the balance position to force ratio mapping function because of electro-thermal effect can be combined with the hydrodynamic flow to form non-uniform hydrodynamic force along the space. This effect can be characterized with standard particles. However, when the particle size is small, the DEP force acting on it would be small and not enough to keep it above the ceiling. The electro-hydrodynamic flow would bring the

particle down and not touch the ceiling. In some of my 6-μm bead experiments at high frequencies, I found that the beads had bistable behavior in the system where they had two balance positions, one on the ceiling and the other not. This occurred above ~MHz. The beads at the larger balance position look dimmer in the images likely because they are not on the focal plane. This circulating field mainly focuses on the region where the balance position is in the range of 20-30 microns.

I observed no bistable behavior in the region where beads were further away from the electrodes. However, we cannot be too far from the centroid of the electrode because if the cell is too far then the DEP force in the vertical direction would not be able to overcome the hydrodynamic lift force and the buoyant force. One way to overcome the hydrodynamic lift force is to have a higher-density media so that the particles are floating or we could invert the device (on an inverted microscope) to make gravity help us to overcome the hydrodynamic lift force. With thorough characterization of the electro-thermal effect experimentally, we should be able to experimentally obtain the balance position to n-DEP force mapping for different sizes, in different voltages, and different frequencies. Therefore, we believe that the n-DEP spring characterization can still be quantitative in the high-conductivity or high-voltage region even in the presence of electro-thermal effects.

The n-DEP spring is a simple but efficient method for single cell DEP characterization. Compared to electro-rotation and impedance spectroscopy, n-DEP spring is the force characterization that can directly link to separation without electrical model. The change of the balance position is small but quickly observed (short transient time) so we can minimize time between the measurements. If we applied a frequency sweep, we can make the cell draw a characteristic curve on the electrodes that shows its n-DEP force versus frequency. If we have a conductivity gradient, we can make the cell draw a characteristic curve on the electrodes that shows its n-DEP force versus conductivity. By playing with the frequency sequence, one can do a thorough characterization of single cell with this method. Although it cannot characterize p-DEP and crossover frequency, the n-DEP force characterization in different frequency and conductivity is sufficient for determining the n-DEP cell separation condition. The angle coplanar electrodes DEP separation is just one of the many different separation platforms. The n-DEP forces, size, shape, information measured from the n-DEP spring will significantly impact the microfluidics community by guiding the design of the intrinsic label free separation technology.

6.1.2. The automated system

Chapter 4 describes the automated system we developed that can dynamically change the frequency and the media conductivity for constructing the 2-D n-DEP force map of the cell. Changing the frequency is trivial with commercialized computerized function generator but changing the conductivity dynamically is a not an easy problem. While we choose the straight-

forward multi syringe pump approach, there are several microfluidic methods we considered but did not chose, for example, the pressure regular control or the pulse-width modulation of high conductivity liquid and low conductivity liquid. These approaches could be considered as options in the future if one wants to miniaturize the automated fluidic conductivity control.

6.1.3. Multimodal electrical and optical cytometry

The key feature of the n-DEP spring is its ability to measure the n-DEP force with images. While other electrical measurement approaches, also measure the cell properties by images, some methods are in a large range of position [9] which confine the image resolution of the single cell, not well focused [49], or static [53] so they cannot perform quantitative image analysis for a lot of cells. The n-DEP spring method combines microscopy and electrical measurement in a high-throughput way, which forms a DEP imaging cytometry for multi-model analysis of particles (**Figure 6-1**). We can study the correlation between the balance positions and size/shape/transparency/time/position (for example we have different conditions in different session of the electrodes). It would be a powerful tool to explore and discover new phenomena for DEP applications.

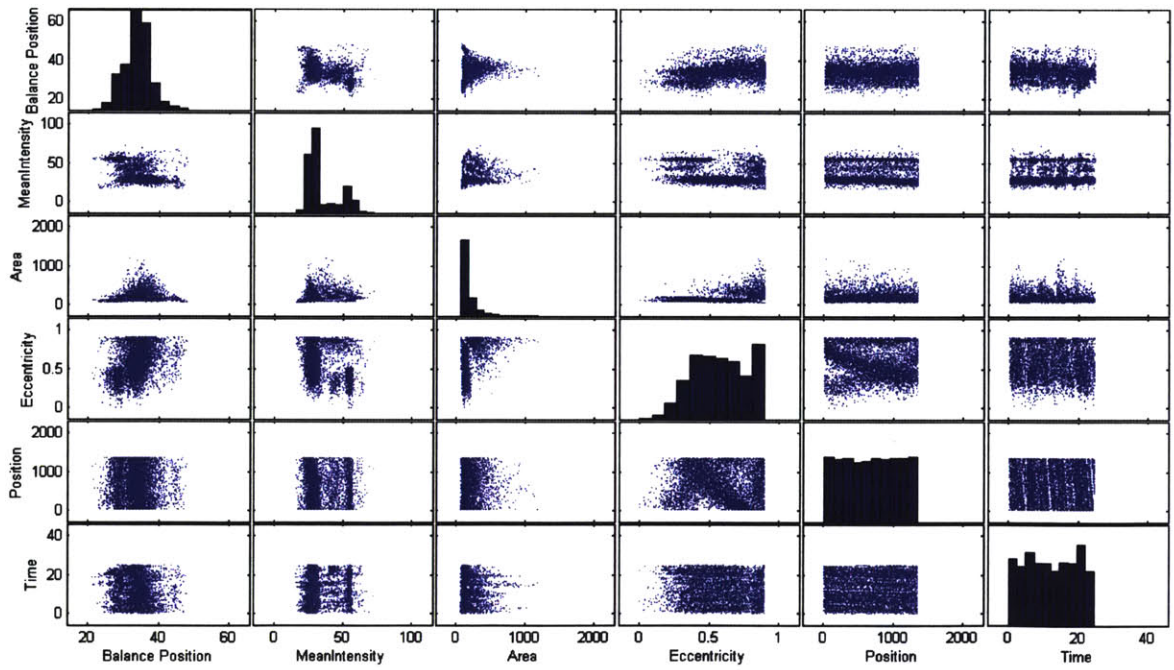

Figure 6-1 Multi-parameters scatter plots for a mixture of cells and beads. The scatter plots show how each parameter correlate with each other and how different cluster distributed. For examples, we can observe the balance position changing with time in the balance position- time plot. We can identify different cluster of cell in the area-mean intensity plot. We can exclude the data from large area or big eccentricity because they are a cluster of two or more particles.

For example, we can analyze the electrical properties of the subpopulation of complex sample without purifying them if they can be classified using optical properties. By standardizing this characterization, we can build a DEP + imaging database for many cell types. Also, we can easily study the temporal changes of the electrical properties, for example, studying electrical changes of neutrophils activation, cell apoptosis with time.

6.2. Future directions Applying frequency sequences with n-DEP spring

The n-DEP spring is a characterization method without particle tracking. However, with particle tracking, we can characterize the DEP force of a single cell by applying a frequency sequence. Thibault Honegger *et al.* has used AC electro-osmosis to focus the cell on the center of the electrodes and applied a frequency sequence to characterize DEP force on the particles [54]. However, in his method, low conductivity is required for p-DEP. With our device and method, we can focus the cells using n-DEP and form a balance position, and then apply a frequency sequence to move the cells. By analyzing the trajectory, one could characterize not only the n-DEP force but also the p-DEP force of the cells in even high conductivity media.

We have a preliminary result of the frequency sequence applied on the live and dead HL-60 cells (under 48 hours starvation) in n-DEP spring. The balance position trajectories of live and dead cells are very different because of the membrane integrity when the frequency switches between 500 kHz and 15 MHz [**Figure 6-2(a)**]. For the live cell in high conductive media (1.6 S/m), the n-DEP force is large in 500 kHz but small at 15 MHz because of the existence of the membrane. Namely, in low frequency the cell act likes an insulator because the membrane, but at 15MHz, the electrical signal bypasses the membrane capacitance and compares the effective conductivity inside the cell (high conductive media inside the cell) with the outside. Therefore, Re[CM] for a live cell is much smaller at 15 MHz than at 500 kHz and we observed the cell dancing with the frequency changes. On the other hand, for the dead HL-60 cells, the membrane has broken resulting in a ghost cell composed only of the non-conductive materials. Therefore, the dead HL-60 cells experience n-DEP in both situation. We stained the HL-60 cells with trypan blue and calculate their electrical and optical correlation. We found out that we can distinguish the live and dead cells both electrically and optically [**Figure 6-2(b)**].

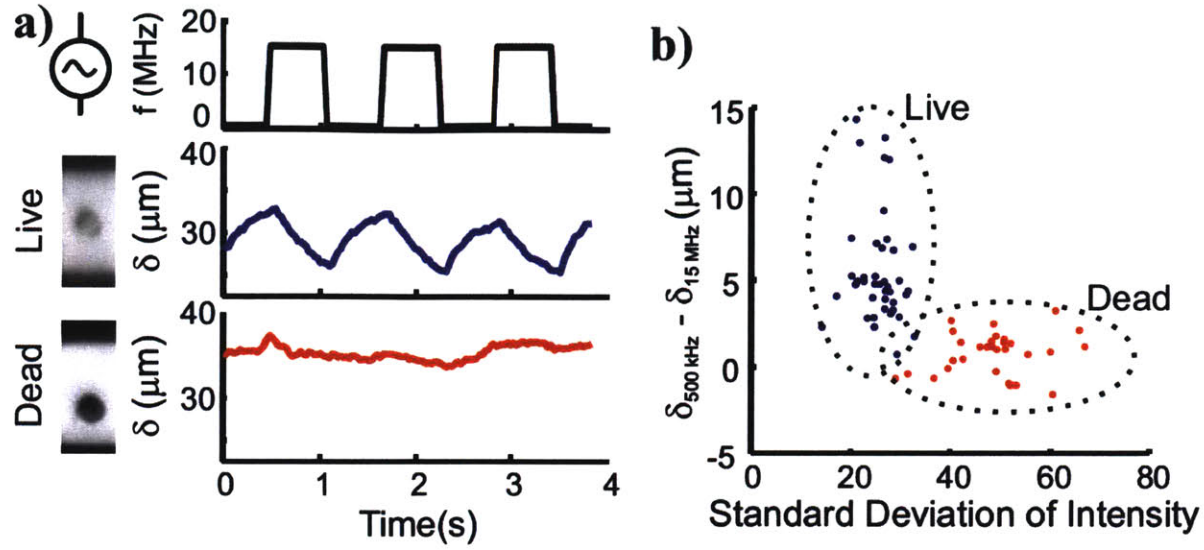

Figure 6-2 Discrimination of live and dead cells by frequency sequence. (a) Introducing a mixture of live and dead HL-60 cells and switching between low frequency (500kHz) and high frequency (15MHz) (top), some cells are observed to have varying δ (middle) while others have constant δ (bottom). **(b)** Correlating the balance position with image information (trypan blue staining of viability), we find that the cells with varying δ are live cells, whereas dead cells have constant δ.

6.2.2. Combining n-DEP spring with fluorescent imaging

If we can improve the sensitivity of our optical system, we can further developed a DEP fluorescent imaging flow cytometry. For example, before, if we want to study the electrical difference of cells between a specific type of GFP-tagged gene expression, we need to either do the DEP separation and then flow cytometry or do the FACS sorting and then the DEP characterization. The downside of doing this is the collections of the DEP separation or the FACS sorting are discretized, so the effect of the gene expression might get low-pass filtered by the discretization. With n-DEP spring with fluorescent imaging, we can obtain single cell correlation between n-DEP force and the fluorescent intensity. With our single cell correlation between n-DEP force and the fluorescent intensity (scatter plot), we can quickly find out the purity and efficiency of using the label-free DEP separation as an alternative of the FACS sorting with any threshold. This can really lead the DEP separation into the new era.

Appendix -A: Fabrication Process Flow

Starting Materials:

150-mm-diameter, 762-μm-thick Pyrex wafers (Bullen Ultrasonics, Eaton, OH)

150-mm-diameter, 650-μm-thick Silicon wafers (WaferNet, Inc., Son Jose, CA)

Step	Description	TRL Machine	Parameters
Electrode patterning, 6" Pyrex wafer			
1	Piranha clean	Acid hood	
2	Dehydration bake	HMDS oven	155°C, 3 mins, wait for air cool
3	Photoresist coat	Coater	NR-7 photoresist: - Spread 6s, 750 rpm - Spin 30s, 2500 rpm
5	Prebake	Hotplate station	155°C(plate setting), 90s, air cool to ambient
6	UV expose	EV1	20 s continuous, soft contact
7	Post-expose bake	Hotplate station	120°C(plate setting), 2 min
8	Develop, rinse and spin dry	Photo-wet bench	RD6 in a shallow beaker: - Gently agitate for 10s - Rinse with dH_2O - Use fresh RD6 with each wafer
9	Metal evaporation	E-beam	100Å Ti, 2000Å Au
10	Liftoff metal	Solvent-Au	
11	Protective resist coat	Coater	AZ 5214E, 500 rpm final speed
12	Bake	Hotplate station	120°C, 2 min
13	Dice wafer	Die saw	

Step	Description	Machine	Parameters
Microfluidic Channel Patterning, 6'' Silicon wafer			
1	Dehydration bake	Hotplate station	200°C, 30 min
2	SU-8 Spin	SU-8 spinner	SU-8 2015(20 μm thickness): Dispense~6ml SU-8 (1ml per inch diameter) Ramp to 500 rpm at 100 rpm/sec accel and hold for 5-10 seconds Ramp to 2250 rpm at 300 rpm/second and hold for total of 30 seconds
3	Prebake	Hotplate station	Slow ramp from 60°C to 95°C, hold at 95°C for 2 min; cool to ambient
4	UV expose	EV1	Flow chamber mask, 12 seconds. 30 μm separation
5	Post-expose bake	Hotplate station	Slow ramp from 60°C to 95°C, hold at 95°C for 2 min; cool to ambient
6	Develop	Solvent-Au	~ 3-5 min soak in PM Acetate 30s spin while spraying with PMA 30s spin while spraying with IPA 30s spin dry
7	Silanize wafer	EML acid hood	Put 3-4 drops of HMDS into cup in vacuum jar. Lean wafer against wall of jar, exposing both front and back Close jar, turn on vacuum for 5-10 min Turn vacuum off, let it sit ~ 30 min

Appendix -B: Determining the electrical properties of the cell from Re[CM]

In this Appendix we determine the conditions under which one can infer the electrical properties of a cell from the cross-over measurement. Note that the symbols used in this Appendix differ from those used in the main text of the thesis.

For a spherical particle with complex polarizability ε_p^* in a media with complex polarizability ε_m^*.

$$\text{CM factor} = \frac{\varepsilon_p^* - \varepsilon_m^*}{\varepsilon_p^* + 2\varepsilon_m^*}$$

At a given frequency, let

$$\varepsilon_p^* = a + bi$$

$$\varepsilon_m^* = c + di$$

where a, b, c, and d are constants, and i is $\sqrt{-1}$. Then

$$\text{CM factor} = \frac{(a-c)+(b-d)i}{(a+2c)+(b+2d)i} = \frac{[(a-c)+(b-d)i][(a+2c)-(b+2d)i]}{[(a+2c)+(b+2d)i][(a+2c)-(b+2d)i]} = \frac{[(a-c)(a+2c)+(b-d)(b+2d)]+[(b-d)(a+2c)-(a-c)(b+2d)]i}{(a+2c)^2+(b+2d)^2}$$

$$\text{Re}\{CM\} = K = \frac{(a-c)(a+2c)+(b-d)(b+2d)}{(a+2c)^2+(b+2d)^2}$$

$\Rightarrow K(a+2c)^2 + (b+2d)^2 = (a-c)(a+2c) + (b-d)(b+2d)$

$\Rightarrow K(a^2 + 4ac + 4c^2 + b^2 + 4bd + 4d^2) = a^2 + ac - 2c^2 + b^2 + bd - 2d^2$

$\Rightarrow (1-K)a^2 + (c-4cK)a + (-2c^2 - 4c^2K) + (1-K)b^2 + (d-4dK)b + (-2d^2 - 4d^2K) = 0$

The problem thus decomposes into finding a and b given c, d, and K.

If $K \neq 1$

$$a^2 + \frac{(c-4cK)}{(1-K)}a + \frac{(-2c^2-4c^2K)}{(1-K)} + b^2 + \frac{(d-4dK)}{(1-K)}b + \frac{(-2d^2-4d^2K)}{(1-K)} = 0$$

and therefore

$$\left[a^2 + \frac{(c-4cK)}{2(1-K)}\right]^2 + \left[b^2 + \frac{(d-4dK)}{2(1-K)}\right]^2 = \frac{(2c^2+4c^2K)}{(1-K)} + \frac{(2d^2+4d^2K)}{(1-K)} + \left[\frac{(c-4cK)}{2(1-K)}\right]^2 + \left[\frac{(d-4dK)}{2(1-K)}\right]^2$$

This is actually the equation for a circle in the a-b plane!

The circle has radius R and center as the following.

$$R = \sqrt{\frac{(2c^2+4c^2K)}{(1-K)} + \frac{(2d^2+4d^2K)}{(1-K)} + \left[\frac{(c-4cK)}{2(1-K)}\right]^2 + \left[\frac{(d-4dK)}{2(1-K)}\right]^2}$$

Center $\left(-\frac{(c-4cK)}{2(1-K)}, -\frac{(d-4dK)}{2(1-K)}\right)$

If we measure two Ks in this frequency by changing the media conductivity (d will also change), we will get a pair of circles and solve for their intersection. If we measure more, they will all intersect at the same points. Therefore, we can get an unique solution of a and b at this frequency (one of the two intersections might be unreasonable because a<0 or b<0). If we measure at many different frequencies, we will get $a(\omega)$, $b(\omega)$ and finally, $\varepsilon_p^*(\omega)$. Eventually, we can determine the electrical model by fitting ε_p^*. This curve can be easy or hard to fit because in nature the electrical property of cell is very complicated given so many irregular organelles, each with different complicated polarizabilities. This complex ε_p^* may not be explained by any current models. If we can measure this curve accurately by tuning c or d, we might be able to find out further more interesting electrical models for cell.

Let's go back to the IDP measurement. If we can only have one measurement, which is the IDP where K=0. The solution set of a and b are on the circle with

$$R = \sqrt{\frac{(2c^2+4c^20)}{(1-0)} + \frac{(2d^2+4d^20)}{(1-0)} + \left[\frac{(c-4c0)}{2(1-0)}\right]^2 + \left[\frac{(d-4d0)}{2(1-0)}\right]^2} = \frac{3}{2}\sqrt{c^2+d^2}$$

Center : $\left(-\frac{c}{2}, -\frac{d}{2}\right)$

As we can see, this circle will pass through a=c, b=d, which is expected when the media and particle have the same electrical properties. Nevertheless, the solution of a and b could be any other point on this circle as well, so it is impossible to get a and b without additional assumptions. However, if we assume with some simple electrical models of the cells, we can still find the parameters of this model. But here we cannot uniquely determine anything by the measurement if the electrical model is incorrect, which one cannot be sure of. We can mathematically find an answer of the electrical model of two parameters by two measurements. However, when we make the third measurement, we might find out it does not fit the model and cannot find a solution common solution. Therefore, we need to adjust this model into three or more parameters in order to fit the measurement we have.

For example

$$\varepsilon_p^* = a + bi = Re\{\varepsilon_p^*(\omega)\} + Imag\{\varepsilon_p^*(\omega)\}i$$

$$\varepsilon_m^* = c + di = Re\{\varepsilon_m^*(\omega)\} + Imag\{\varepsilon_m^*(\omega)\}i$$

Normally, we assume the media act as a lossy dielectric material, so we can assume the following.

$$\varepsilon_m^* = c + di = \varepsilon_m - (\frac{\sigma_m}{\omega})i$$

If we assume the same thing to the particle,

$$\varepsilon_p^* = a + bi = \varepsilon_p - (\frac{\sigma_p}{\omega})i$$

In this model,

$$a = \varepsilon_p$$

$$b = -(\frac{\sigma_p}{\omega})$$

$$c = \varepsilon_m$$

$$d = -(\frac{\sigma_m}{\omega})$$

By substituting a, b, c, d from

$$\left[a^2 + \frac{(c-4cK)}{2(1-K)}\right]^2 + \left[b^2 + \frac{(d-4dK)}{2(1-K)}\right]^2 = \frac{(2c^2+4c^2K)}{(1-K)} + \frac{(2d^2+4d^2K)}{(1-K)} + \left[\frac{(c-4cK)}{2(1-K)}\right]^2 + \left[\frac{(d-4dK)}{2(1-K)}\right]^2$$

We have

$$\left[\varepsilon_p{}^2 + \frac{(\varepsilon_m-4\varepsilon_mK)}{2(1-K)}\right]^2 + \left[\left(\frac{\sigma_p}{\omega}\right)^2 + \frac{\left(4(\frac{\sigma_m}{\omega})K-(\frac{\sigma_m}{\omega})\right)}{2(1-K)}\right]^2 = \frac{(2\varepsilon_m{}^2+4\varepsilon_m{}^2K)}{(1-K)} + \frac{\left(2(\frac{\sigma_m}{\omega})^2+4(\frac{\sigma_m}{\omega})^2K\right)}{(1-K)} +$$

$$\left[\frac{(\varepsilon_m-4\varepsilon_mK)}{2(1-K)}\right]^2 + \left[\frac{\left((\frac{\sigma_m}{\omega})-4(\frac{\sigma_m}{\omega})K\right)}{2(1-K)}\right]^2$$

By having two measurements at two different frequencies ω_1 and ω_2, we might or might not find $\sigma_{m,1}$and $\sigma_{m,2}$ such that $K(\omega_1, \sigma_{m,1})$ and $K(\omega_2, \sigma_{m,2})$ equal to zeros.

So we are solving for the intersections of two ellipsoids with the same eccentricity but different center and different major and minor axes in the $\varepsilon_p - \sigma_p$ plane.

By doing so, we could potentially find the ε_p and σ_p (there might be no IDP in any σ_m for a specific frequency as well) by two measurements of IDP in two different frequencies. If we have more complicated models with more parameters, we need more measurement to fit.

In conclusion, if we can measure two Ks at a given frequency, we can mathematically determine the $\varepsilon_p^*(\omega)$. We cannot determine $\varepsilon_p^*(\omega)$ by only the IDP (K=0) measurement. With additional electrical models, we can potentially determine n parameters for a specific model by n measurements.

References

[1] D. R. Gossett et al., "Label-free cell separation and sorting in microfluidic systems.," *Analytical and bioanalytical chemistry*, vol. 397, no. 8, pp. 3249-67, Aug. 2010.

[2] S. Zheng et al., "Membrane microfilter device for selective capture, electrolysis and genomic analysis of human circulating tumor cells.," *Journal of chromatography. A*, vol. 1162, no. 2, pp. 154-61, Aug. 2007.

[3] M. Yamada et al., "Microfluidic devices for size-dependent separation of liver cells.," *Biomedical microdevices*, vol. 9, no. 5, pp. 637-45, Oct. 2007.

[4] S. Choi, S. Song, C. Choi, and J.-K. Park, "Microfluidic self-sorting of mammalian cells to achieve cell cycle synchrony by hydrophoresis.," *Analytical chemistry*, vol. 81, no. 5, pp. 1964-8, Mar. 2009.

[5] D. Di Carlo, J. F. Edd, D. Irimia, R. G. Tompkins, and M. Toner, "Equilibrium separation and filtration of particles using differential inertial focusing.," *Analytical chemistry*, vol. 80, no. 6, pp. 2204-11, Mar. 2008.

[6] D. Huh et al., "Gravity-driven microfluidic particle sorting device with hydrodynamic separation amplification.," *Analytical chemistry*, vol. 79, no. 4, pp. 1369-76, Feb. 2007.

[7] R. Huang et al., "A microfluidics approach for the isolation of nucleated red blood cells (NRBCs) from the peripheral blood of pregnant women.," *Prenatal diagnosis*, vol. 28, no. 10, pp. 892-9, Oct. 2008.

[8] A. Lenshof et al., "Acoustic whole blood plasmapheresis chip for prostate specific antigen microarray diagnostics.," *Analytical chemistry*, vol. 81, no. 15, pp. 6030-7, Aug. 2009.

[9] M. D. Vahey and J. Voldman, "An equilibrium method for continuous-flow cell sorting using dielectrophoresis.," *Analytical chemistry*, vol. 80, no. 9, pp. 3135-43, May 2008.

[10] R. Pethig, "Review Article — Dielectrophoresis : Status of the theory , technology , and applications," *Nano*, pp. 1-35, 2010.

[11] J. Yang, Y. Huang, X. B. Wang, F. F. Becker, and P. R. Gascoyne, "Differential analysis of human leukocytes by dielectrophoretic field-flow-fractionation.," *Biophysical journal*, vol. 78, no. 5, pp. 2680-9, May 2000.

[12] G. H. Markx, M. S. Talary, and R. Pethig, "Separation of viable and non-viable yeast using dielectrophoresis.," *Journal of biotechnology*, vol. 32, no. 1, pp. 29-37, Jan. 1994.

[13] K. F. Hoettges, Y. Hübner, L. M. Broche, S. L. Ogin, G. E. N. Kass, and M. P. Hughes, "Dielectrophoresis-activated multiwell plate for label-free high-throughput drug assessment.," *Analytical chemistry*, vol. 80, no. 6, pp. 2063-8, Mar. 2008.

[14] M. Stephens, M. S. Talary, R. Pethig, A. K. Burnett, and K. I. Mills, "The dielectrophoresis enrichment of CD34+ cells from peripheral blood stem cell harvests.," *Bone marrow transplantation*, vol. 18, no. 4, pp. 777-82, Oct. 1996.

[15] P. R. C. Gascoyne, X.-B. Wang, Y. Huang, and F. F. Becker, "Dielectrophoretic Separation of Cancer Cells from Blood.," *IEEE transactions on industry applications*, vol. 33, no. 3, pp. 670-678, Jan. 1997.

[16] P. Gascoyne, C. Mahidol, M. Ruchirawat, J. Satayavivad, P. Watcharasit, and F. F. Becker, "Microsample preparation by dielectrophoresis: isolation of malaria.," *Lab on a chip*, vol. 2, no. 2, pp. 70-5, May 2002.

[17] L. A. Flanagan et al., "Unique dielectric properties distinguish stem cells and their differentiated progeny.," *Stem cells (Dayton, Ohio)*, vol. 26, no. 3, pp. 656-65, Mar. 2008.

[18] Z. R. Gagnon, "Cellular dielectrophoresis: applications to the characterization, manipulation, separation and patterning of cells.," *Electrophoresis*, vol. 32, no. 18, pp. 2466-87, Sep. 2011.

[19] T. Schnelle, T. Mu, G. Gradl, S. G. Shirley, and G. Fuhr, "Paired microelectrode system : dielectrophoretic particle sorting and force calibration," *Journal of Electrostatics*, vol. 47, pp. 121-132, 1999.

[20] T. Honegger, K. Berton, E. Picard, and D. Peyrade, "Determination of Clausius–Mossotti factors and surface capacitances for colloidal particles," *Applied Physics Letters*, vol. 98, no. 18, p. 181906, 2011.

[21] H. A. Pohl and R. Pethig, "Dielectric measurements using non-uniform electric field (dielectrophoretic) effects," *Journal of Physics E: Scientific Instruments*, vol. 10, no. 2, pp. 190-193, Feb. 1977.

[22] H. Imasato and T. Yamakawa, "A milestone toward clinical laboratory automation - measurement of dielectrophoretic force of femto-Newtons (10−15 Newtons) -."

[23] G. Fuhr, T. Schnelle, T. Müller, H. Hitzler, S. Monajembashi, and K.-O. Greulich, "Force measurements of optical tweezers in electro-optical cages," *Applied Physics A: Materials Science & Processing*, vol. 67, no. 4, pp. 385-390, Oct. 1998.

[24] M.-T. Wei, J. Junio, and H. D. Ou-Yang, "Direct measurements of the frequency-dependent dielectrophoresis force.," *Biomicrofluidics*, vol. 3, no. 1, p. 12003, Jan. 2009.

[25] L. M. Broche, K. F. Hoettges, S. L. Ogin, G. E. N. Kass, and M. P. Hughes, "Rapid, automated measurement of dielectrophoretic forces using DEP-activated microwells.," *Electrophoresis*, Jul. 2011.

[26] B. G. Hawkins, C. Huang, S. Arasanipalai, and B. J. Kirby, "Automated dielectrophoretic characterization of Mycobacterium smegmatis.," *Analytical chemistry*, vol. 83, no. 9, pp. 3507-15, May 2011.

[27] R. Hölzel, "Electrorotation of single yeast cells at frequencies between 100 Hz and 1.6 GHz.," *Biophysical journal*, vol. 73, no. 2, pp. 1103-9, Aug. 1997.

[28] H. Morgan, T. Sun, D. Holmes, S. Gawad, and N. G. Green, "Single cell dielectric spectroscopy," *Journal of Physics D: Applied Physics*, vol. 40, no. 1, pp. 61-70, Jan. 2007.

[29] F. Holzner, B. Hagmeyer, H. Schutte, M. Kubon, B. Angres, and M. Stelzle, "Numerical modelling and measurement of cell trajectories in 3-D under the influence of dielectrophoretic and hydrodynamic forces," *ELECTROPHORESIS*, vol. 32, no. 17, pp. 2366-2376, 2011.

[30] A. Irimajiri, T. Hanai, and A. Inouye, "A dielectric theory of 'multi-stratified shell' model with its application to a lymphoma cell," *Journal of Theoretical Biology*, vol. 78, no. 2, pp. 251-269, May 1979.

[31] T. B. Jones, "Electromechanics of particles," *Cambridge: Cambridge University Press*, 1995.

[32] K. Asami, Y. Takahashi, and S. Takashima, "Dielectric properties of mouse lymphocytes and erythrocytes.," *Biochimica et biophysica acta*, vol. 1010, no. 1, pp. 49-55, Jan. 1989.

[33] R. Höber, "Eine Methode, die elektrische Leitfähigkeit im Innern von Zellen zu messen," *Pflüger's Archiv für die Gesammte Physiologie des Menschen und der Tiere*, vol. 133, no. 4–6, pp. 237-253, Jul. 1910.

[34] K. Asami, "Characterization of heterogeneous systems by dielectric spectroscopy," *Progress in Polymer Science*, vol. 27, no. 8, pp. 1617-1659, Oct. 2002.

[35] J. Yang, Y. Huang, X. Wang, X. B. Wang, F. F. Becker, and P. R. Gascoyne, "Dielectric properties of human leukocyte subpopulations determined by electrorotation as a cell separation criterion.," *Biophysical journal*, vol. 76, no. 6, pp. 3307-14, Jun. 1999.

[36] D. Holmes et al., "Leukocyte analysis and differentiation using high speed microfluidic single cell impedance cytometry.," *Lab on a chip*, vol. 9, no. 20, pp. 2881-9, Oct. 2009.

[37] T. Sun, N. G. Green, S. Gawad, and H. Morgan, "Analytical electric field and sensitivity analysis for two microfluidic impedance cytometer designs.," *IET nanobiotechnology / IET*, vol. 1, no. 5, pp. 69-79, Oct. 2007.

[38] N. Demierre, T. Braschler, P. Linderholm, U. Seger, H. van Lintel, and P. Renaud, "Characterization and optimization of liquid electrodes for lateral dielectrophoresis.," *Lab on a chip*, vol. 7, no. 3, pp. 355-65, Mar. 2007.

[39] Y. Huang, X. B. Wang, F. F. Becker, and P. R. Gascoyne, "Introducing dielectrophoresis as a new force field for field-flow fractionation.," *Biophysical journal*, vol. 73, no. 2, pp. 1118-29, Aug. 1997.

[40] M. D. Vahey, "A Microfluidic Platform for the Genome-Wide Analysis of Electrical Phenotype : Physical Theories and Biological Applications," *Electrical Engineering*, 2010.

[41] D. Irimia, S.-Y. Liu, W. G. Tharp, A. Samadani, M. Toner, and M. C. Poznansky, "Microfluidic system for measuring neutrophil migratory responses to fast switches of chemical gradients.," *Lab on a chip*, vol. 6, no. 2, pp. 191-8, Mar. 2006.

[42] F. Lin, W. Saadi, S. W. Rhee, S.-J. Wang, S. Mittal, and N. L. Jeon, "Generation of dynamic temporal and spatial concentration gradients using microfluidic devices.," *Lab on a chip*, vol. 4, no. 3, pp. 164-7, Jul. 2004.

[43] Y. Liu, J. Sai, A. Richmond, and J. P. Wikswo, "Microfluidic switching system for analyzing chemotaxis responses of wortmannin-inhibited HL-60 cells.," *Biomedical microdevices*, vol. 10, no. 4, pp. 499-507, Aug. 2008.

[44] O. N, "A Threshold Selectrion Method from Gray-Level Histograms," *IEEE Transactions on Systems Man And Cybernetics*, vol. 9, no. 1, pp. 62-66, 1979.

[45] W. M. Arnold, H. P. Schwan, and U. Zimmermann, "Surface conductance and other properties of latex particles measured by electrorotation," *The Journal of Physical Chemistry*, vol. 91, no. 19, pp. 5093-5098, Sep. 1987.

[46] X.-F. Zhou, G. H. Markx, R. Pethig, and I. M. Eastwood, "Differentiation of viable and non-viable bacterial biofilms using electrorotation," *Biochimica et Biophysica Acta (BBA) - General Subjects*, vol. 1245, no. 1, pp. 85-93, Aug. 1995.

[47] H. P. Schwan, "Linear and nonlinear electrode polarization and biological materials," *Annals of Biomedical Engineering*, vol. 20, no. 3, pp. 269-288, May 1992.

[48] F. F. Beckert, X.-b Wangt, Y. Huangt, R. Pethigt, and J. Vykoukalt, "The removal of human leukaemia cells from blood using interdigitated microelectrodes," *Blood Cells*, vol. 2659, 1994.

[49] F. Gielen, A. J. Demello, and J. B. Edel, "Dielectric Cell Response in Highly Conductive Buffers.," *Analytical chemistry*, vol. 84, no. 4, pp. 1849-1853, Jan. 2012.

[50] J. Cohen, "The immunopathogenesis of sepsis.," *Nature*, vol. 420, no. 6917, pp. 885-91, 2002.

[51] M. D. Vahey, "A Novel Method for the Continuous Separation of Microorganisms based on Electrical Properties by," *Electrical Engineering*, pp. 1-103, 2006.

[52] J. Oh, R. Hart, J. Capurro, and H. M. Noh, "Comprehensive analysis of particle motion under non-uniform AC electric fields in a microchannel.," *Lab on a chip*, vol. 9, no. 1, pp. 62-78, Jan. 2009.

[53] W. M. Arnold and U. Zimmermann, "Electro-rotation: development of a technique for dielectric measurements on individual cells and particles," *Journal of Electrostatics*, vol. 21, no. 2–3, pp. 151-191, Sep. 1988.

[54] T. Honegger, K. Berton, E. Picard, and D. Peyrade, "Determination of Clausius–Mossotti factors and surface capacitances for colloidal particles," *Applied Physics Letters*, vol. 98, no. 18, p. 181906, May 2011.

[55] I. Ermolina, Y. Polevaya, Y. Feldman, B.-Z. Ginzburg, and M. Schlesinger, "Study of normal and malignant white blood cells by time domain dielectric spectroscopy," *IEEE Transactions on Dielectrics and Electrical Insulation*, vol. 8, no. 2, pp. 253-261, Apr. 2001.